Contents

List of Figures

To whom I love the most

Acknowledgments

I would like to express my special appreciation and thanks to my supervisor Professor André Zaccarin. You have been a tremendous mentor for me. I appreciated your encouragement, guidance, and support. I feel honored to have been given the opportunity to contribute to research under your supervision.

My appreciation also goes to my co-supervisor Raphaël Desbiens. Your advice on both research as well as on my career have been priceless. You directed my thesis to the industry domain which helped me to link research to industry. I also thank you for all what you did to help me settle with my family in Quebec city.

I would like to thank Prof. Drissen and the Groupe de recherche en astrophysique, who gave us access to their instrument to complete this work. Thanks for the training and support to use the instrument and your data.

Also, I would like to pay my humble respects to my family, especially my parents: My mother (God bless her), who did not have the chance to see me in this day, my father who waited a long time for this day. Your prayer for me was what sustained me thus far.

A special thanks to my beloved wife Amira. Words can not express how grateful I am to all your sacrifice and support for me since our mariage. You give me love, guidance, self confidence as well as sharing ideas in the research with me. I will never forget that you were always my support in the moments when there was no one to answer my queries.

Chapter 1

Introduction

This thesis presents a research project that was realized at the Laboratoire de Vision et systèmes Numériques (LVSN) at l'Université Laval. The subject of this work was initially defined in a research collaboration between Prof. Zaccarin and ABB lnc. It was partly funded by the Natural Sciences and Engineering Research Council of Canada and ABB Inc. Most of the experimental work was made possible by the collaboration of Prof Drissen, from the Groupe de recherche en astrophysique, who gave us access to SpIOMM, an imaging Fourier transform spectrometer.

1.1 Applications of Imaging Fourier Transform Spectrometers

Imaging Fourier Transform Spectrometers (IFTS) are important systems for remote sensing imaging applications because of their ability to provide, simultaneously, both high spatial and spectral resolution images of a scene. The spectral data obtained from a high resolution imaging FTS is often classified as "hyper spectral".

The idea of IFTS was first proposed in 1972 [37]. However, it is only in the 1990s that we had the first IFTS that produced valuable scientific results [32]. Nowadays, IFTS has proved its competency in many applications because of its ability to provide rapid and non-destructive analysis both spectrally and spatially.

In the field of biomedical imaging and sensing, microspectroscopy is used for cancer pathology and tumor diagnosis to obtain more information about the composition of the tumor tissue [4, 5, 7, 45]. In environmental domain, IFTS are used for remote detection of gases and liquids, hazardous vapors, and monitoring of the ozone layer [51, 17, 20]. They are also used by the military for remote detection of camouflaged vehicles, analysis of aircrafts exhaust, and standoff chemical detection [1, 43, 40]. IFTS are also particularly suited for applications in astronomy because of their high sensitivity to light. They are used, among others, for studying the statistics and physics of galaxy and the early stages of star formation [42, 48, 33].

1.2 Motivations

An IFTS produces a data cube where the x and y axis are the spatial coordinates of the scene, and the interferogram samples are found along the z axis. The IFTS captures one interferogram for each of its sensor elements (pixels). The Fourier transform of each interferogram generates an estimate of the radiometric spectrum, within the sensor band, radiated by the scene element imaged by that pixel. For maximum spectral accuracy and resolution, each interferogram sample must come from the same location in the scene. This means that the scene being imaged must be stationary for the duration of the scan, which may last from less than a second to many hours depending on the application. This condition is hard to achieve in many cases due to the relative motion between the instrument and the scene, or simply because of the nature of the scene being imaged. This relative motion or motion in the scene will, at best, reduce the spectral resolution of the data, and at worst make the data unusable.

When there is relative motion between the scene and the instrument, or within the scene, we need to build an interferogram for each scene element from the interferogram samples of the data cube. So, if the instrument underwent a motion in a certain direction and we knew the parameters of that motion, we would only need to shift the image planes in the direction opposite to that motion. In space-borne and airborne FTS imagers, motion compensation is done using opto-mechanical means to keep the sensor pointing on the same ground area for the duration of the scan. We propose instead to perform motion compensation a posteriori, using the data information. This is simpler as it requires no hardware and can be used to compensate for non-predictable motion where pointing mechanisms do not work.

Motion compensation in the image plane of the interferograms is conceptually interesting but not as straightforward as it may sound. Most motion compensation techniques, like the one developed for video compression, assumes that the signals they want to align have constant intensity. An interferogram signal is a modulated signal and is not constant. Interferogram samples, besides being measurements of a specific scene element, have properties that directly tie them to a pixel on the sensor from which they were acquired. First, the sampling interval of the interferogram is typically not uniform throughout the sensor. Second, the calibration parameters are also not uniform throughout the sensor (calibration is needed to convert a sensor reading from a relative to an absolute scale). Registration of the image planes of a data cube acquired by an IFTS needs to take into account these two properties in order to generate interferograms from which electromagnetic spectral information can be extracted accurately and with high resolution.

1.3 Objectives and Major Contributions

Our objective is to develop algorithms to process data acquired by an IFTS (without opto-mechanical pointing mechanisms) when there is a relative motion between the scene and the

instrument or within the scene, in order to reduce the impact of this motion on the spectral accuracy and resolution of the acquired data.

We can summarize the contributions in this thesis as :

- Development of suitable motion estimation algorithms to align the frames of a data cube acquired by an IFTS when there is relative motion between the scene and the instrument or within the scene. With these algorithms, we generate data cubes where each interferogram has only samples coming from the same scene location.

- Development of an algorithm that takes into account the spatially varying sampling interval of an instrument and resamples the interferograms after motion compensation so that each interferogram is sampled uniformly.

- Development of an algorithm to calibrate the data cube acquired by an IFTS while preserving the information required for motion compensation of that data.

1.4 Thesis Organization

Chapter 1 summarizes the motivation, the objectives and the main contributions of this research. Chapter 2 presents an overview of FTS and IFTS including the background information that will be used later in the thesis. The simulated and experimentally acquired data cubes that are used for this research are described in Chapter 2.

A description of the problem coming with data cubes acquired from a moving IFTS is given in Chapter 3. We survey different image registration techniques appropriate for our problem and describe the algorithms we have developed for registering the frames of the data cubes. Results obtained with these algorithms on simulated and experimental data are given.

In Chapter 4, we present the concept of off-axis distortion, and its spatial dependance (which is the result of the spatially varying sampling interval of an IFTS), and we propose an algorithm that takes into account and corrects the mixed off-axis distortion of a motion compensated interferogram. Results obtained on simulated and experimental data are given.

In Chapter 5, we discuss the impact of calibration on our algorithms. We discuss the difference between calibrating a data cube acquired from a fixed IFTS and the challenge of calibrating data cube acquired from a moving IFTS. We present an algorithm for calibrating a data cube acquired with a moving IFTS and give results on simulated and experimental data. Motion compensation, mixed off-axis distortion and calibration are integrated and used to process data cubes.

We conclude this thesis in Chapter 6 and we suggest directions for future research.

Chapter 2

Imaging Fourier Transform Spectrometer and Data Cube Acquisition

This chapter presents a general review of the basics of FTS and IFTS instruments. The review is not exhaustive but concentrates on the needed information that is most relevant to our project. In the second part of the chapter, we describe the IFTS data cubes both simulated and experimentally used in this thesis. The simulated data is generated from a simulator designed for the purpose of this research. The experimental data was acquired from an IFTS prototype at ABB Bomem and an IFTS for astronomy.

2.1 Fourier Transform Spectrometer

A Fourier Transform Spectrometer (FTS) captures the electromagnetic spectrum of a source by measuring the temporal coherence of a radiative source. A beam of light is split into two beams and reflected off two mirrors. At least one of the mirrors is moving to change the optical path difference between the two beams. The reflected beams are then brought together and the amplitude of the interference pattern is measured. An interferogram is measured by sampling the interference pattern for different optical path differences. The Fourier Transform of this interferogram returns the spectrum of the input source. Figure 2.1 shows a Michelson interferometer that is considered as the heart of the FTS. Given a monochromatic source $A(\sigma_0)$, where σ_0 is the wave-number (reciprocal of wavelength), the intensity of the interferogram, as a function of the optical path difference (OPD) x between the two beams, is given by

$$I_t(x) = 2A(\sigma_0)[1 + cos(2\pi\sigma_0 x)] \tag{2.1}$$

where $I_t(x)$ is the intensity at a given OPD x.

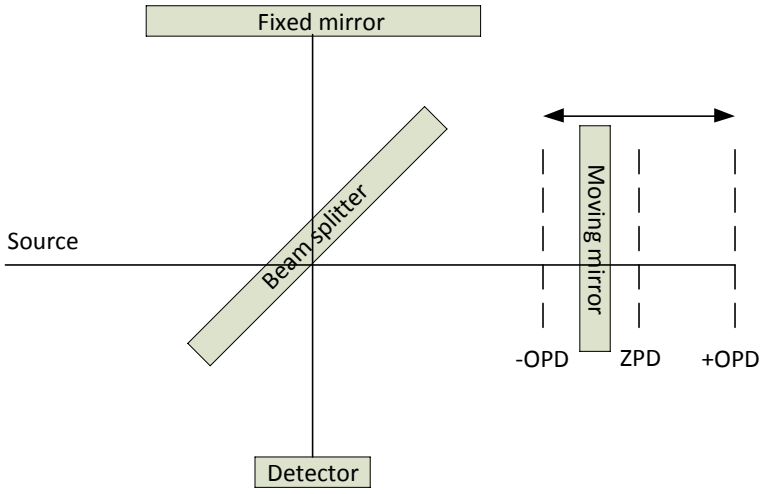

Figure 2.1: FTS.

The zero path difference (ZPD) is the location where the optical path difference is zero, and is the point where the interferogram is maximum. This occurs when both mirrors are equally apart from the beam splitter. At this point the size of the interference pattern is infinite, and the central fringe occupies the entire image plane.

2.1.1 From Monochromatic to Polychromatic

When the source contains more than one frequency, the detector detects a superposition of such cosines. The monochromatic light $A(\sigma_0)$ will be replaced by a polychromatic light, which has a spectrum of $B(\sigma)$. The equation can be expressed as

$$I_t(x) = 2\int_0^\infty B(\sigma)[1 + cos(2\pi\sigma x)]d\sigma \tag{2.2}$$

that in turn can be arranged to

$$\begin{aligned} I_t(x) &= 2\int_0^\infty B(\sigma)d\sigma + 2\int_0^\infty B(\sigma)cos(2\pi\sigma x)d\sigma \\ &= I(0) + I(x) \end{aligned} \tag{2.3}$$

where $I(0)$ is a constant value and $I(x)$ is the part of the interferogram, which after a Fourier transform, gives the spectrum.

The interferogram and its spectrum are related by a cosine transform, which is suitable for an ideal interferogram that is symmetric about the ZPD. Hence we have the following transform

pair

$$\begin{aligned} I(x) &= \int_{-\infty}^{\infty} B(\sigma) e^{j2\pi\sigma x}\, \mathrm{d}\sigma \\ &= F^{-1}\{B(\sigma)\} \\ B(\sigma) &= \int_{-\infty}^{\infty} I(x) e^{-j2\pi\sigma x}\, \mathrm{d}x \\ &= F\{I(x)\} \\ I(x) &\iff B(\sigma) \end{aligned} \tag{2.4}$$

where, $F^{-}1\{\}$ is the inverse Fourier transform operator and $F\{\}$ is the Fourier transform operator, and the $\iff$ is the Fourier transform conversion [24].

2.1.2 Spectral Resolution

Spectral resolution describes the ability of a sensor to define fine wave-number intervals. The output spectrum is characterized by the maximum wave-number that depends on the sampling rate of the interferogram, and its resolution that depends on the length of the OPD. To have a high resolution spectrum, the OPD must be extended to high values. For a given maximum OPD, the unapodised spectral resolution is given by

$$\delta\sigma = \frac{1}{2 \times OPD_{max}}. \tag{2.5}$$

Having an OPD extending to infinity results in a spectrum with an infinite resolution. This is obviously impossible to obtain because the moving mirror can only travel a finite distance. The interferogram is truncated as the mirror reaches the minimum or the maximum OPD. Truncating the interferogram is equivalent to multiplying the infinite length interferogram with a boxcar function.

Instrument Line Shape Function

The truncated interferogram can be written as

$$I_L(x) = \Pi_{2L}(x) I(x) \tag{2.6}$$

where, $I(x)$ is interferogram before truncation, Π_{2L} is the boxcar function that equals one when $|x| \leq L$ and zero otherwise, L is the OPD path length, and finally I_L is the interferogram after truncation.

Taking the Fourier transform of the previous equation gives

$$A_L(\sigma) = W_L(\sigma) * A(\sigma) \tag{2.7}$$

where $W_L(\sigma) = 2Lsinc(2\pi\sigma L)$ and is the transform of the boxcar function, and $*$ is the convolution operator. Convolution of the the spectrum $A(\sigma)$ with $W_L(\sigma)$ lowers the resolution of the output spectrum $A_L(\sigma)$ [24].

To show the relation between the OPD, ILS and the spectral resolution, we simulated two spectra for CO_2. We changed the length of the OPD in two similar scans. The first spectrum has a relatively short OPD (1000 samples) with a spectral resolution of 4 cm^{-1}, while the second spectrum has an OPD four times longer (4000 samples) to give a spectral resolution of 1 cm^{-1}. The sensor operating band is between 500 cm^{-1} to 2000 cm^{-1}, with a sampling rate twice the highest wave number. Figure 2.2 shows the effect of changing the length of OPD on the spectral resolution. We can clearly see that the spectrum obtained with the

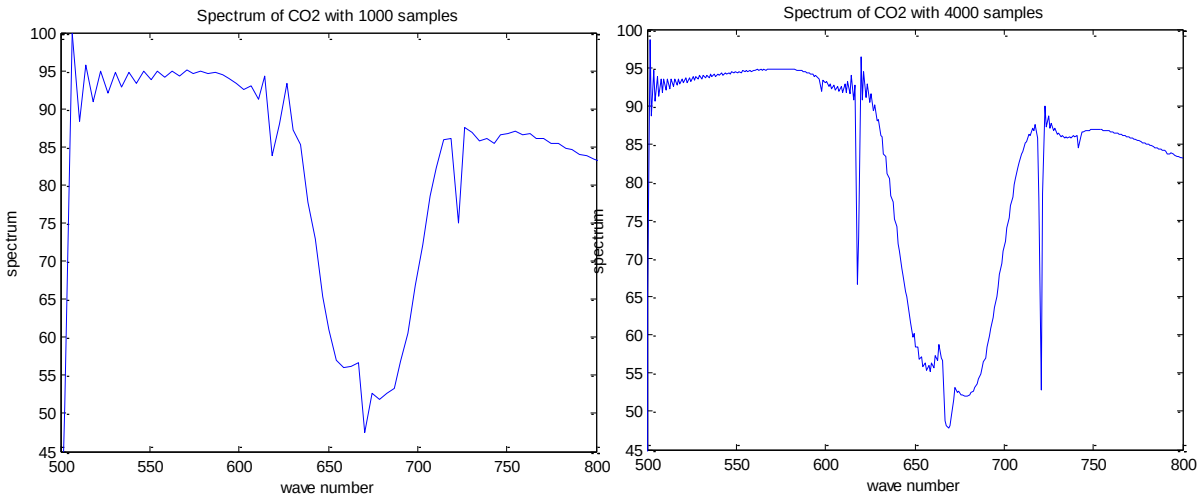

Figure 2.2: Effect of OPD length on spectral resolution.

interferogram with the longer OPD has a higher resolution than the spectrum generated with the interferogram with shorter OPD. We use this relation to setup the resolution of the simulated output data cubes used in the thesis.

2.1.3 Off-axis Effect

Real light sources are never just points, but they are extended sources with finite sizes. So, when light rays enter the interferometer, they make different angles with respect to the optical axis. An off-axis light ray is modulated at a lower frequency than a light ray on the optical axis when we move the mirror of the interferometer. This implies that the interferogram scale is compressed for pixels that are off-axis (i.e., the interferograms are not sampled at the same interval as a function of the location of the pixels on the sensor). This is the off-axis effect.

The scale compression is a function of the angle between the off-axis and on-axis pixel. We use the small angle approximation to calculate the off-axis effect for the simulated data in the thesis. We use $cos(\theta) \approx (1 - \frac{\theta^2}{2})$, where θ is the angle between the incoming ray and the optical axis, and $cos(\theta)$ is the off-axis effect. Assume that the radius of the circle for a circular

radiation source is r, and its focal length is f, then $r \approx f\theta$,and $cos(\theta) \approx (1 - \frac{r^2}{2f^2})$. According to the equation of the interferogram, the intensity at a point source not on the optical axis will be

$$I(x) = 2\int_0^\infty A(\sigma)cos(2\pi\sigma x cos(\theta))d\sigma \tag{2.8}$$

This intensity will be modified for a circular source and will depend on the off-axis angle as follows

$$I(x) = 2\int_0^{2\pi}\int_0^{\theta_{max}}\int_0^\infty A(\sigma)cos(2\pi\sigma x cos(\theta))d\sigma sin\theta d\theta d\phi \tag{2.9}$$

The off-axis effect causes the interferograms to be sampled at slightly shorter OPD, therefore, affecting the interferogram in the space domain as well as affecting the spectrum in the spectral domain. The spectra appear to be expanded to slightly lower wave numbers, causing them to have different spectral sampling intervals. At the centre pixel the off-axis has a small impact, whereas the greatest effect is experienced by the corner pixel elements. We define σ_0 as the wave-number of the central pixel with the minimum off-axis effect, and σ is the wave-number for any other pixel. They are related by the cosine of the off-axis angle θ as $\frac{\sigma}{\sigma_0} = cos(\theta)$. Figure 2.3a shows the off-axis angle. Figure 2.3b shows the spectrum of a monochromatic

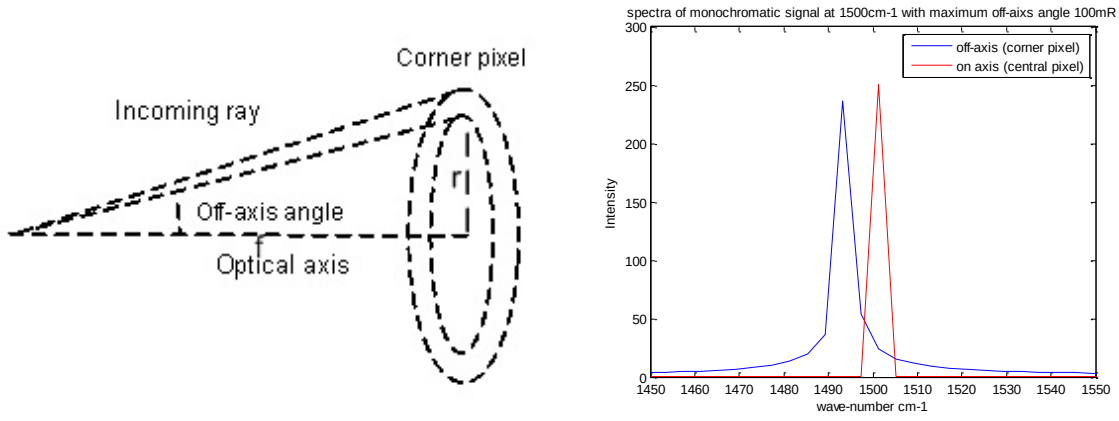

(a) Off-axis angle

(b) Off-axis effect

Figure 2.3: Off-axis angle and its effect on the output spectrum.

corner pixel with an off-axis angle of 100mRad, out of a centre pixel with no off-axis effect. The wave number is set to be 1500 cm^{-1}. The off-axis correction algorithm must remap the spectra to their correct wave-number grids.

2.1.4 Imaging FTS and Hyper Spectral Image/Data Cube

Instead of using a single detector (which is the case of FTS), the imaging FTS uses an array of detectors. They are usually arranged in a rectangular or a square shape. This array of detectors is capable of acquiring high resolution spectral images over a specified area that can be recorded as hyper spectral images. Hyper spectral images are defined as being recorded in many, narrow, contiguous bands to provide information on the major features of the spectral reflectance of a given object. The images can be visualized as a 3-dimensional data set with two spatial and one spectral dimension, and the data set is therefore often referred to as an image cube. Hyper spectral data provide detailed information on the emission and absorption features of the spectral reflectance of a given object. Figure 2.4 illustrates the concept of a hyper spectral data set. It can be seen as a stack of spatial images over different spectral channels or as a stack of spectra arranged in an array of pixels. The upper left cube describes the frames in the time domain. When tracking a single spatial pixel in the axis of time, we will have the interferogram of that pixel. If this cube of data is transformed to the frequency domain where the Fourier transform will be applied to each spatial pixel along the time, it will result in a hyper spectral data cube. Because of the spatial-spatial-spectral dimensional nature of the hyper spectral data sets, they are often referred as image/data cubes. As stated in [47], the data that are extracted from the IFTS is correlated both spatially and spectrally due to the homogeneities of features covered by the surrounding pixels and the overlap of information across the adjacent channels [47, 24, 23].

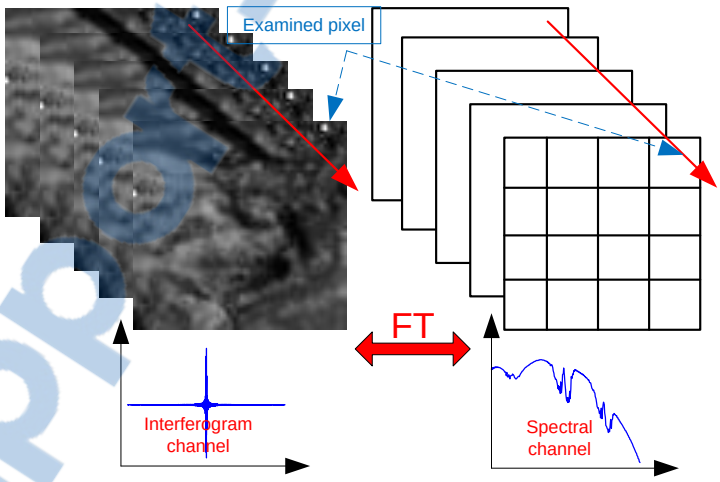

Figure 2.4: Hyper spectral image/data cube.

2.1.5 Calibration

Measurements obtained from a FTS suffer from the effect of the gain and offset factors of the instrument. For this reason, an instrument must be calibrated against some form of

reference so that measurements can be corrected using this calibration information [38]. The calibration process depends mainly on comparing the spectrum with two reference spectra that are generated from blackbodies. In this section we define the blackbodies and the calibration for IFTS data cubes.

Blackbodies

Blackbodies are bodies that emit or absorb all the radiation. They emit or absorb the maximum amount of radiation possible for a body at a specified temperature. They are a convenient baseline for radiometric calculations, since any thermal source at a specified temperature is constrained to emit less radiation than a blackbody at the same temperature [50]. Figure 2.5 shows blackbody curves at different temperatures.

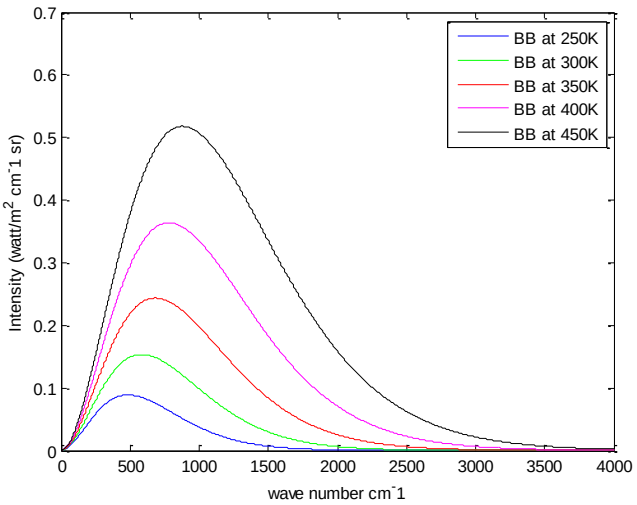

Figure 2.5: Blackbodies at different temperatures.

In 1900, Max Planck derived the theoretical solution that quantifies the blackbody radiation distribution. The Planck function expresses the radiance emission of a blackbody according to its wavelength as

$$B_\lambda(T) = \frac{2hc^2\lambda^{-5}}{e^{hc/\lambda KT} - 1} \tag{2.10}$$

where h is Plank's constant, c is the light velocity in m/sec, λ is the wavelength, T is the temperature in Kelvin, and k is Boltzmann's constant. The previous equation represents the blackbody radiation at a single wavelength. It may be preferred to work with wave number instead of wavelength. Wave number is a unit that can be related to the wavelength as $\sigma_{cm} = \frac{1}{100\lambda}$. The blackbody equation can be written as a function of wave number but the

energy integrated over both representations must be equal

$$B_\sigma(T) = \frac{2hc^2\sigma^3}{e^{hc\sigma/KT} - 1} \tag{2.11}$$

Calibrating the spectra

The raw data magnitude spectrum C_σ can be modeled as

$$C_\sigma = R_\sigma(L_\sigma + L_{\sigma 0}) \tag{2.12}$$

where C_σ is the observed raw spectrum from the scene, L_σ is the incident radiance, R_σ is the spectral responsivity of the instrument, and $L_{\sigma 0}$ is the instrument emission or the offset (that can be defined as the radiance which, if introduced at the input of the instrument, would give the same contribution as the actual emission from various parts of the optical train).

The calibration is usually done with the help of known radiance sources such as blackbodies. We use two blackbodies at cold and hot temperatures for calibration. The linear relationship written for both the hot and cold blackbody observed raw spectrum

$$C_c = R_\sigma(B_c + L_{\sigma 0})$$
$$C_h = R_\sigma(B_h + L_{\sigma 0})$$

can be solved to yield

$$\begin{aligned} R_\sigma &= \frac{(C_h - C_c)}{B_h - B_c} \\ L_{\sigma 0} &= \frac{C_h}{R_\sigma} - B_h \\ &= \frac{C_c}{R_\sigma} - B_c \end{aligned} \tag{2.13}$$

where B_h and B_c are the Planck blackbodies radiances for the hot and cold blackbodies, while C_h and C_c are the radiance from the known sources (physical blackbodies). From the previous equations and solving for a science target spectrum yields the basic calibration relationships

$$L_\sigma = \frac{C_\sigma}{R_\sigma} - L_{\sigma 0} \tag{2.14}$$

We apply the calibration equation on the spectra obtained from an IFTS data cube scanned at ABB Bomem. We scanned two blackbodies at cold and hot temperature for the calibration purpose. The IFTS scans a transparent container with Toluene gas. Figure 2.6 shows the spectra of toluene before (i.e., C_σ) and after (i.e., L_σ) calibration. Figure 2.7 shows a frame before and after calibrating all the spectra of the data cube each at its spatial location. We can see the effect of calibration that manages to eliminate the black circles at the center of the frame. This is important for the motion estimation algorithm that is used to align the frames generated from a moving IFTS instrument.

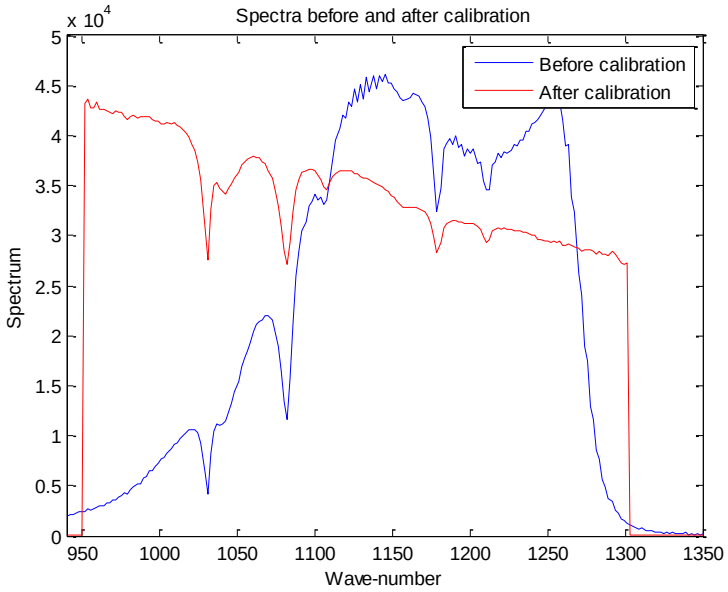

Figure 2.6: Spectra of toluene before and after calibration.

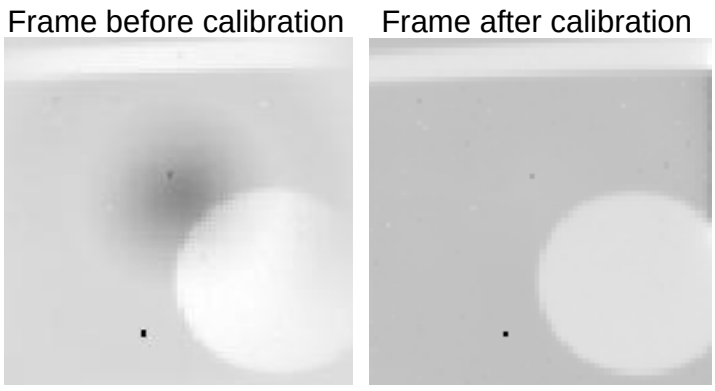

Figure 2.7: IFTS frame before and after calibration.

2.2 IFTS Data Cube Acquisition

In this section we discuss the methods to acquire IFTS data cubes that will be used in the thesis. We use a simulator to generate data in the long wave infra red (LWIR) and near infra red (NIR) bands. Also, we use experimental data cubes generated from IFTS instruments at ABB Bomem and Laval University. We generate both stationary and moving data cubes. Moving data cubes can have a relative global motion between the instrument and the targets, or more than one target moving in the scanned scene of the IFTS.

2.2.1 Simulated Data

A simulator has been designed in order to generate data cubes with varying characteristics. With the simulator, we can simulate target motion with different parameters for the IFTS (several gas spectra, integration area for the detectors, etc.)

The output of the simulator represents an array of detectors of an infrared camera. Each pixel in this camera gives a value related to the integration of the incident light from the IFTS on it. The dimension of this array can be varied. A schematic for the output layout of a frame is shown in Figure 2.8a. The integration in the detector is implemented by dividing each pixel to 100 sub-pixels then integrating their values. These sub-pixels can be adjusted afterward to put in consideration the area occupied by the electronics in the infrared camera (fill ratio). The red circles show the loci where the pixels have the same off-axis effect. For simplicity in some of the output generated cubes, the off-axis may be calculated one time only for each pixel location and its value is assigned to all the sub-pixels related to this pixel. An output frame representing two different targets is shown in Figure 2.8b. The red arrows show the direction of motion for the targets through the frames.

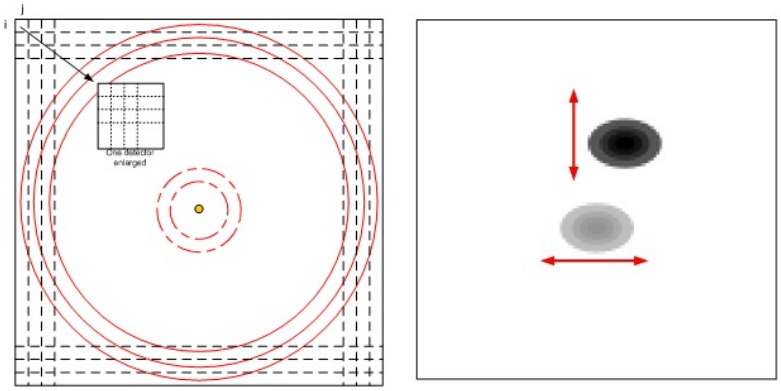

(a) Simulator output layout schematic (b) An output frame

Figure 2.8: The layout schematic and an output frame from the simulator.

A Target in Absorption or Transmission Mode in LWIR Band

In the scenario shown in Figure 2.9, a plume of gas in absorption or transmission mode is moving in front of a background. The background can be an instrumental blackbody or can be the Earth's surface or the Sun in the case of scanning the atmosphere. An example for this scenario in the absorption mode is a plume of carbon dioxide gas at a temperature less than the temperature of the background so the carbon dioxide absorbs the radiation. If the temperature of the carbon dioxide is higher than the temperature of the background, the carbon dioxide will be in the emission mode. We use this scenario for generating the data through out the thesis. The output radiance can be calculated as:

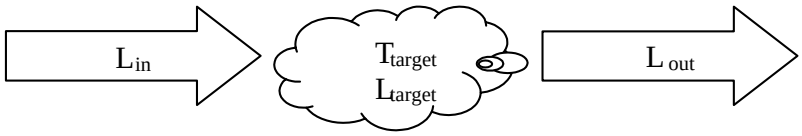

Figure 2.9: Scenario for a gas in absorption or transmission mode.

$$L_{out} = L_{in}T_{target} + L_{target}(1 - T_{target}) \tag{2.15}$$

where T_{target} is the target transmittance and depends on target temperature, length of the path in the target, target concentration, etc.; and L_{in} is the input radiance, L_{out} is the output radiance, and L_{target} is the blackbody radiance at the target temperature.

An output radiance for this scenario is shown in Figure 2.10 where carbon dioxide is simulated at a height of 6km above the Earth's surface at a temperature of 250K in front of a blackbody at temperature 300K, representing the Earth. We can see the absorption lines of the carbon dioxide. This setup can be extended to scanning two or more successive gases absorbing or transmitting as shown in appendix A.

A Target in the NIR Band

Working in the NIR range, we can assume that there is negligible emission from Earth's surface, so the radiation from the Sun that is transmitted through the column of the gas is reflected on Earth's surface toward the IFTS. The emission from the Sun in this spectral band is simulated from the spectral radiance of a blackbody at temperature 6000K according to Planck's equation. The reflectance of Earth's surface is simulated from NASA database [41] at this range and is normalized to 0.4 as a maximum reflection coefficient. The transmittance of CO_2 is computed from Hitran spectroscopic parameters. We use this setup to generate IFTS data cubes in the NIR band. More information about the setup is found in appendix A.

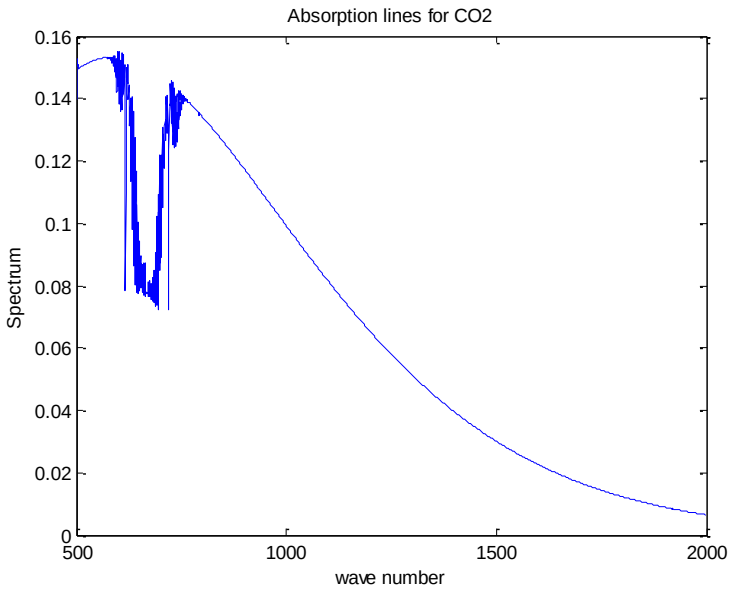

Figure 2.10: Simulated CO_2 in absorption mode.

2.2.2 Experimental Data

Two sources of experimental data cubes are used in this thesis: from an instrument of ABB Bomem and from SpIOMM (Spectrometre Imageur de l'Observatoire du Mont-Megantic) at Laval University.

ABB Bomem Experimental Data

An IFTS prototype working in the infrared range is used to acquire experimental data cubes at ABB Bomem. A blackbody radiates behind the target and the transmitted radiation is captured by a 16 bit thermal camera. The data cube contains nearly 8000 frames with dimension 64*64. The system is guided by a sinusoidal laser beam at frequency of 15,798 Hz. The detector IR signals are sampled at equal spaced intervals, so we can eliminate the sampling position error.

SpIOMM Experimental Data

SpIOMM is an imaging FTS for astronomy that was assembled in 2004 at Laval University. It was developed in collaboration with ABB Bomem, INO (Institut national d'optique), and the Canadian Space Agency. It is designed to be attached to a telescope for space and galaxy observation. There are successful observing runs using the SpIOMM at the observatoire du Mont Mégantic in southern Québec[16, 15, 11, 12]. SpIOMM operates in the visible range (350-900nm) with a circular field of view of 12 arcminutes in diameter. Its detector is blue-sensitive, liquid nitrogen-cooled with spatial resolution of 1340 x1300 pixels. The physics of

SpIOMM depends on the classical Michelson interferometer with two outputs ports. One port is only used and the interferogram is recorded by individual images at each OPD step. The interferometer is controlled with a laser-based servo system that is programmed to control the position of the mirror. The interferogram is sampled at a step size determined by the Nyquist criteria. The readout time of the detector is around 5 seconds. Figure 2.11 shows images taken in the laboratory at Laval University. The left image shows the SpIOMM instrument with the camera. The right image shows the set-up used to control the motion of the targets. A metal

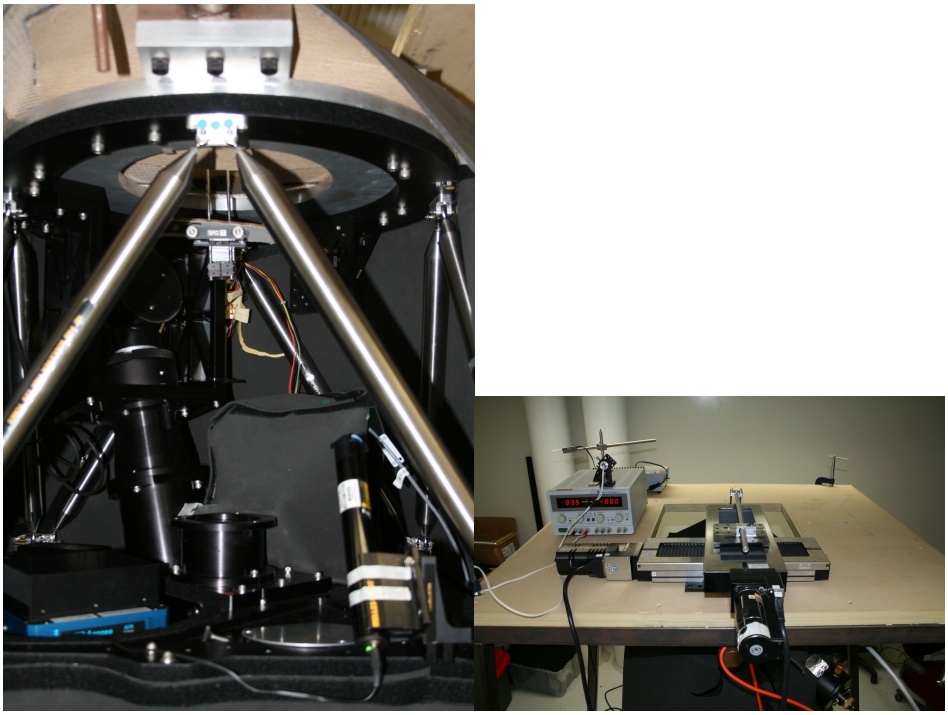

(a) SpIOMM instrument (b) Robots to move targets

Figure 2.11: Experimental setup for SpIOMM.

frame is supporting the SpIOMM in the vertical direction. To access the field of view, we designed a wood base with a square hole in the center and installed it on the top of the metal support as shown in the right of Figure 2.11. We combine two lamps to form the light source for the experiment: a wide spectrum argon lamp [2] including several peaks at the range of 700nm to 900nm, and a halogen lamp with a continuous spectrum from 300nm to 900nm. This combination creates a light source with wide continuous background and sharp peaks. We install a resolution target or visible filters in front of the field of view. The light emitted from the lamps is reflected by the ceiling then passed through the filters or the resolution target to reach the camera. Figure 2.12 shows the frequency response of the filters. We use the filters with cut-off frequency at 715nm and 1000nm in our experiments. All the system is covered with black heavy cloth to isolate it from the surrounding light.

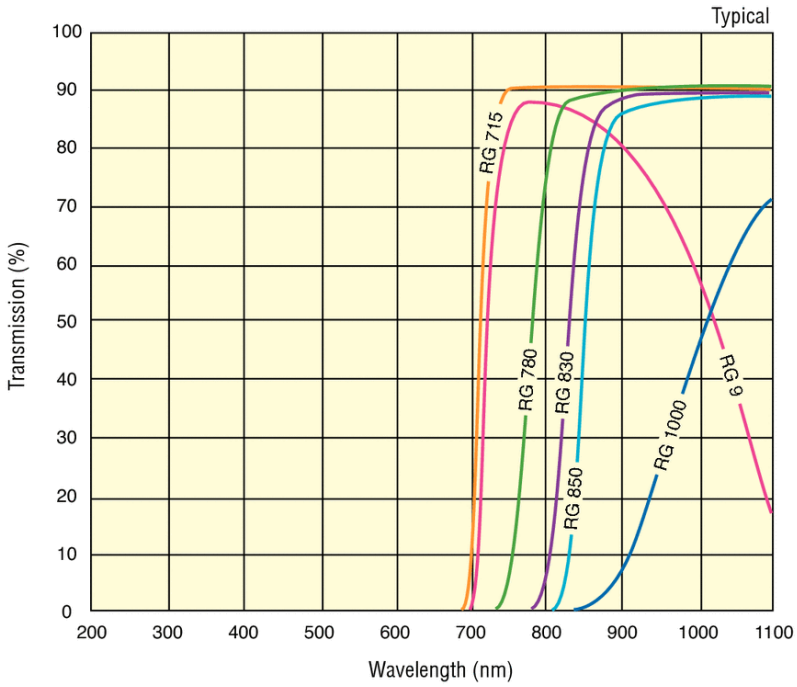

Figure 2.12: Frequency response of filters.

2.3 Conclusion

In this chapter we presensted a fast review for FTS and IFTS technology. We discussed spectral resolution, off-axis distortion and spectral calibration that will be used in this thesis. We end the chapter with data cube acquistion both simulated and experimental.

Chapter 3

Motion Correction

This chapter defines the problem and the effect of acquiring a data cube from a moving IFTS. As a result of acquiring a hyper-spectral cube from a non stationary IFTS, the output spectra have degraded spectral resolution and accuracy. The chapter covers the concepts of optical flow techniques and classifies them according to the performance under the brightness variation. Applying the optical flow techniques on simulated and experimental data cubes of IFTS is presented.

3.1 Problem Illustration for Motion

This section describes the effect of motion on the output spectra of IFTS. We examine two cases, a global relative motion between the instrument and the target, and the case with more than a target moving in the field of view of the IFTS.

3.1.1 Defining Problem with a Single Moving Target

For a given data cube with no relative motion between the instrument and the scene, the interferogram of each spatial location is constructed from the samples along the OPD axis (scanning axis) of the spectrometer. However, for a cube with a relative motion between the instrument and the scene, the samples of the interferogram are not related to the same spatial location. The interferograms are constructed from samples of different spatial locations according to the relative motion between the instrument and the target. The upper part of Figure 3.1 shows how the samples of the interferogram are constructed in the case of relative motion. Along the selected OPD axis, the samples of the interferogram start at a spatial location corresponding to a target labelled "1". While scanning, the samples of the interferogram are not always related to the target due to the motion. They are related to other spatial location while the locations of the target are indicated by locations "2,3,4". We need to align the frames of the spectrometer in the case of relative global motion to achieve a realigned cube with frames as shown in the lower part of figure 3.1. In the realigned cube,

the samples of the constructed interferogram are contributed by the spatial locations "1,2,3,4" that are always related to the same target.

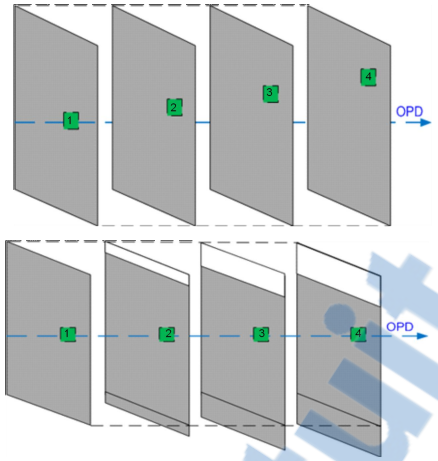

Figure 3.1: Problem with a single moving target.

3.1.2 Defining Problem with Multiple Moving Targets

Consider two targets A and E with dimensions one by one pixel as shown in Figure 3.2a. The target located at pixel A is stationary and the other target located at pixel E is moving to pixel location H, K, and L in frames 2, 3, and 4 respectively. Along the OPD axis of pixel A, we find the interferogram samples related to the same pixel location in the next frames. While along the OPD axis of pixel E, the interferogram samples are related to other spatial areas that occupy this place. Our goal is to track the target along the frames, so when we reconstruct the interferogram for pixel E, it contains samples from pixel H in the second frame, pixel K in the third frame, and pixel L in the fourth frame. Tracking target E along the frames gives

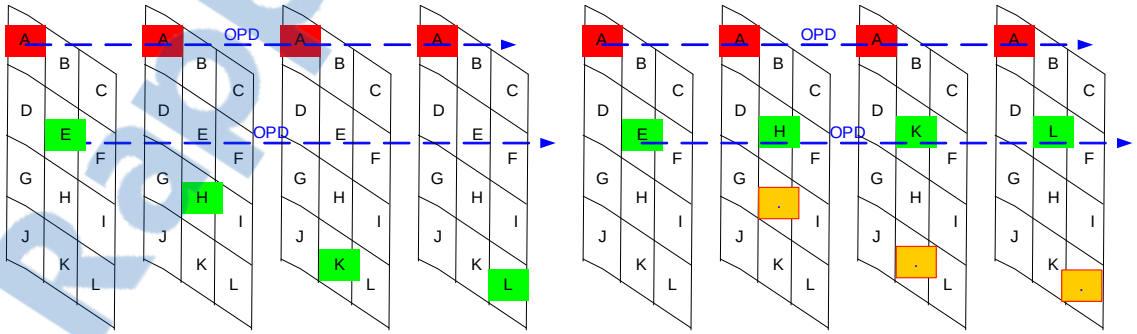

(a) Before correction (b) After correction

Figure 3.2: Non stationary targets before and after motion correction.

an interferogram constructed from samples always related to the same target. We need to construct another cube contains interferograms each with samples related to the same spatial location. Figure 3.2b shows the cube after correction.

3.1.3 Effect of Motion on the Interferogram and Spectrum

To examine the effect of motion on the interferogram and the spectrum, we consider a scene that is a background of a blackbody at 300K , and a CO_2 target at 250K in absorption mode. This scenario represents a carbon dioxide gas at height of 6 km over the earth's surface which is scanned in front of the surface of the earth. The target moves from the lower right corner to the upper left one in a step of 0.1pixel/frame. We simulate a grid of the output detectors of 128x128 pixels with 1000 frames. The ZPD is at frame 501. We ignore the noise and shear effect while setting a maximum off-axis angle of 0.04 Rad. The output sample is a 16 bit pixel to simulate the infrared camera. The sensor operating band is between 500-2000 cm^{-1} wavenumber. The sampling rate is twice the maximum frequency of the input spectrum. We track the interferogram of the pixel located at the border of the CO_2 column of gas. We compare this pixel with another pixel in a stationary cube. Figure 3.3 shows the effect of motion on the interferogram and the spectrum. From the scanned interferogram of the moving target, we recognize that the samples on the OPD are related to the background at the beginning of the scan till the area around the ZPD. The intensity of the background samples is higher than the intensity of the samples of the target because the target is in the absorption mode. Around the ZPD, the samples are related to the CO_2, then the samples are related to the background when moving further along the OPD. Most of the information is placed around the ZPD. The far OPD affect mainly the resolution of the spectrum. We can see the errors (i.e low resolution) in the spectrum obtained from the moving target when compared to the spectrum obtained from the non moving target. The goal is to correct for the motion in order to maintain a useful or a high resolution spectrum representing the target.

3.1.4 Motion Compensation

In order to obtain high spectral accuracy, the scene has to be stationary in the field of view of the IFTS for the complete acquisition time of the data cube. This condition may not be fully met for some applications. Due to the relative motion between the instrument and the scene being scanned, the interferogram of a given pixel is composed of data samples coming from different sub-areas of the scene, leading to corrupted spectra when Fourier transformed. In airborne FTS imagers, the motion compensation is done using opto-mechanical means to get the interferogram samples from the same spatial location. We propose to perform motion compensation a posteriori using the data information. We use motion estimation techniques to recover the undistorted spectra. This will compensate for the unpredictable motion where the opto-mechanical means fail, and will not add to the hardware complexity.

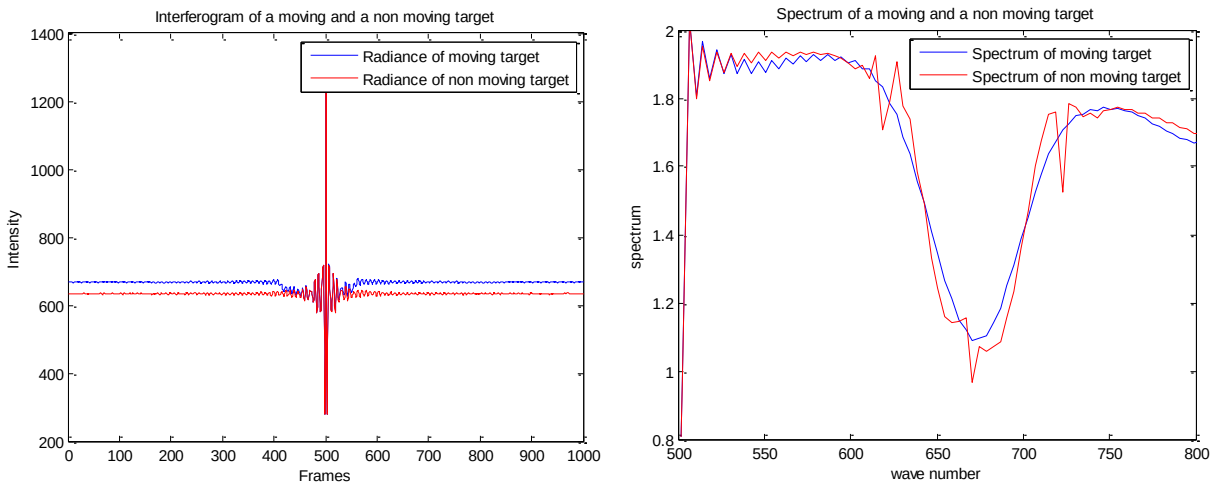

Figure 3.3: Monochromatic off-axis correction.

3.2 Review for Motion Estimation Techniques

In this section we review motion estimation techniques, and divide them to two categories according to our data. We fully discuss the techniques that are suitable for our data and discuss the modification if any.

Optical flow has been commonly described as the apparent motion of brightness patterns in an image sequence. Computation of optical flow is known as the problem of estimating a displacement field $[dx, dy]$ for transforming the brightness patterns from one frame to the next in the data cube. It is critical to choose an appropriate constraint equation that accurately represents the significant events in a dynamic scene. Optical flow can be induced by the relative motion between the camera and a scene. However, it may also exist, in the absence of camera and/or scene motion, due to other events such as a light source [34].

Recovering the 2-D velocity field from a sequence of intensity images is an ill-posed problem. The problem is ill-posed because local intensity alone fails to completely generate the motion information. For example, in regions of constant intensity, motion cannot be detected and an infinite number of solutions exist. Even when the intensity is constant in a given direction, the solution is still only partially available. Under such conditions, it is only possible to provide the component of the solution that is perpendicular to the given direction. This is referred to as the aperture problem [21]. Because the problem of recovering the 2-D velocity is ill-posed, additional information must be added to the problem statement to clearly define a closed set in which a single stable solution exists.

IFTS output frames are challenging from the point of view of motion estimation techniques. They have a temporal change that is related to the interferogram intensity of the pixels that

varies along the OPD axis and can be related to non-uniform illumination problem in the video sequence literature. The interferogram has its maximum at the ZPD, then it decreases to the side-lobes taking the shape of an auto-correlation function. We may divide the methods for motion estimation or optical flow techniques to two categories. The first category is the one that employs brightness constancy, where it is assumed that the image brightness of a scene point remains constant or approximately constant from one frame to the next. The second is that which allows the brightness variation of a surface. The scene dynamical events induce both geometric and radiometric variations in time-varying image. This category is suitable for our data cube where the geometric variation can be related to the relative motion between the instrument and the scene, and the radiometric variation can be related to the interferogram intensity change.

3.2.1 Methods with Brightness Constancy

As a pixel at location (x, y, t) with intensity $E(x, y, t)$ moves by $(\delta x, \delta y, \delta t)$ between two frames in a data cube, we can apply the following equation :

$$E(x + \delta x, y + \delta y, t + \delta t) = E(x, y, t) \tag{3.1}$$

Assuming the motion to be small enough, and using the Taylor series expansion up to the first order term for the left hand side, we can rewrite the equation as :

$$E(x + \delta x, y + \delta y, t + \delta t) = E(x, y, t) + E_x \delta x + E_y \delta y + E_t \delta t \tag{3.2}$$

That follows :

$$E_x \delta x + E_y \delta y + E_t \delta t = 0 \tag{3.3}$$

where, $[E_x, E_y, E_t]$ is the image gradient in the spatio-temporal volume. This can be also written as :

$$\bigtriangledown E(X, t) \cdot V + E_t(X, t) = 0 \tag{3.4}$$

where $V = (\frac{\delta x}{\delta t}, \frac{\delta y}{\delta t})^T$. This is an equation with two unknowns that is referred to the aperture problem of the optical flow algorithm, so another set of equation is needed, given some additional constraints. In this section, we describe some methods that can be considered under this category.

Lucas-Kanade Method

Lucas technique [28] takes advantage of the fact that in many applications, the two images are already in approximate registration. They assumed that the flow is constant in a small window, so there will be more than two equations for the two unknowns and thus the flow can be determined using the least squares method to solve the over-determined system of equation.

Equation 3.4 can be arranged as follows

$$\begin{bmatrix} E_{x1} & E_{y1} \\ E_{x2} & E_{y2} \\ ..... & ..... \\ E_{xn} & E_{yn} \end{bmatrix} \begin{bmatrix} V_x \\ V_y \end{bmatrix} = - \begin{bmatrix} E_{t1} \\ E_{t2} \\ ..... \\ E_{tn} \end{bmatrix} \tag{3.5}$$

Solving the equation using least mean square method gives the two optical flow parameters

$$V = (A^T A)^{-1} A^T (-b) \tag{3.6}$$

where, A is the spatial derivative matrix, and b is the vector containing the temporal derivatives. Lucas-Kanade method is simple and fast, and also robust in the presence of noise. But it has many disadvantages. The assumption of constant illumination is not usually right for the different scenarios. It cannot fill the missing flow information in the inner parts of homogeneous objects. It cannot recover the aperture problem.

Horn-Shunk Method

Horn-shunk introduces a global constraint of smoothness on the velocity [22]. It combines the gradient constraint that is in equation 3.4 with a global smoothness term to constrain the estimated velocity field V. Minimizing the equation:

$$\int_D (\bigtriangledown E(X,t) \cdot V + E_t(X,t))^2 + \lambda^2(|\bigtriangledown u|^2 + |\bigtriangledown v|^2) dX \tag{3.7}$$

defined over a domain D, where the parameter λ is a regularization constant that reflects the influence of the smoothness term. Iterative equations are used to minimize the previous equation and obtain image velocity:

$$\begin{aligned} u^{n+1} &= u^{-n} - E_x \frac{E_x u^{-n} + E_y v^{-n} + E_t}{\lambda^2 + E_x^2 + E_y^2} \\ v^{n+1} &= v^{-n} - E_y \frac{E_x u^{-n} + E_y v^{-n} + E_t}{\lambda^2 + E_x^2 + E_y^2} \end{aligned} \tag{3.8}$$

where n denotes the iteration number,u^{-n} and v^{-n} are neighbourhood averages of u^{n+1} and v^{n+1}. Horn-Shunk method is more complicated than the Lucas-Kanade method. We need to average the neighbourhood velocity at each step. The results also depend on the regularization constant that can be varied. An advantage of this method is the filling of the missing flow information from the motion boundaries. Horn-Shunk method can generate reasonable results in the case of brightness variation by adding the rate of change of image brightness to the error to be minimized. However, we can not consider it among the methods allowing the brightness variation because it still depends on the brightness constancy hypothesis.

Region-Based Matching

The idea of region matching algorithms is to divide the frame into many blocks where each block is compared with the corresponding block and its adjacent neighbours in the previous or successive frame. In that way, the motion vector can estimate the movement of a block from one location to another. This matching algorithm has been implemented using many techniques starting from the full search one. This technique matches all possible displaced candidate blocks within the search area in the reference frame, in order to find the block with the minimum distortion. There are other techniques that try to achieve the same performance doing as little computation as possible like the three step search, four step search, diamond search, and the cross diamond one [25, 36, 8, 46].

3.2.2 Methods with Brightness Variation

The second category of methods allows the brightness variation of a surface. The scene dynamical events induce both geometric and radiometric variations in time-varying image. This category is suitable for our data cube where the geometric variation can be related to the relative motion between the instrument and the scene, and the radiometric variation can be related to the interferogram intensity change.

There are several methods that can describe this category. Some of these methods are described below.

Phase-based Method

Harold [44] proposed a sub-pixel algorithm for image registration based on the relative phase between two images. Computed using 2D discrete Fourier Transforms, the relative phase is a plane whose slope gives the 2D motion between the frames. Let $f_1(x, y)$ and $f_2(x, y)$ be the two frames for which we need to estimate the motion vector (x_o, y_o) between them, where $f_2(x, y) = f_1(x - x_0, y - y_0)$. According to the Fourier shift property

$$\hat{f}_2(u, v) = \hat{f}_1(u, v)exp(-i(ux_0 + vy_0)) \quad . \tag{3.9}$$

We compute the complex ratio of

$$\hat{C}(u, v) = \frac{\hat{f}_2}{\hat{f}_1} = exp(-i(x_0u + y_0v)) \tag{3.10}$$

so the linear phase difference between the two frames is given by

$$\hat{\phi}(u, v) = \angle\hat{C}(u, v) = x_0u + y_0v \quad . \tag{3.11}$$

This is a planar surface through the origin, from which the slopes can be estimated from the least squares regression law; these slopes are the translation in the spatial domain.

To apply this algorithm, we start by registering the frames to the nearest integral pixel coordinates. A Blackman or Blackman Harirs window is applied in the pixel domain to eliminate image boundary effects in the Fourier domain [18]. Then, we calculate the discrete Fourier transform of $f_1(x, y)$ and $f_2(x, y)$. The vector (x_0, y_0) can be estimated using the least squares regression law from the complex ratio image.

Mutual information method

One of the effective algorithms for registering the images under the intensity inconsistency is the mutual information (MI). MI appeared in many domains as shown in [13, 6, 26]. This technique has its roots in the information theory [9].

Define two random variables, A and B, that have a marginal probability mass functions $P_A(a)$ and $P_B(b)$, and a joint probability mass function $P_{A,B}(a, b)$, the mutual information (MI), $I(A, B)$, measures the degree of dependence of A and B by measuring the distance between the joint distribution $P_{A,B}(a, b)$, and the distribution associated with the case of complete independence $P_A(a).P_B(b)$, by means of the relative entropy or the Kullback-Leibler measure [49], i.e.

$$I(A, B) = \sum_{a,b} P(a, b) log \frac{P(a, b)}{P(a).P(b)} \tag{3.12}$$

And MI is related to the entropy by the following equations

$$\begin{aligned} I(A, B) &= H(A) + H(B) - H(A, B) \\ &= H(A) - H(A|B) \\ &= H(B) - H(B|A) \end{aligned} \tag{3.13}$$

where $H(A, B)$ is the joint entropy, $H(A), H(B)$ are the entropies for A and B respectively, and $H(A|B)$ and $H(B|A)$ the conditional entropies of A given B and that of B given A, and their definitions are as follows

$$\begin{aligned} H(A) &= -\sum_{a} P_A(a) log P_A(a) \\ H(A, B) &= -\sum_{a,b} P_{A,B}(a, b) log P_{(A,B)}(a, b) \\ H(A|B) &= -\sum_{a,b} P_{A,B}(a, b) log P_{(A|B)}(a|b) \quad . \end{aligned} \tag{3.14}$$

To apply the MI concept to the images registration domain, each probability distribution mentioned before must be given a definition related to the image intensity values. A two

dimensional joint histogram h is defined as a function of two variables, A, and B that are the gray level intensities in the two images needed to be registered. Each value h at the entry (A, B) is the number of corresponding pairs having gray-level A in the first image and gray-level B in the second one. Estimation for the joint probability distribution$P_{A,B}(a, b)$ are obtained by normalizing the joint histogram of the image pair as

$$P_{A,B}(a,b) = \frac{h(a,b)}{\sum_{a,b} h(a,b)} \tag{3.15}$$

And the two marginal probability mass functions can be obtained from

$$\begin{aligned} P_A(a) &= \sum_b P_{A,B}(a,b) \\ P_B(b) &= \sum_a P_{A,B}(a,b) \end{aligned} \tag{3.16}$$

Intensity a in the floating image and b in the reference image are related through the geometric transformation T. The MI similarity measure states that the images are geometrically aligned by transformation T when MI is maximal. During the transformation process, the grid points of the floating image will not always coincide with that of the reference one, so, it is required to interpolate to determine the intensity values of non-grid points.

Applying this technique in the sub-pixel image registration is time consuming. Moreover, we have no local maximum for the MI registration technique between two images. Also, the accuracy of the technique depends on the window size where the MI is performed. Due to the previous factors, it may be preferred to use the MI algorithm for pixel registration and using another one for the sup-pixel registration.

GDIM Method

The general and challenging version of optical flow techniques is to estimate the motion at each pixel. This includes estimating the motion vectors of more than a target moving in different directions. We need also to minimize the brightness difference between the corresponding pixels. In this section we discuss a method presented by Negahdaripour [34] that we use through the thesis to estimate the motion at each spatial location in the frames of IFTS. This technique can be compared to the block matching technique discussed in the previous section but with the ability to work under illumination variation.

Negahdaripour [34] proposed the Generalized Dynamic Image Model (GDIM) to decouple image transformations into the geometric components related to the displacement in both directions and into the radiometric component that is related to the illumination variation. As the image brightness will vary by $\delta e(r) = e(r + \delta r) - e(r)$ where $r = [x, y, t]^T$, and $e(r)$

denotes the image brightness of some scene point, he defined $\delta e(r)$ in terms of multiplier and offset parameters as $\delta e(r) = \delta m(r)e(r) + \delta c(r)$ He then assumed that the unknown motion vectors are constants within a small spatial region (spatial smoothness constraint) taken to be a square window centered at each image point. A least-squares formulation is then employed to estimate the motion vectors and the two parameters of the radiometric component. Negahdaripour minimized the sum of squared errors over the small region and showed that the parameter values $(\delta x, \delta y, \delta m, \delta c)$ can be estimated from

$$\sum_W \begin{bmatrix} e_x^2 & e_x e_y & -e_x e & -e_x \\ e_x e_y & e_y^2 & -e_y e & -e_y \\ -e_x e & -e_y e & e^2 & e \\ -e_x & e_y & e & 1 \end{bmatrix} \begin{bmatrix} \delta x \\ \delta y \\ \delta m \\ \delta c \end{bmatrix} = \sum_W \begin{bmatrix} -e_x e_t \\ -e_y e_t \\ e e_t \\ e_t \end{bmatrix} \tag{3.17}$$

where W is the neighbourhood region, e is the pixel intensity, and $e_a = \delta e/\delta a$. This computation is repeated for each image point. By solving the previous matrix, we can get the motion vectors in both direction between two frames in the IFTS cube. The multiplier and offset for the image brightness are also obtained. We describe in Appendix B two modifications we made to this algorithm to improve the results when used on interferogram frames.

Computing the Optical Flow with Physical Models of Brightness Variation

Horst et al tried to describe a formulation based on models of brightness variations that are caused by time-dependent physical processes that yields a generalized brightness change constraint equation [19].

$$\bigtriangledown E(X,t).V + E_t(X,t) = f(E_0, t, a) \tag{3.18}$$

where, $V = (\frac{\delta x}{\delta t}, \frac{\delta y}{\delta t})^T, f(E_0, t, a) = \frac{d}{dt}[h(E_0, t, a)], h$ is a parameterized function along which brightness can change, E_0 denotes the image at time 0, and a denotes a parameter vector for the brightness change model. Horst proposed a formula for the h function for many cases like exponential decay, diffusion, and moving illumination envelope.

3.3 Simulated Data

In this section we apply the motion estimation techniques previously discussed on simulated data to register the frames of an IFTS. We use two simulated data cubes. The first cube contains a global relative motion between the instrument and the scanned scene, while the second cube contains more than a target moving in different directions. We end by obtaining a high resolution spectra from the IFTS after registering the frames according to the motion vectors generated from the motion estimation techniques.

3.3.1 Single Target Scenario

A global motion exists between the instrument and the scanned scene. We simulated a data cube that contains a column of CO_2 scanned by a non stationary IFTS. We use the phase-based and the MI techniques to generate the motion vectors needed to align the frames of the IFTS [29, 30, 35, 31].

Data Cube Acquisition

For the NIR range, we can assume that there is negligible emission from earth's surface, so the radiation from the sun that is transmitted through the column of the gas is reflected on earth's surface towards the IFTS. The emission from the sun in this spectral band is simulated from the spectral radiance of a blackbody at temperature 6000K according to Planck's equation [27]. The IFTS is assumed to be placed on a plane scanning the column of gas at a height nearly 2 km above earth's surface. The column of gas has an elliptical shape of CO_2 for simulation purpose, with a maximum concentration of 380 ppm at the centre and decreasing gradually to the edges, and the operating band for the IFTS sensors is between 6000-6500 cm^{-1}. The reflectance of earth's surface is simulated from a NASA database [41] at this range and is normalized to 0.4 as a maximum reflection coefficient. The CO_2 transmittance is obtained from Hitran spectroscopic database [3]. Figure 1 shows the setup for the mentioned scenario. The hyper-spectral cube we generate has 8000 frames of 64 x64 pixels, with a $1.75cm^{-1}$ spectral resolution. The sampling rate or the minimum OPD step is set to twice the maximum wavenumber (7000 cm^{-1}). For simplicity and to focus on the motion estimation performance, we assumed there is no off-axis effect or shear errors due to interferometer misalignment. The instrument is moving according to the motion pattern shown in Figure 3.4. This pattern is repeated every 1000 frames, while each path represented by an arrow lasts for 100 frames. At ZPD (frame 4001), the target is located at the lower right corner in the scene. On the right side of the figure, examples of the output frames are shown.

Registration using Motion Estimation

Motion compensation on the interferograms is difficult for two reasons. First, the intensity of the interferogram varies with the OPD. Second, the intensity variation is not spatially uniform since we are looking at scene elements with different electromagnetic spectrum. Therefore, motion registration techniques based on constant intensity cannot be used to register the frames. Most motion registration techniques robust to intensity variation also assume, however, uniform spatial variation. In this section, we use the phase-based method to compute the motion compensated cubes. Then, we combine the phase-based and the mutual information algorithms to compute motion compensated cubes from which spectra information can be retrieved. We compare between the two results.

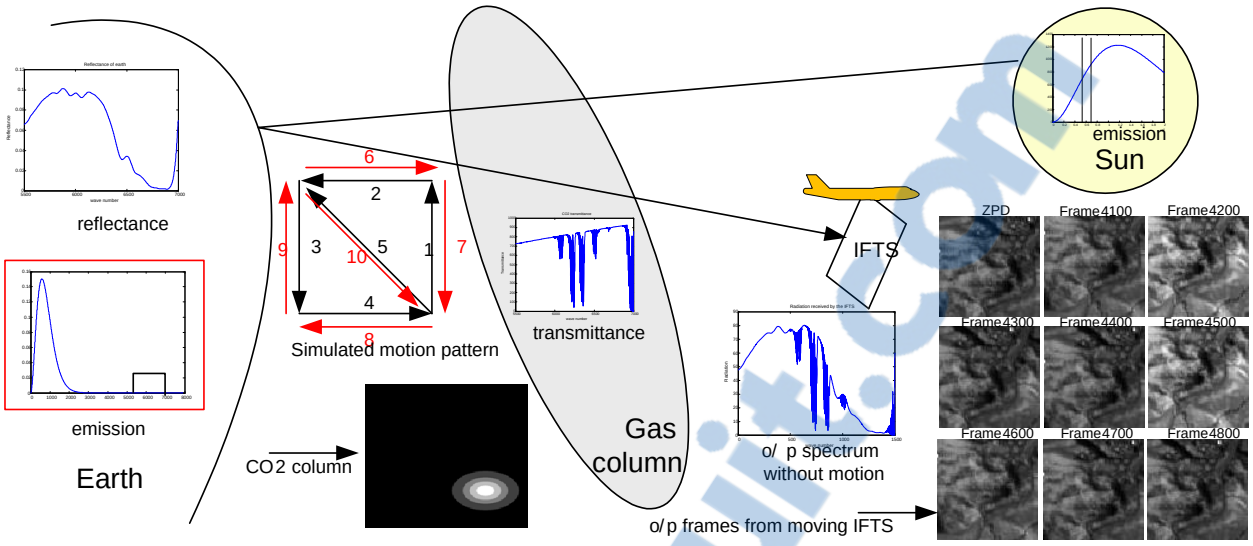

Figure 3.4: Setup for IFTS scanning a target in NIR band.

Both methods can work under illumination variation. However, MI is more robust to illumination variation that is not spatially uniform, which is the case in our scenario, mainly around the ZPD frames. The phase-based method is much faster than the MI with a higher accuracy. As the phase-based is a sub-pixel technique, we need to estimate the motion vectors between each two successive frames along the OPD and sum up the results. This introduces error accumulation. So, we register the frames using the MI with the ZPD as a reference for pixel precision, then use the phase-based algorithm for the sub-pixel registration. We refer to this algorithm as the mixed method. The accumulation of errors in the motion vectors is stopped since we estimate motion relatively to the ZPD frame. Figure 3.5a and b shows the accumulated motion vectors for both the phase-based and mixed method compared to reference motion vectors used to move the target. Zooming on certain motion vectors shows the benefit of using the mixed method. The motion vectors generated from the mixed method algorithm are well aligned with the reference motion vectors. Figure 3.5c and d show the error in the motion vectors in both directions generated from both methods. When using the mixed method, there is no error accumulation since the vectors are estimated relatively to the ZPD.

In order to illustrate the effect of motion on the shape and resolution of the output interferogram and spectrum, we tracked the interferogram samples for a pixel located at the border of the CO_2 column, and computed its spectrum. We compared them with the interferogram and spectrum coming from the same pixel but from a data cube with stationary CO_2 column. The green curves in Figures 3.6 and 3.7 are related to the non-stationary data, while the black ones are computed from the stationary data.

The interferogram radiance (green curve) oscillates since it captures radiance from different

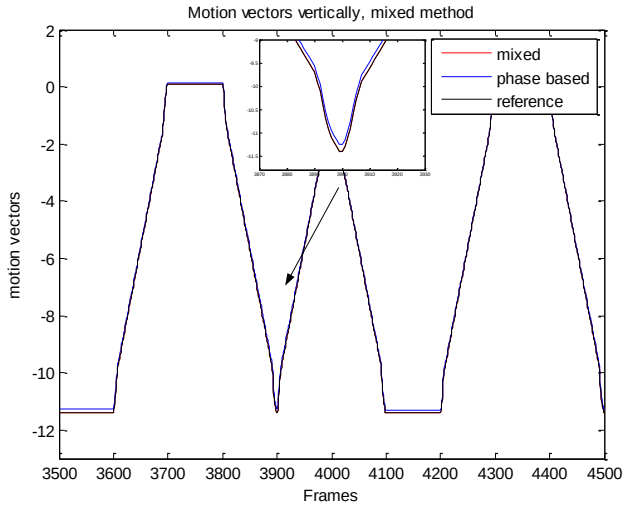

(a) Vertical

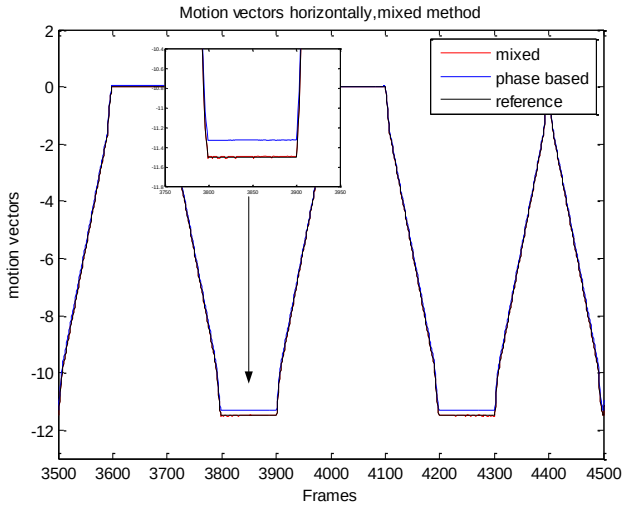

(b) Horizontal

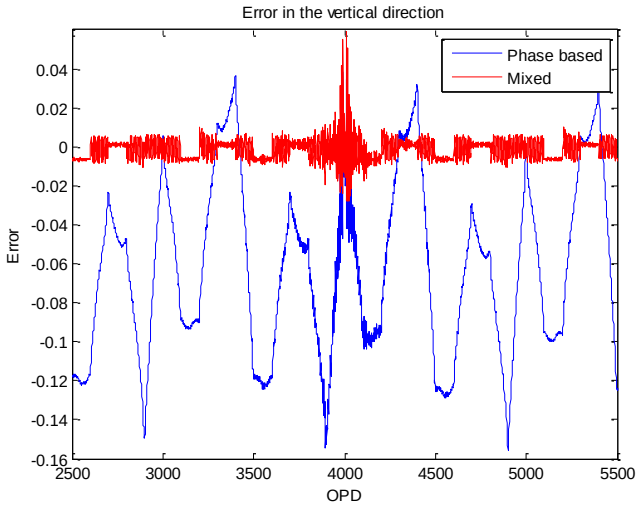

(c) Vertical

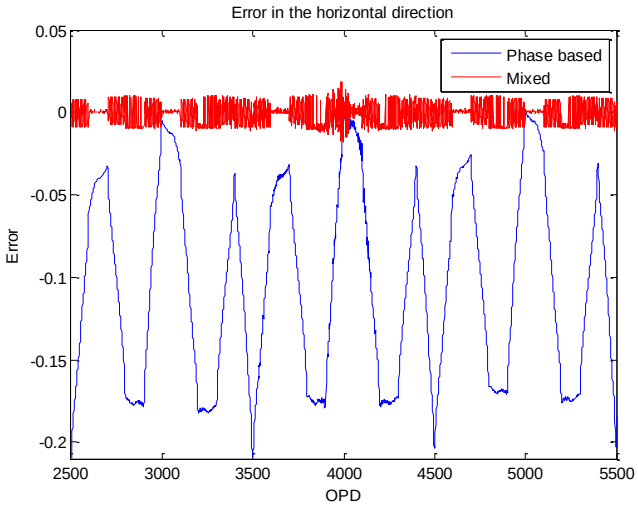

(d) Horizontal

Figure 3.5: Motion vectors for both methods and the error generated from each method.

spatial scene elements as shown in Figure 3.6. The interferogram related to the phase-based method (blue curve) appears to oscillate around the ZPD, while the interferogram of the mixed method (red curve) coincides with that of the known one. Figure 3.7 shows that the

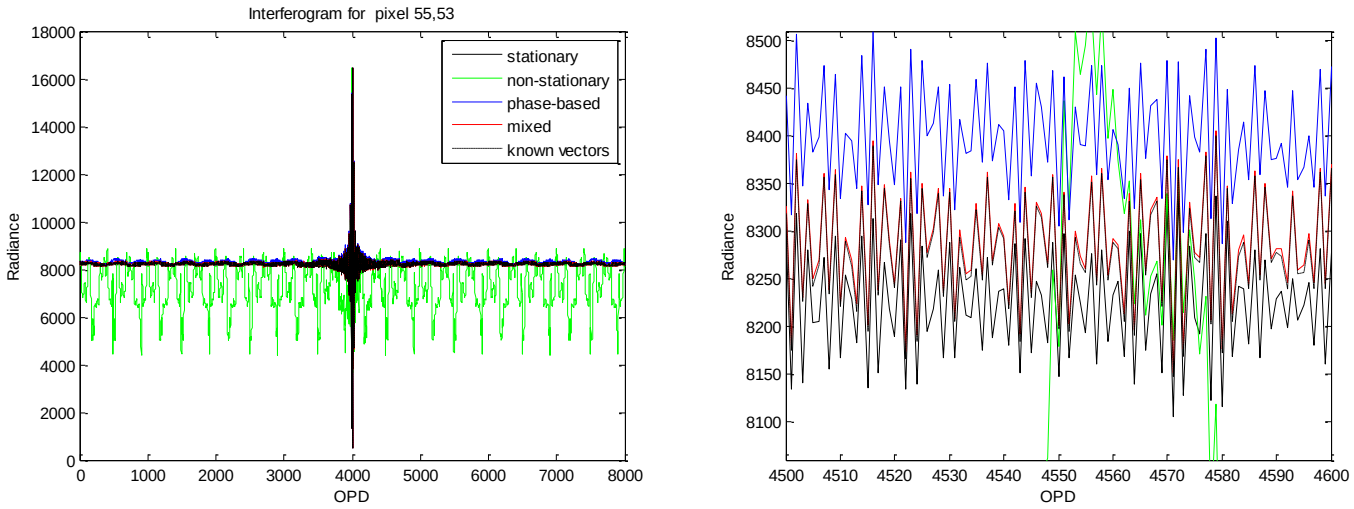

(a) Interferograms

(b) Zoomed

Figure 3.6: Interferograms for carbon dioxide at NIR.

mixed method improves the resolution of the output spectrum, which matches the spectrum of the pixel assuming known motion vectors. Note that the difference between the spectrum computed using the known motion vectors and the ground truth (stationary) is caused by the interpolation errors. Figure 3.7 also shows a zoom at the wavenumbers where the CO_2 absorbs. For comparing two spectra, the SNR is calculated as follows [47]

$$SNR = 10log\frac{\sum_{k=0}^{N-1}|S_1(K)|^2}{\sum_{k=0}^{N-1}|S_1(K)-\hat{S}_1(K)|^2} \tag{3.19}$$

where S is a spectrum, $\hat{S}$ is a reference spectrum, K is a wavenumber in the spectrum, and N is the total number of points on the axis of spectrum.

It may be preferred to compute and compare the average SNR for several spectra for each point on the spectrum curve. This enables us to have a more stable result for the SNR, and to follow the shape of the SNR curve versus different wavenumbers, where, it may be more important to have a high SNR in the sensor operating band for the examined material. Computing the SNR for the spectra shows improved results for the mixed method over the phase-based method as shown in Figure 3.8. The SNR reference spectra were computed after aligning the frames using the known motion vectors. Zooming on certain bands are shown for better examination. These results show the benefits of using the motion estimation technique to align the frames of non-stationary IFTS. This technique gives output spectra with reduced

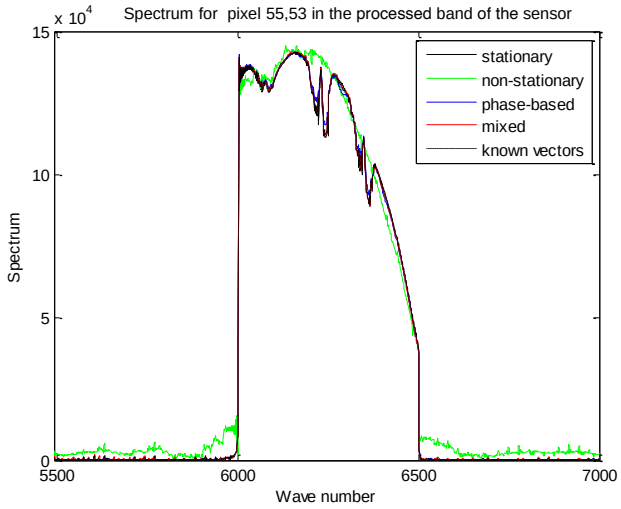

(a) Spectra

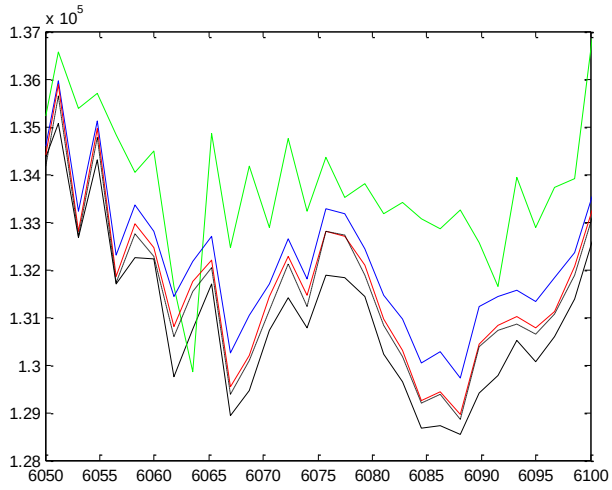

(b) Band 6050-6100

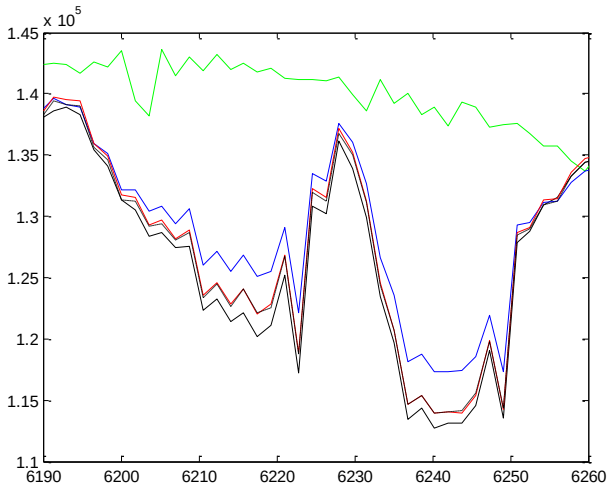

(c) Band 6190-6260

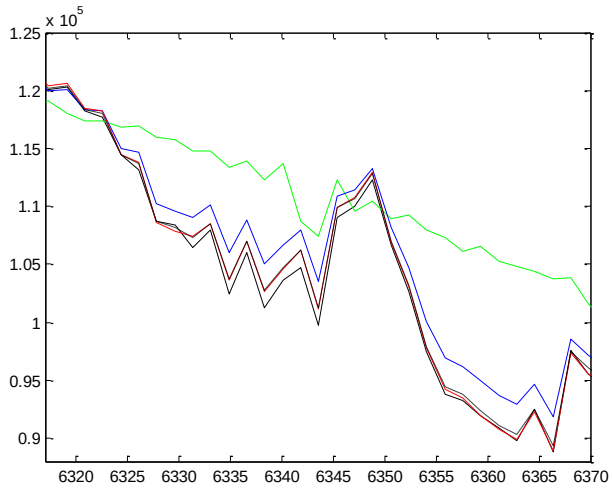

(d) Band 6320-6370

Figure 3.7: Spectra for carbon dioxide at NIR.

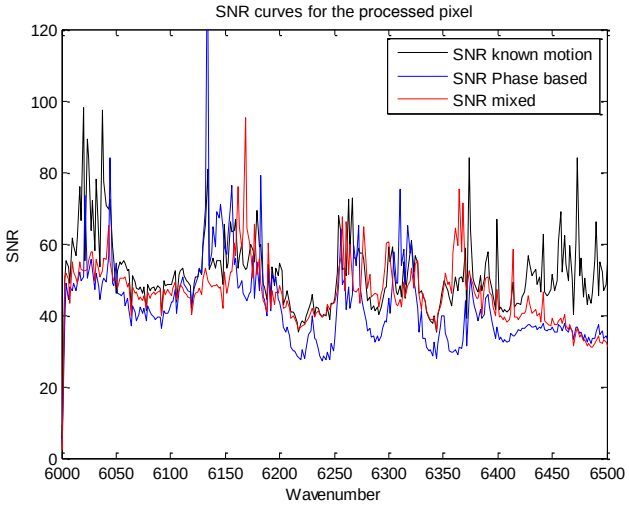

(a) SNR

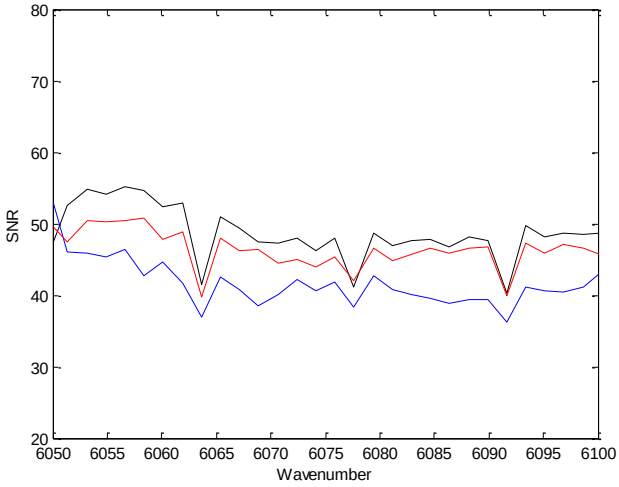

(b) Band 6050-6100

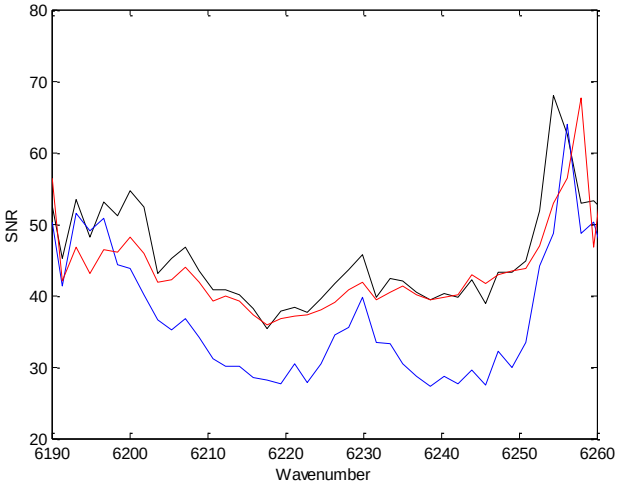

(c) Band 6190-6260

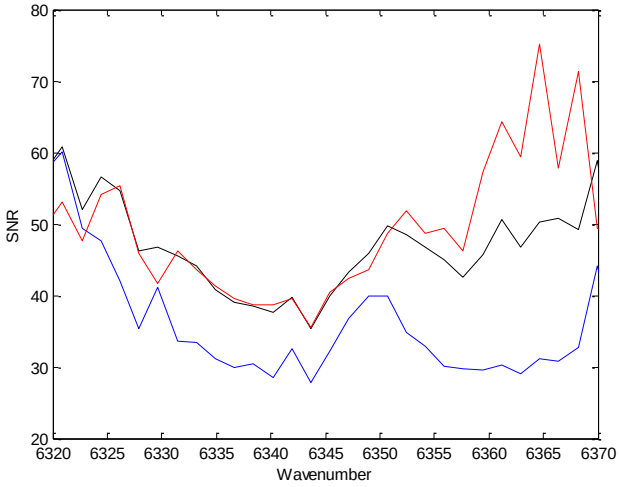

(d) Band 6320-6370

Figure 3.8: Spectra for carbon dioxide at NIR.

errors as well as with a recognized increase in the SNR. The results also show that mixing the MI and phase-based algorithms helped reducing the errors, improving the output spectra and increase the SNR.

Delimiting the Shape and Location of the Column in the Scene

After alignment of the frames and FFT of the interferograms, each frame will be related to a certain wavenumber, where each spatial location in it corresponds to the intensity of the spectrum of the pixel at this wavenumber. As the CO_2 has high absorption around wavenumbers 6216, 6247, and 6366 cm^{-1} in the NIR range. The frames related to these wavenumbers in the cube of spectra are shown in Figure 3.9 before and after the alignment. The elliptical shape of the column is now apparent at those wavenumbers, although it was completely blurred before the alignment. The location of the plume is related to the acquisition time of the ZPD frame since it was the reference frame used to align the other frames.

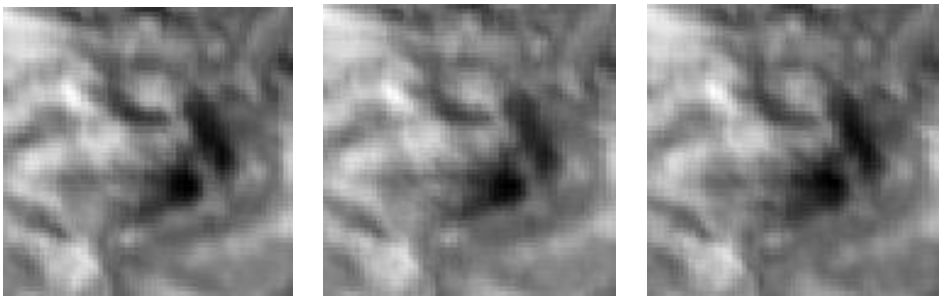

(a) Before alignment.

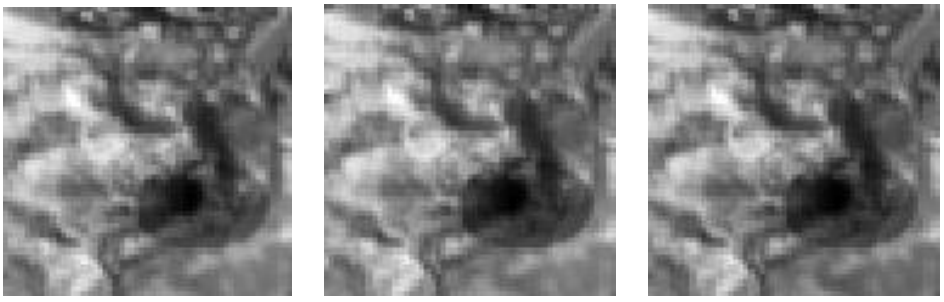

(b) After alignment.

Figure 3.9: Frames at wave numbers 6216, 6247, and 6366 cm-1 before (up), and after (down) alignment. In b), the elliptical shape of CO_2 is apparent.

3.3.2 Multiple Targets Scenarios

Data Cube Acquisition

A simulator is designed to obtain data cubes containing more than one moving target. The output of the simulator represents an array of detectors of an infrared camera. Each pixel in this camera will give a value related to the integration of the incident light from the IFTS. The dimension of this array can be varied. The integration in the detector is implemented by dividing each pixel to 100 sub-pixels then integrating their values. The hyper-spectral cube from the simulator has 1000 frames of 128 x128 pixels, with a $3.5cm^{-1}$ spectral resolution. The sampling rate or the minimum OPD step is set to twice the maximum wavenumber ($2000cm^{-1}$), the fill ratio for the sensors is set to 81%. The maximum off-axis angle is set to be 100mRad that is the maximum angle subtended by focal plane assembly (FPA) in Geosynchronous Imaging Fourier Transform Spectrometer (GIFTS) geometry [47]. In this section, we assume that we have two targets CO_2 and H_2O in the LWIR band at a temperature that is lower than the temperature of the background. The background is a blackbody at temperature 300K. We set the temperature of the targets at 250K, so they are in absorption mode. The targets and the proposed motion are shown in Figure 3.10.

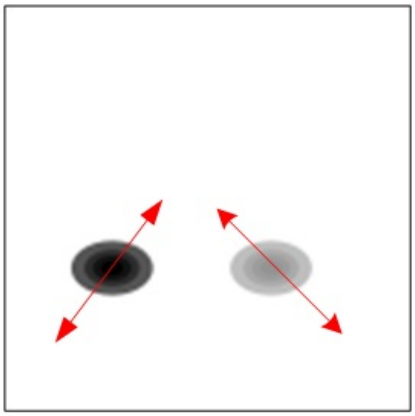

Figure 3.10: The simulated targets.

Registration using Motion Estimation

A carbon dioxide and water vapour plumes of gases are placed near the centre of the scene beside each other at the acquisition time of the ZPD frame. The CO_2 target moves diagonally at the lower right side, while the H_2O target moves diagonally at the lower left side with speed of 0.1pixel/frame.

We use the GDIM motion estimation between a main reference frame and two sub-references

frames and the other frames to estimate the motion vectors. We add two more sub-references frames because the motion of the target is greater than the maximum motion that can be computed using the algorithm. We estimate the motion vectors between these far frames and the sub-reference frames, and then add the resulted motion vectors to the motion vectors obtained between the sub-reference frames and the main reference frame. So, all the frames in the cube are motion estimated relative to the main reference frame. The motion vectors and the two parameters for the radiometric component are computed within a 9x9 window using the least square method. We use a three level pyramid (a hierarchically process from the top level to the bottom level) while computing the motion vectors for low computational complexity. The same simulation scenario is repeated with non moving targets to obtain the ground truth. The motion vectors obtained from the GDIM for both targets are shown in Figure 3.11 for carbon dioxide and in Figure 3.12 for the water vapour. We conclude from the motion vectors that both the targets are moving diagonally with the same speed in the scene.

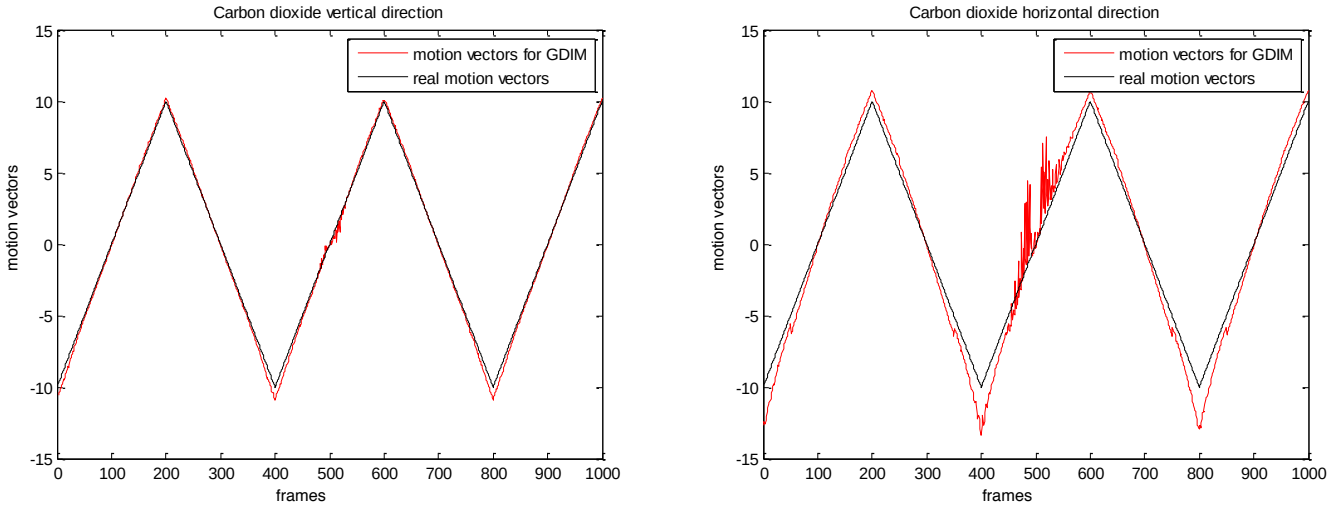

(a) Vertical

(b) Horizontal

Figure 3.11: Motion vectors for carbon dioxide.

Figure 3.13 shows the error in the motion vectors for both directions compared to the ground truth. The ground truth is the motion vectors used to move the targets in the simulator. The error for the CO_2 target is higher than the error in the H_2O target. This can be referred to the density of the CO_2 that is lower than the density of the H_2O. This results in a lower contrast between the CO_2 and the background that makes it harder to estimate the motion.

We choose two spatial locations in the scene, one in the CO_2 gas plume, and the other in the H_2O gas plume to construct the interferograms. Figure 3.14 shows the interferograms and spectra of the water vapour before and after correction. The red curve represents a pixel

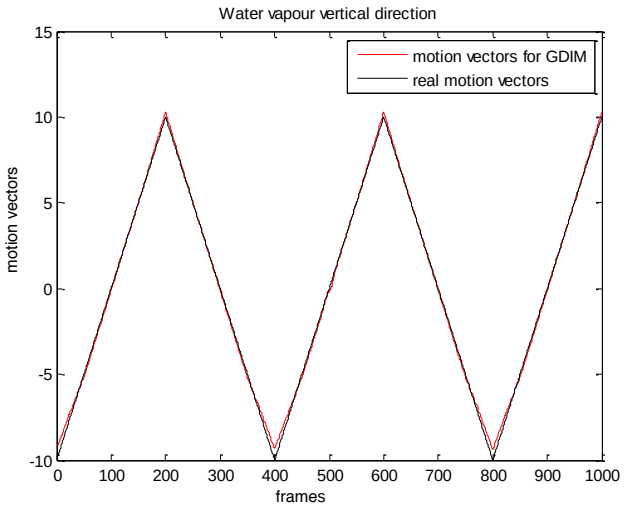

(a) Vertical

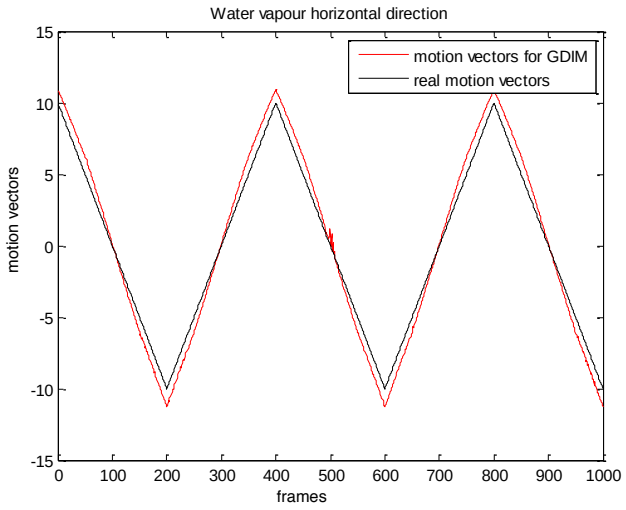

(b) Horizontal

Figure 3.12: Motion vectors for water vapor.

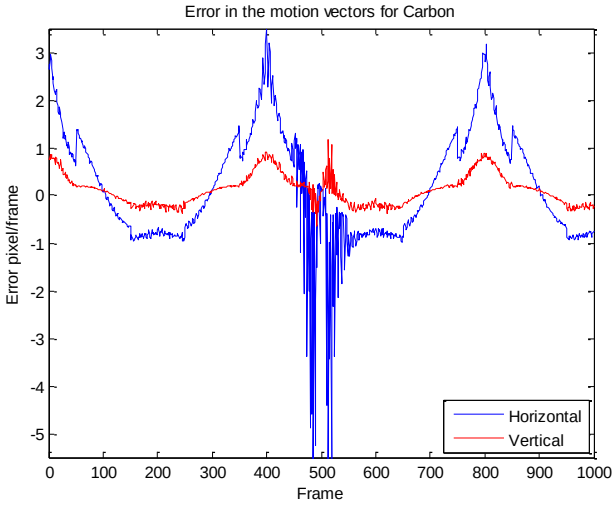

(a) Carbon dioxide

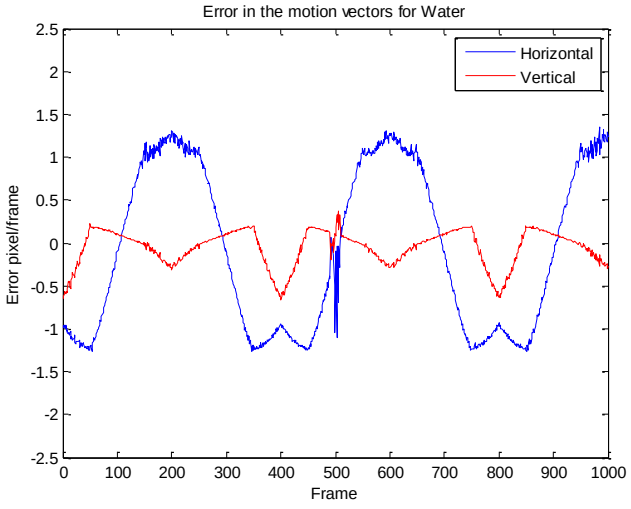

(b) Water vapor

Figure 3.13: Error in the motion vectors.

inside the water vapour before the motion correction. The oscillations of the interferograms indicates that the targets are moving repeatedly. We have used the motion vectors computed with the GDIM algorithm to align the spatial areas related to the water vapour in the frames. The motion corrected OPD for the examined pixel contains samples that belong to the water vapour only and is represented by the blue curve. The black curve is related to the reference stationary cube. From the figure of the interferogram, the motion corrected blue curve matches with the ground truth black curve. The spectrum curves show the benefit of using GDIM to align the frames of the IFTS. The out of band energy is low compared to the non corrected spectrum. Zooming on the absorption lines of the water vapor, shows to a high extent how the GDIM method managed to retrieve a high resolution spectrum matching with the ground truth. Similar results can be obtained from examining a pixel in the carbon dioxide target. From Figure 3.15, the blue curve related to the motion corrected interferograms match the ground truth black curve. From the figure of spectra, the motion correction algorithm manages to increase the resolution of the spectrum around the wavenumbers with high absorption (at $670cm^{-1}$). Looking at the motion corrected spectrum, we observe that it is a better match with the ground truth.

There exists a difference between the ground truth and the corrected spectrum for both targets. This is the effect of mixing off-axis distortions, which will be discussed in the next chapter.

3.4 Experimental Data

In this section we use the motion estimation techniques previously discussed on section 3.2 on experimental data generated from SpIOMM IFTS. We examine both the global motion between the SpIOMM and the scanned scene, and the scenario with two moving targets. We obtain a high resolution spectra for the used light source after registration.

3.4.1 Single Target Scenario

For a single target scenario we used a resolution target moving in the field of view of the SpIOMM. We obtain a high resolution spectral lines for the argon lamp. The results are published in [31].

Data Cube Acquisiton

For our experimental data, we placed a resolution target in the field of view of SpIOMM as shown in Figure 3.16. The target was lit by a filtered argon lamp. The target is moved diagonally across the field of view of the instrument using a step by step motor. SpIOMM, which is a "step-scan" interferometer, was triggered to acquire a frame between each displacement step. We installed two filters with cut-on frequency of 715nm and 1000nm on the resolution target. The captured data cube has 1340 frames of 1300 x1300 pixels, with a $50cm^{-1}$ spectral

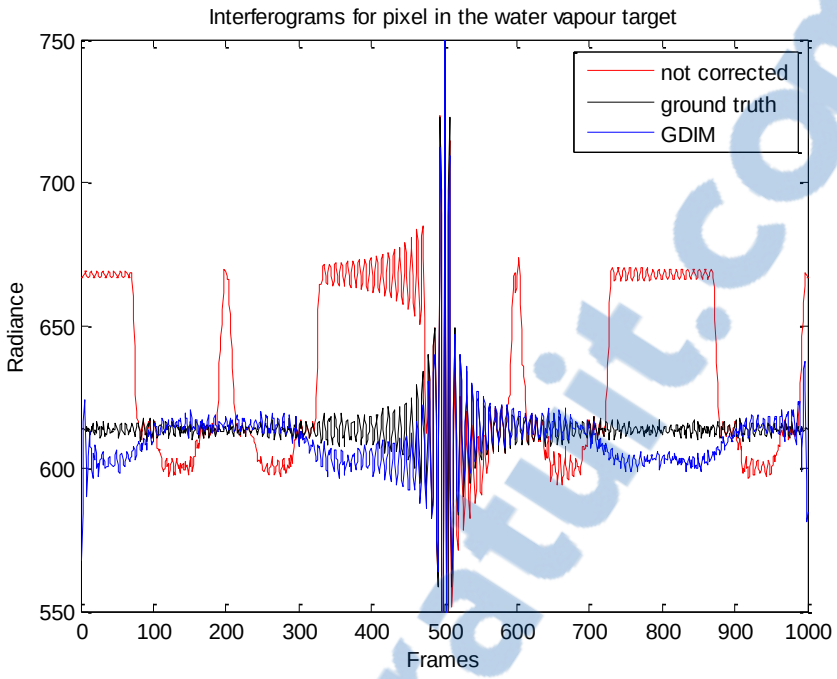

(a) Interferograms

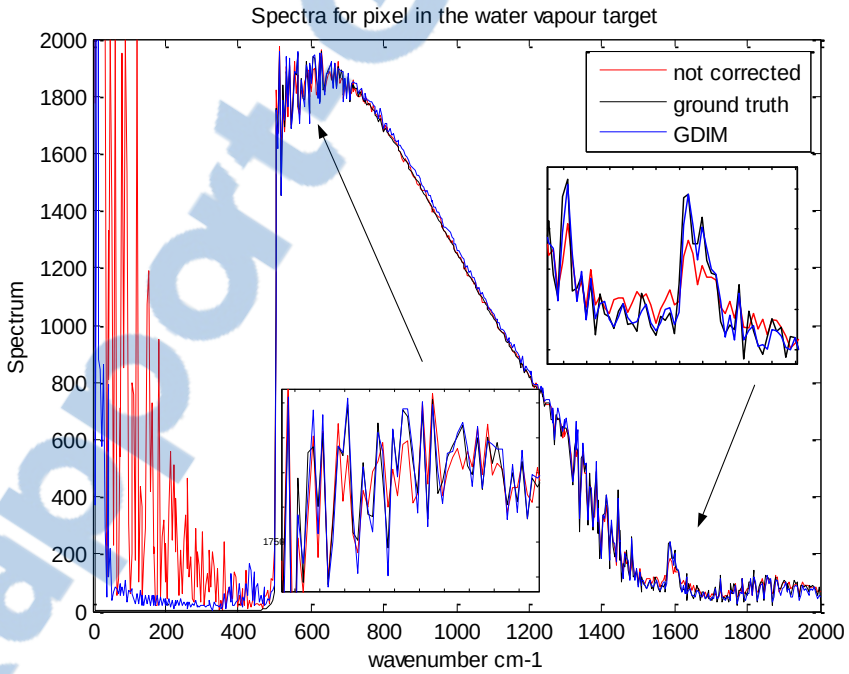

(b) Spectra

Figure 3.14: Interferograms and spectra for the water vapor before and after motion correction.

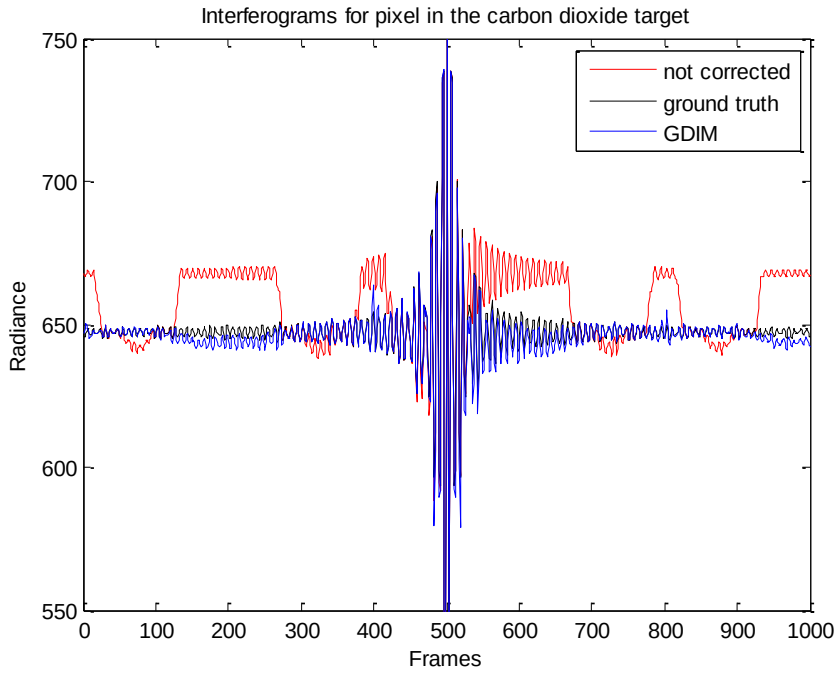

(a) Interferograms

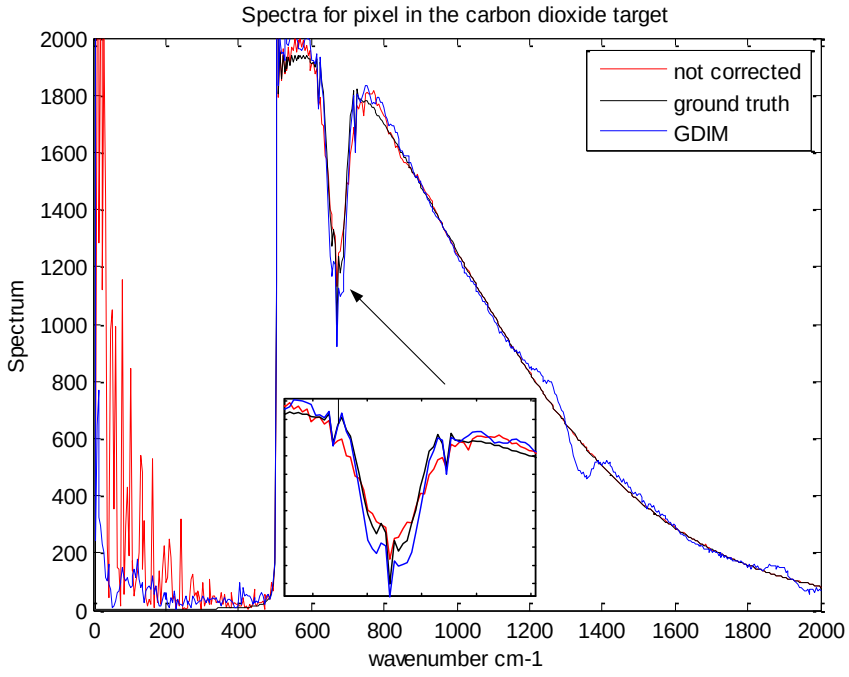

(b) Spectra

Figure 3.15: Interferograms and spectra for the carbon dioxide before and after motion correction.

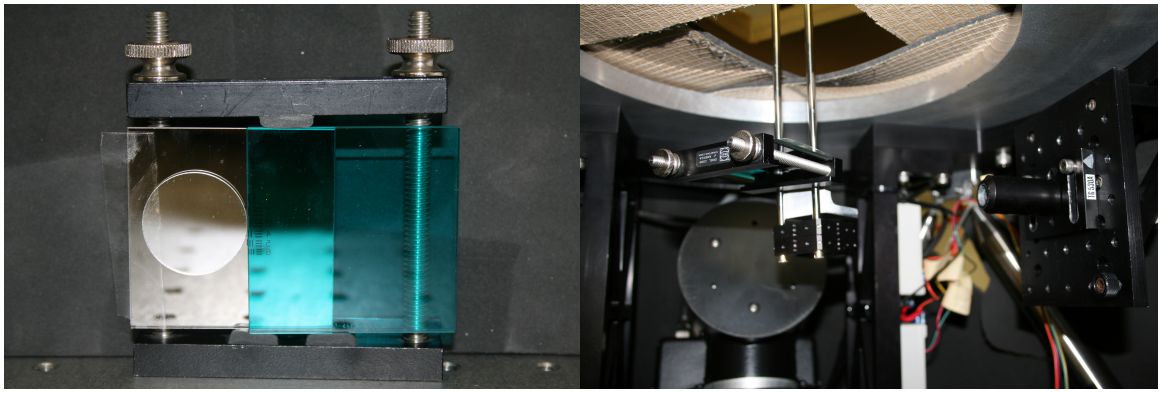

(a) Resolution target with filters

(b) Resolution target installed above the field of view of SpIOMM

Figure 3.16: Resolution target and filters.

resolution. We use pixel binning of 5x5 to have final frames of 260x260 pixels. After binning, it was shown that the target is moving in a diagonal direction at a rate of approximately 0.4pixel/frame. Figure 3.17 shows an output frame from SpIOMM including the resolution target, and the motion vectors for the target in both directions.

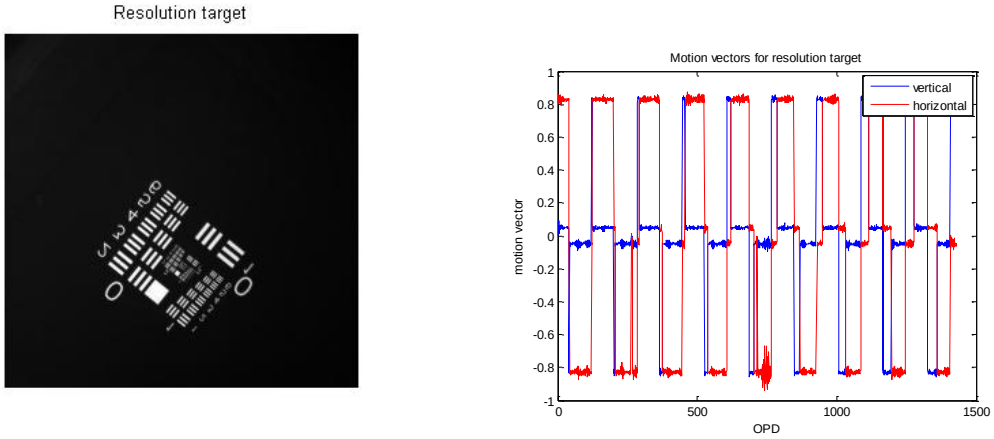

(a) Output frame

(b) Motion vectors

Figure 3.17: Resolution target and motion vectors.

Results

We tracked the interferogram samples for a pixel in the cut-on 715nm filter and computed its interferogram. We then compute the spectrum from the interferogram. We compare this spectrum with that coming from the same pixel but in a data cube where the target is stationary to show the effect of motion on the shape and resolution of the output spectrum.

The effect on the interferogram is shown in Figure 3.18 by the red curve related to the moving target, while the black curve is related to the stationary target. We observe that the red curve oscillates according to the motion of the target. The blue curve shows the interferogram after using the phase-base algorithm to correct for the motion. The blue curve matches with the ground truth black curve. Zooming on a part of the interferogram shows the efficiency of the motion estimation algorithm to place the interferogram samples related to the same spatial location on a single OPD axis.

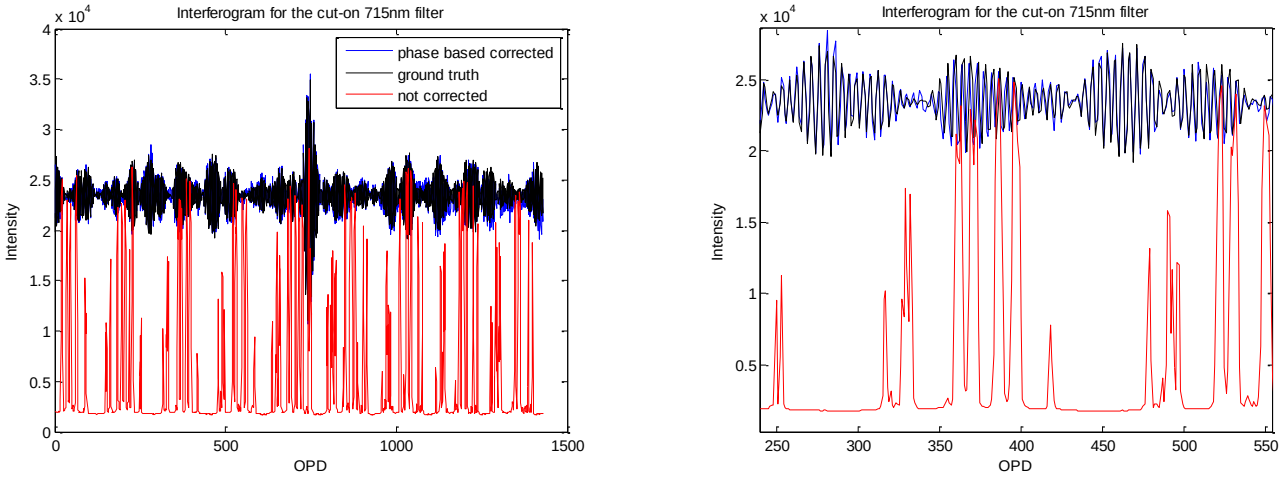

(a) Interferograms after motion correction

(b) Zoomed

Figure 3.18: Interferograms after motion correction for the red filter.

Figure 3.19 shows the spectra. We see that the motion corrected blue curve matches with the black ground truth. Zooming a part of the spectrum, we observe that we can retrieve the correct spectrum for the argon lamp. The difference between the ground truth and the motion corrected curve is related to the mixed off-axis distortion and will be discussed later. We tracked another pixel located in the opaque filter with cut-on 1000nm to verify the efficiency of the motion estimation algorithm. The opaque filter blocks the radiation of the argon lamp. After aligning the samples of the interferogram and computing the spectrum, the output spectrum has a nearly zero value at this band as shown in Figure 3.20

3.4.2 Multiple Targets Scenario

Data Cube Acquisition

We installed two targets in the field of view of SpIOMM. The first target is a green LED light with a spectral peak around $570nm$. The second target is a hole passing the wide spectral lines of the argon source. The two targets are moving in two diagonal non intersecting directions. The robots controlling the targets have a step motion of $0.1mm$ to give nearly 2

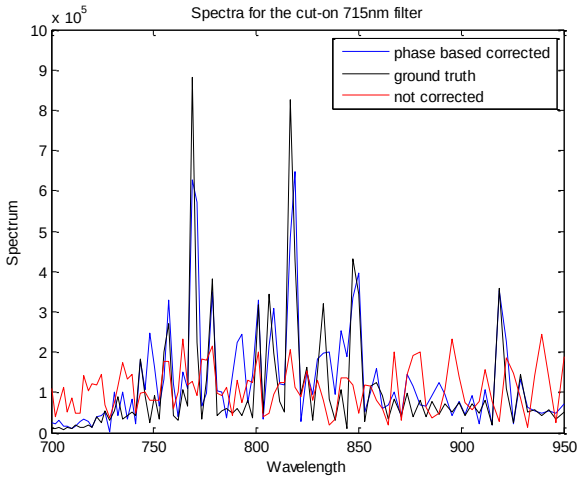

(a) Spectra for the red filter

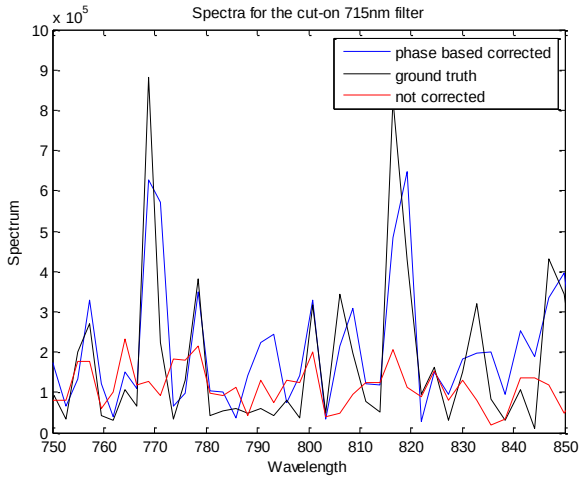

(b) Zoomed

Figure 3.19: Spectra after motion correction for the red filter.

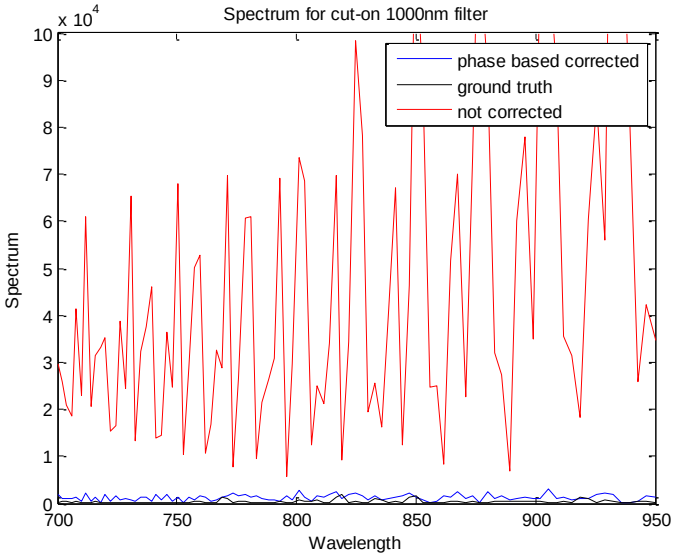

Figure 3.20: Spectra generated from the opaque filter.

pixels/frame motion, and the camera acquires the frames when the robots are stationary. We setup an experiment to give a cube of 1340 frames with 1300x1300 pixels, and 50 cm^{-1} spectral resolution. We use pixel binning of 5x5 to have final frames of 260x260 pixels. An output frame and the targets track are shown in Figure 3.21. The total track length for the targets is around 45 pixels after binning.

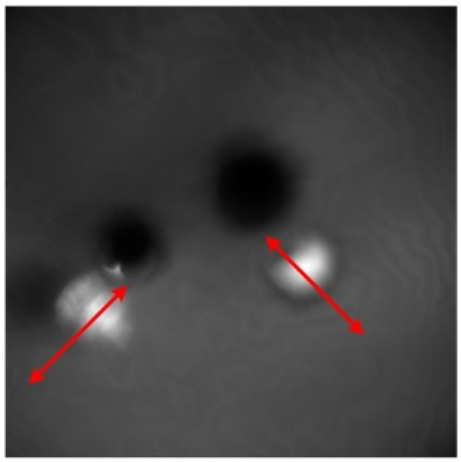

Figure 3.21: The simulated targets. (Left) is the is the green LED light and (right) is the hole.

The setup is isolated from the surrounding light. The light of the argon lamp lights the setup from the upper side to pass through a hole in a green plastic filter attached to one of the robots. The green LED is attached to the second robot and moves independently at a level higher than the green filter. The two robots are synchronized with the camera to acquire the frame shot when the robots are stationary. Time needed to scan one cube is around three hours. We scanned the same scenario with stationary targets to obtain a reference cube.

Results

We use the GDIM between a main reference frame and two sub-references frames and the other frames to estimate the motion vectors as discussed in the simulated cube with multiple targets. The computed motion vectors are shown in Figure 3.22. We conclude that the hole is moving repeatedly between the upper left and lower right directions, while the green LED is moving repeatedly between the upper right and lower left directions.

Figure 3.23 shows the interferograms and spectra of the LED target. The inteferograms before and after motion correction compared to the ground truth show the benefits of using GDIM to correct for the motion of the targets. The blue corrected curve matches the black ground truth curve. The peak of the LED spectrum is highly improved. A zoom on the transmission

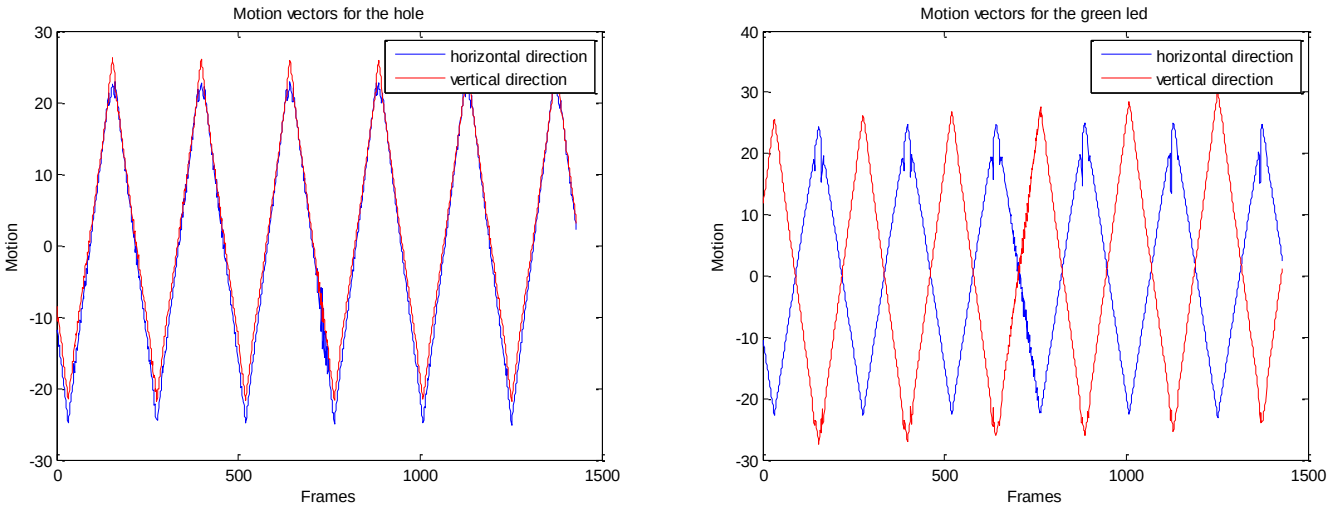

(a) Motion vectors for the hole

(b) Motion vectors for the green LED

Figure 3.22: Motion vectors for GDIM.

wavelength shows the increase in the resolution of the LED spectrum compared to the spectrum before motion correction represented by the red curve.

Similar results are obtained in the case of the hole target. Figure 3.24 shows the interferogram of the argon lamp and its spectrum before and after motion correction. Examining the interferograms proves the efficiency of the GDIM to place the samples of the moving target on the same OPD. The argon spectral lines after motion correction have higher resolution and match with the ground truth represented with the black curve. Two zoom window in the transmission wavelengths are shown. The minor differences between the motion corrected spectrum and the ground truth is related to the mixed off-axis distortion.

3.5 Conclusion

As a result of acquiring the hyper-spectral cube from a non stationary IFTS, the output spectra have degraded spectral resolution or are severely distorted. Two motion estimation techniques were combined to align the frames of the hyper-spectral cube in the case of global motion: MI technique for aligning the frames on a pixel-based reference, followed by phase-based for the sub-pixel level. This technique was tested on simulated and experimental IFTS data cube to give output spectra with reduced errors as well as with a recognized increase in the SNR. Moreover, aligning the cube allowed us to locate the target spatially and delimitating its shape.

To compensate for motion of more than one target, we modified the GDIM algorithm to take into account the particularity of the interferogram data around the zero path difference.

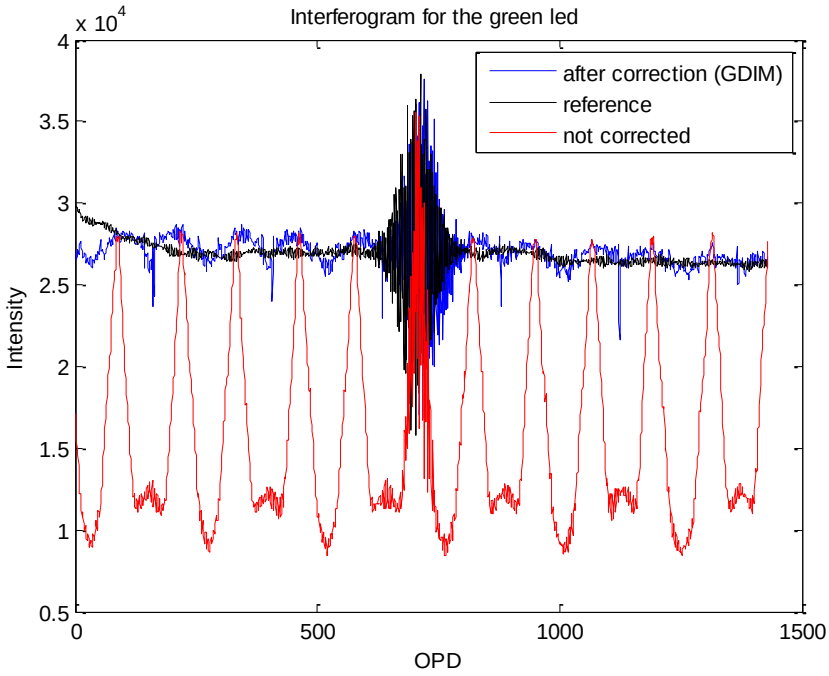

(a) Interferograms

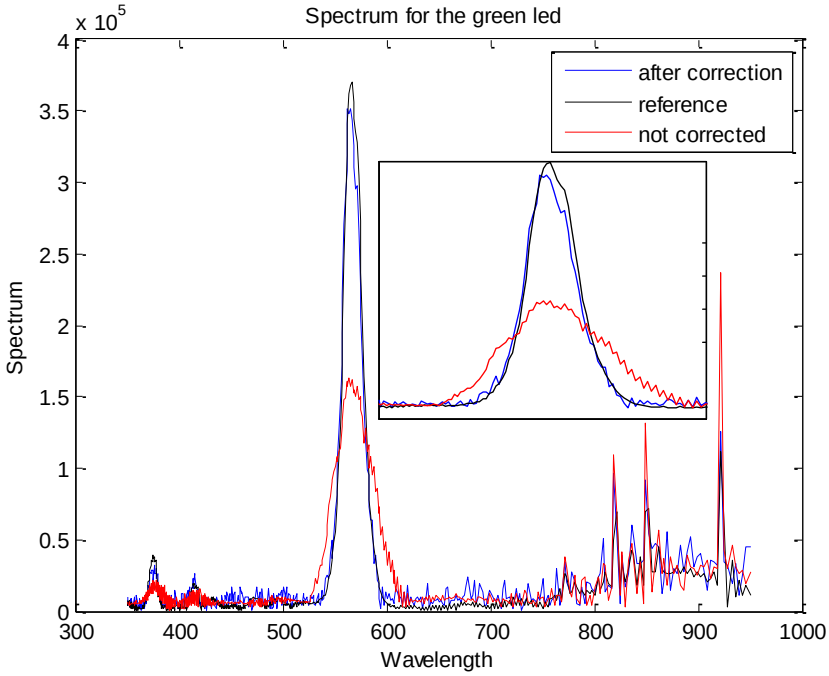

(b) Spectra

Figure 3.23: Interferograms and spectra for the green LED before and after motion correction.

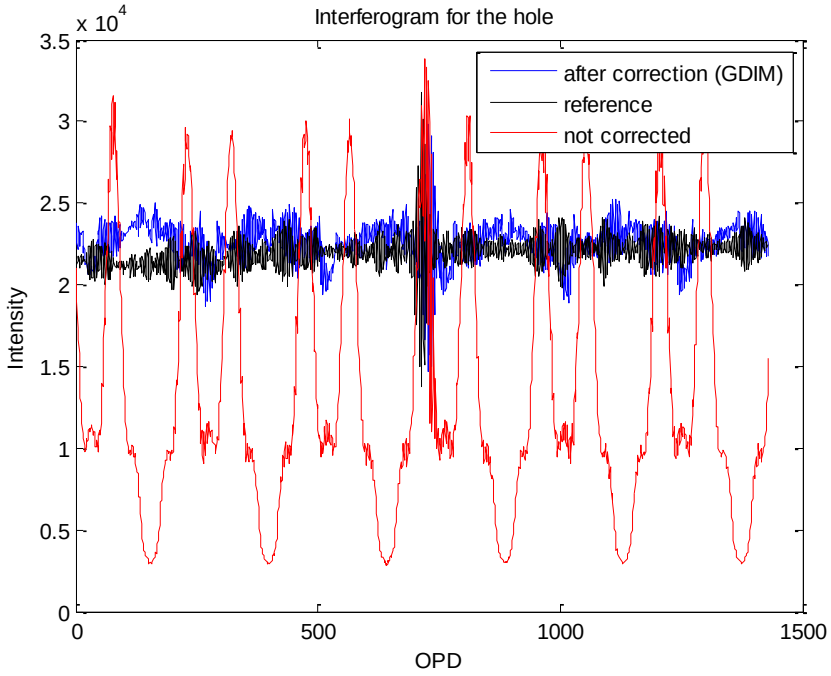

(a) Interferograms

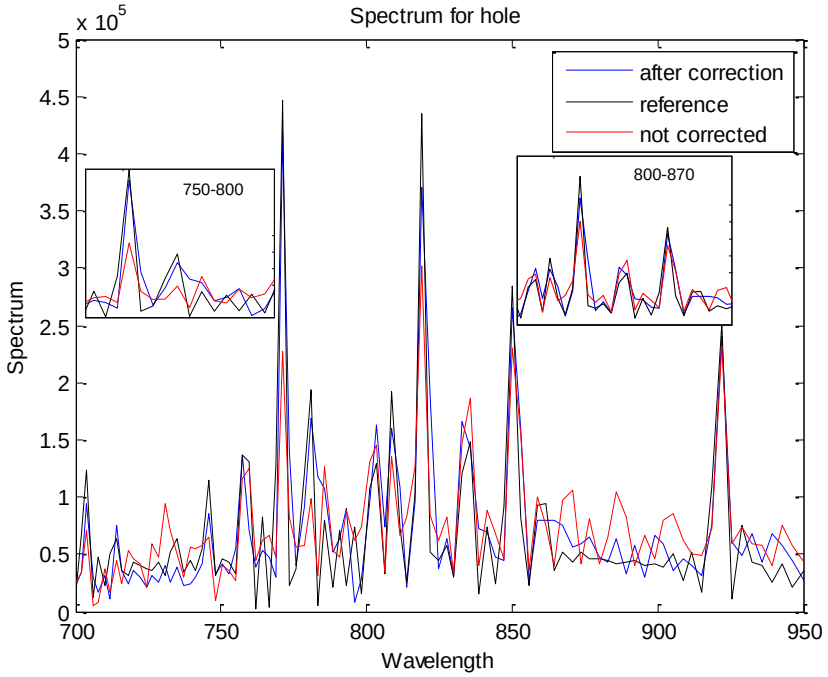

(b) Spectra

Figure 3.24: Interferograms and spectra for the hole before and after motion correction.

Again, we used simulated and experimental data to test our algorithms and evaluate their performance against a ground truth. This algorithm was used on data contains water vapor and Carbon dioxide to give output spectra with high resolution for both targets.

Chapter 4

Off-axis Correction

After registering the frames of the IFTS, an interferogram contains samples from different spatial locations that were subjected to different off-axis distortion. The spectrum obtained from the interferograms is not only scaled on the axis, but it is also distorted due to the mixed off-axis distortion values of the pixels. In the case of uniform off-axis distortion, a spectral scaling recovers the spectrum. When the off-axis distortion is not uniform or mixed, we need to correct for the distortion. In this chapter, we present an algorithm for correcting the mixed off-axis distortion. We align the samples on a given OPD axis according to the motion correction algorithm previously discussed. The proposed correction procedure resamples the interferograms for a given off-axis angle. We use simulated and experimental data cubes to demonstrate the results.

4.1 Illustration and Solving for Non-uniform Off-axis Distortion

Off-axis distortion shifts the signal toward the lower wavenumbers [10]. This shift depends on the geometry of the field of view and can be calculated by the value of the off-axis propagation angle of the rays in the interferometer. Working with a stationary IFTS, we can correct the off-axis distortion by rescaling the spectra with a proper adjusting of the wavenumber. Following [**?**] we can assume a relation between the corrected spectrum and the measured spectrum as follow:

$$S_c[j] = \sum_{k=-N}^{N} S_m[k] ILS_d[j,k] \tag{4.1}$$

where S_c is the corrected spectrum, S_m is the measured spectrum as measured by the instrument, and ILS_d is the discrete transfer matrix between the measured wavenumber grid k and the corrected wavenumber grid j, with $j, k \in [-N, N]$ for interferogram having (2N+1) points. Note that the interferograms can be assumed to be band-limited signals that can be sampled and interpolated with a sinc function to permit the exact reconstruction of the original signal

(when the sampling rate is higher than two times the Nyquist frequency). This helps us to discretize the equations. The ILS_d can be expressed as:

$$ILS_d[j,k] = \int_0^1 H(\alpha) D_N(\alpha k - j) d\alpha \tag{4.2}$$

where $H(\alpha)$ is the continuous ILS sampled by the Dirichlet kernel $D_N(\alpha k - j)$, and α is the cosine of the off-axis angle or the ratio between the measured and corrected wavenumber.

In the case of moving scene, the spectrum has contribution from many off-axis distortions related to the different spatial locations before motion correction. In this case, correcting the off-axis distortion in the interferogram domain is more convenient than correcting it in the spectral domain, since we can correct for each pixel independently as will be discussed.

When working in the interferogram domain, it is preferred to align the off-axis distorted data to the most off-axis pixel as shown in previous work [39, 14]. Shifting the data toward higher frequencies would imply a compression of the interferogram, resulting in loss of information at its extremities. Aligning in the interferogram can be done also by scaling the OPD axis with the ratio $\frac{cos(\theta_p)}{cos(\theta_q)}$, where θ_p is the off-axis angle related to the most off-axis pixel, and θ_q is an off-axis angle related to any other pixel in the spatial co-ordinate. After scaling, the grid points of the new samples do not coincide with the axis of the old ones. It is required to interpolate to determine the intensity values of non-grid points. Simulations done with bicubic interpolation proved to give low resolution results. Shifted Dirac function can be integrated in the interferogram to align it with the OPD of the most off-axis pixel. Following equations 4.1 and 4.2, the continuous ILS $H(\alpha)$ can be expressed by the shifted Dirac function in the case of imaging detectors with very small pixels. In this case, only the center of mass of the line shape of off-axis pixels is shifted toward lower frequencies, while it does not broaden significantly. We can then write

$$H(\alpha) = \delta(\alpha - \gamma) \tag{4.3}$$

where γ is the desired shift in the wavenumber. Substituting in equations 4.1 and 4.2 and taking the Fourier transform from j to m, where m is the corrected interferogram grid, the corrected interferogram in its final form as shown in [39] is :

$$i_c[m] = \frac{1}{2N+1} \sum_{k=-N}^{N} S_m[k] exp[i2\pi k m \beta] \tag{4.4}$$

where $\beta = \frac{\gamma}{2N+1}$

This technique proved to be faster and more precise than any other interpolation technique [39]. Figure 4.1 shows the advantage of interpolating using shifted Dirac function over the bicubic interpolation.

In the case of a moving scene, it is not possible to correct for the off-axis distortion using the scaling technique. The samples are collected from several spatial locations and each sample

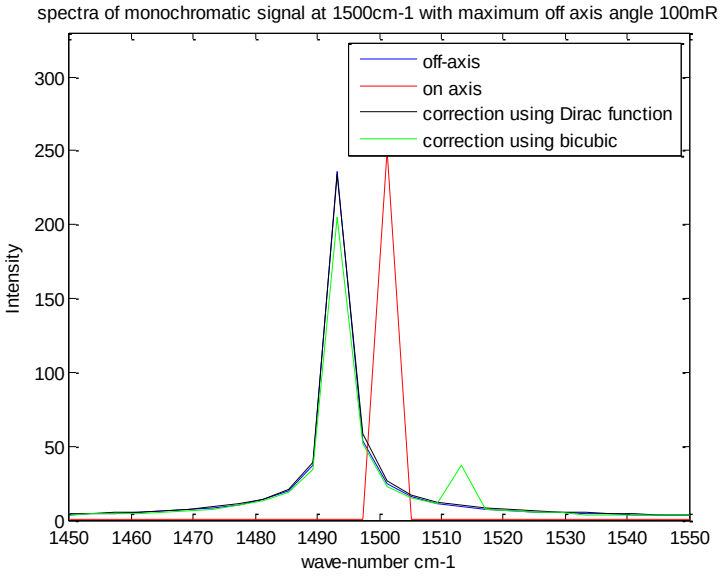

Figure 4.1: Monochromatic off-axis correction.

has its own off-axis distortion. Assuming that the motion is slow while scanning, we may still correct for the off-axis distortion. The diagram of Figure 4.2 shows the idea for mixed off-axis distortion correction. The resampling algorithm processes a motion compensated interferogram sample by sample, starting with the first sample. We calculate the cosine of the off-axis angle of the sample's OPD before motion correction (q_i) using the motion vectors $dx(i)$ and $dy(i)$ that are generated when aligning the frame i. Using the ratio p/q_i where p is the cosine of the off-axis angle for the motion corrected OPD spatial location, we shift the OPD that includes pixel i before motion correction towards the motion corrected OPD. Considering slow motion between the frames, the off-axis distortion differs slowly or is constant between consecutive samples for the tested interferogram. When interpolating for the new sample value using the surrounding samples, the kernel of interpolation extends to samples with nearby or constant off-axis angle. So, the error is limited while stretching or compressing the OPD.

4.2 Off-axis Correction for Simulated Data

In this section we apply the algorithm previously discussed to correct for the off-axis distortion for simulated data. To generate the off-axis angles to be used in the off-axis correction algorithm, we start by simulating the distortion map for the simulated data cube containing multiple targets, as previously discussed. We define σ_0 as the wavenumber of the central pixel with the minimum off-axis distortion, and σ is the apparent wavenumber for any other pixel. They are related by the cosine of the off-axis angle θ as $\frac{\sigma}{\sigma_0} = cos(\theta)$. From Figure 4.3,

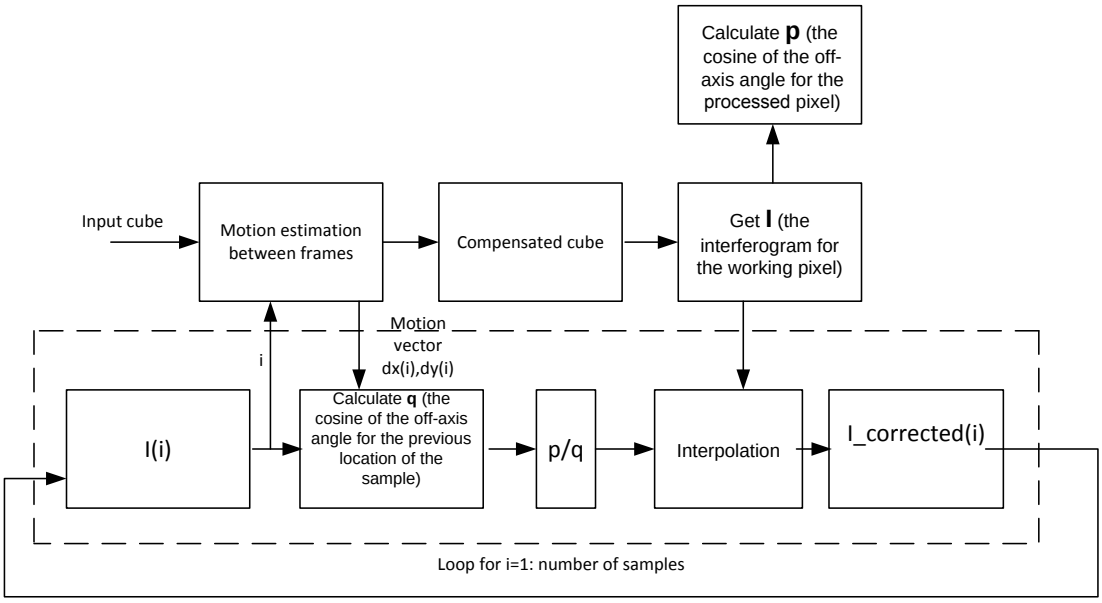

Figure 4.2: Off-axis correction algorithm.

the central pixel has no off-axis distortion with wavenumber σ_0 , while this distortion is at its maximum at the corner pixels with wavenumber σ_{min}. We may relate any wavenumber corresponding to a pixel (x, y) to the minimum wavenumber corresponding to the corner pixel by $\sigma_{min} = b(x, y) \times \sigma(x, y)$, where $b(x, y)$ is a scaling factor between pixel (x, y) and the corner pixel, and $\sigma(x, y)$ is the associated wavenumber to this pixel. For simulating the map, a monochromatic signal at 1500 cm^{-1}, with spectral resolution of $3.5cm^{-1}$, and cube dimension of 128x128 with 1000 frames are used. Maximum off-axis distortion angle is 100mrad.

There exist a difference between the ground truth and the motion corrected spectrum for the simulated data cube (section 3.4). This is the effect of mixing interferogram values with different off-axis distortion. Each motion corrected sample was subjected to a different off-axis distortion according to its spatial location. We use the off-axis correction algorithm previously discussed to correct for this distortion. The benefit of the correction is clearly apparent with the water vapor target. In Figure 4.4a we can see that the off-axis distortion changes the shape of the spectral lines. After correction, the spectral lines are a better match to the ground truth. For comparison accuracy, the off-axis angle used to simulate the ground truth has the same value of the off-axis angle for the motion corrected OPD. The mean square error between the ground truth spectrum and the corrected spectrum using the mixed off-axis correction algorithm is 80. We choose the band $1300 - 1480cm^{-1}$ where the water vapour is in absorption mode to compute the MSE value.

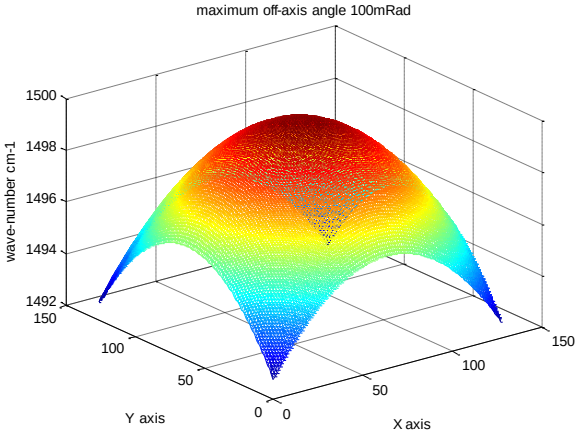

Figure 4.3: Simulated wave-number map.

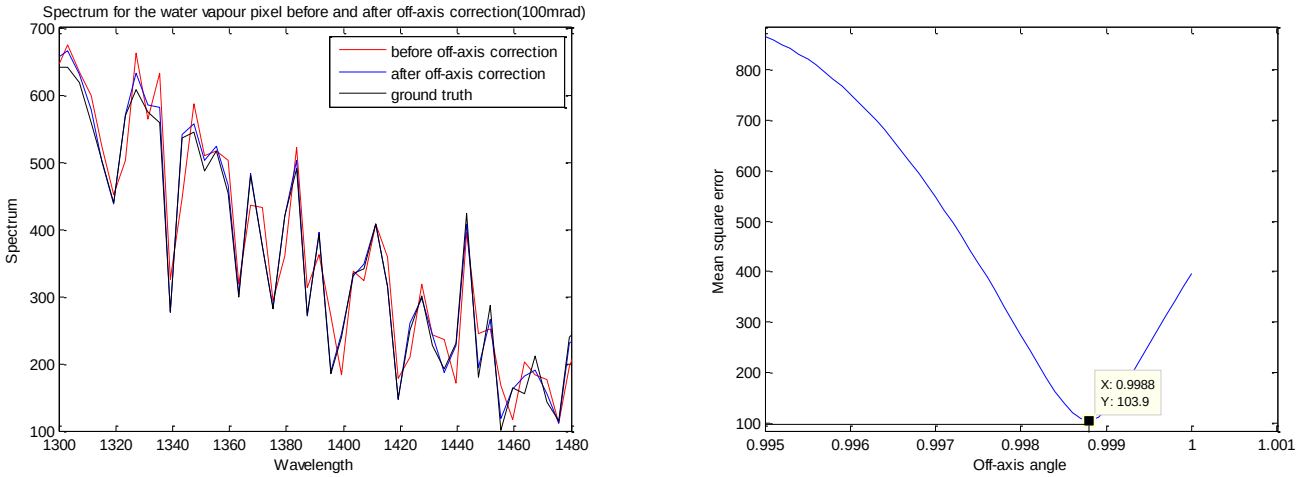

(a) 1300-1480cm-1

(b) Error generated from spectral shift off-axis correction

Figure 4.4: Spectrum of water vapour after using non-uniform off-axis correction and the errors generated from the spectral shift off-axis correction.

Next, we compare this value with the least error that can be obtained for off-axis correction using the spectral shift method. To do so, we calculate the least mean square error (LMSE) between the spectral shifted spectra for all possible off-axis angles and the ground truth spectrum. Figure 4.4b shows the error curve as a function of the cosine of the off-axis angle. LMSE is 103.9 for cosθ=0.9988. This gives an advantage for the mixing off-axis correction algorithm over the spectral shift method of about 20%. Figure 4.5a shows the spectrum computed with the least mean square error spectral shift(cosθ=0.9988), the mixing off-axis corrected spectrum, and the ground truth. From that figure, we see the advantage of using the mixing off-axis correction algorithm compared to the spectral shift off-axis correction method. Figure 4.5b shows the difference between the spectra generated from both methods and the ground truth. The error is lower in the case of mixing off-axis correction compared to the spectral shift technique. Note that with experimental data, it is not possible to find the off-axis angle that gives the LMSE for the spectral shift off-axis correction. We introduced the spectral shift method as a way to benchmark our algorithm.

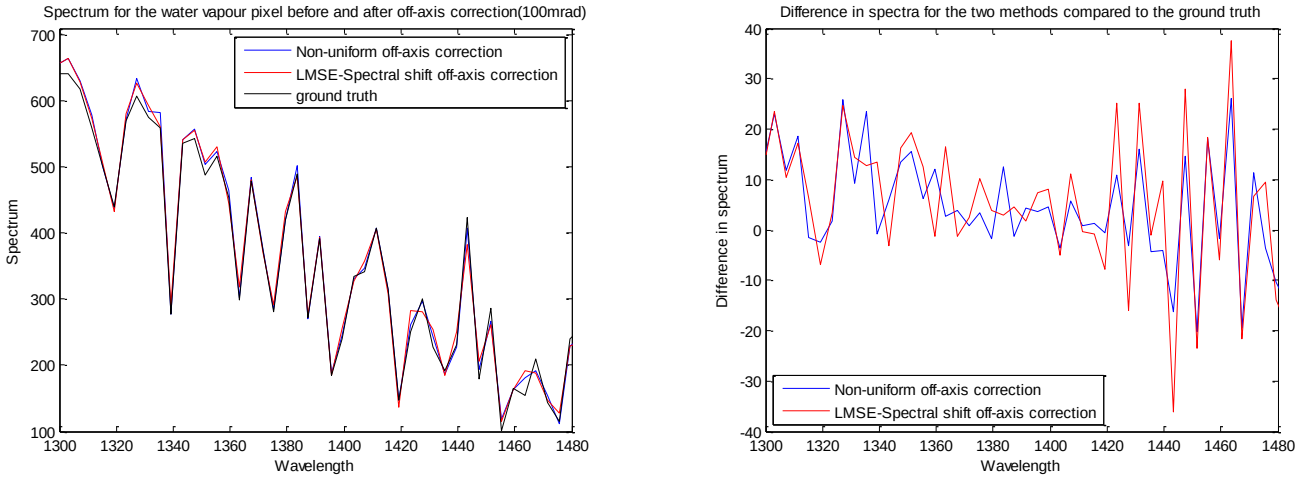

(a) Spectra

(b) Difference from ground truth

Figure 4.5: Spectra from non-uniform off-axis correction and LMSE-spectral shift off-axis correction.

4.3 Off-axis Correction for Experimental Data

In this section, the off-axis correction algorithm previously discussed in section 4.1 is applied on experimental data generated from SpIOMM. Using the SpIOMM experimental data, the off-axis distortion is calculated using a data cube captured with an integrating sphere, in which a single mode laser is injected, placed in the field of view of SpIOMM. The interferograms of this data cube are Fourier transformed to obtain a cube of the monochromatic laser spectra.

Zero padding and interpolation are used to increase the accuracy of the estimated frequency peak at each pixel. For this work, we have zero padded the frequency grid up to 2^{15} samples on each axis. Figure 4.6 shows the off-axis map we have computed before and after increasing the resolution. From the figure we can notice that the minimum off-axis distortion is not located at the centre because the highest frequency is at the edge. This is a characteristic of SpIOMM, which was designed to work with two output ports where the on-axis pixel is between them.

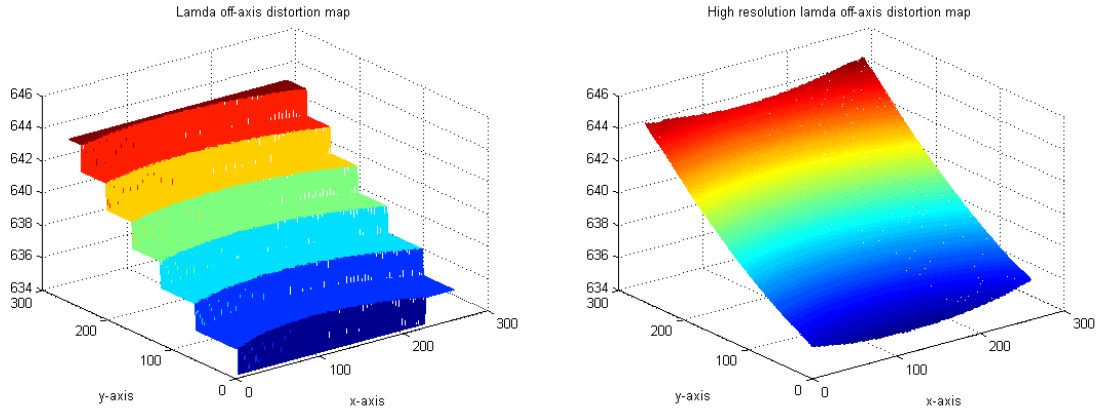

(a) Low resolution map

(b) High resolution map

Figure 4.6: Off-axis map before and after increasing resolution.

4.3.1 Results for a Single Target

The frames in SpIOMM data cubes have high off-axis angles as shown with the calculated off-axis map. In section 3.4.1, after aligning the frames in the data cube using the phase-based method, the samples placed on the motion corrected OPD as shown in Figure 3.19 have errors from mixed off-axis distortion. We apply the off-axis correction algorithm for each sample on the motion corrected OPD using the surrounding samples for interpolation purpose. We assume that the surrounding samples are subject to the same or approximately the same off-axis angle distortion due to the target slow motion. Figure 4.7 shows the advantage of applying the off-axis correction algorithm. It improves the resolution of the output spectrum generated after motion correction in the experiment of moving resolution target. The output spectrum after off-axis correction coincides with the spectrum of the non-moving target[31].

4.3.2 Results for Multiple Targets

We look at the spectrum of pixels in the target hole (section 3.4.2) because it has wide spectral lines. The argon spectral lines generated in Figure 3.24 show a high improvement after off-axis

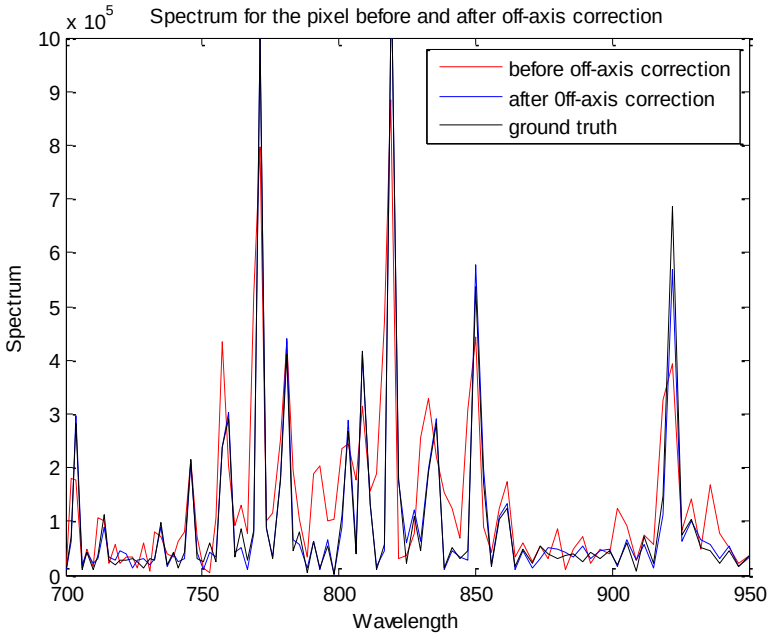

(a) Spectra after off-axis correction

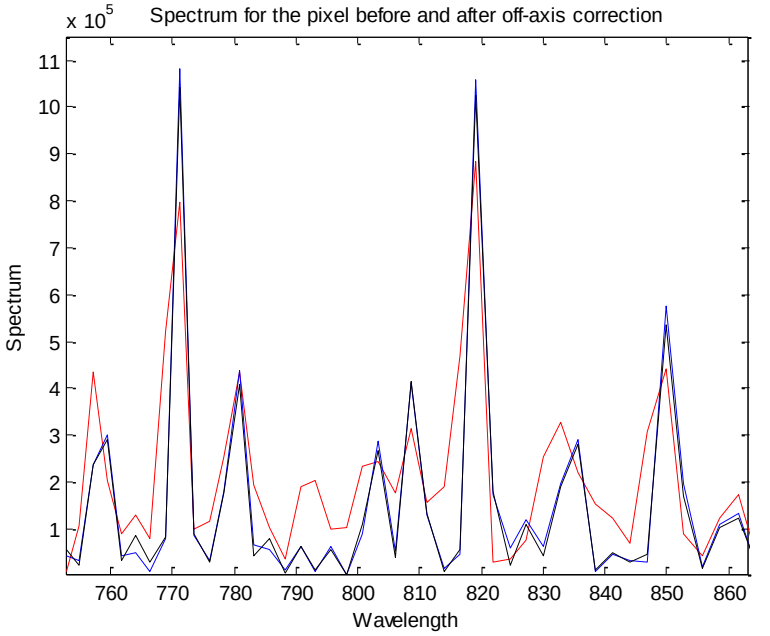

(b) Zoomed

Figure 4.7: Spectra after off-axis correction.

correction as shown in Figure 4.8. The 700-900nm band and a zoom on the 750-850nm are given to show the improvement in the resolution before and after off-axis correction.

4.4 Conclusion

After aligning the samples from different spatial locations on the same OPD, a non uniform off-axis distortion problem appears. Each aligned sample on the OPD has a different off-axis distortion angle related to its previous location.

We developed an algorithm to resample the interferogram obtained by motion compensation. This algorithm assumes that the motion is slow enough so that the off-axis distortion parameters vary slowly with the interferogram samples. We tested our off-axis correction algorithm with our motion estimation algorithms on simulated and experimental data, and obtained a spectrum with resolution similar to the ground truth of a non moving target.

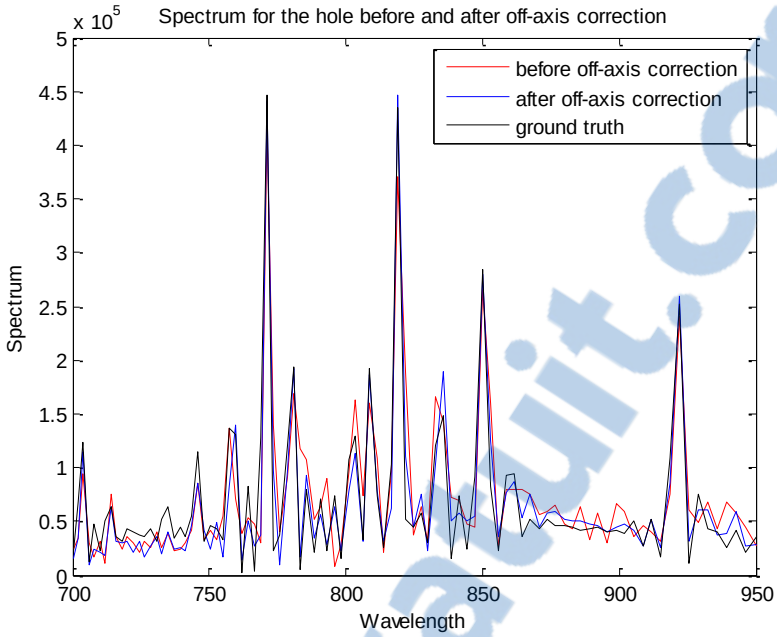

(a) 700-950nm

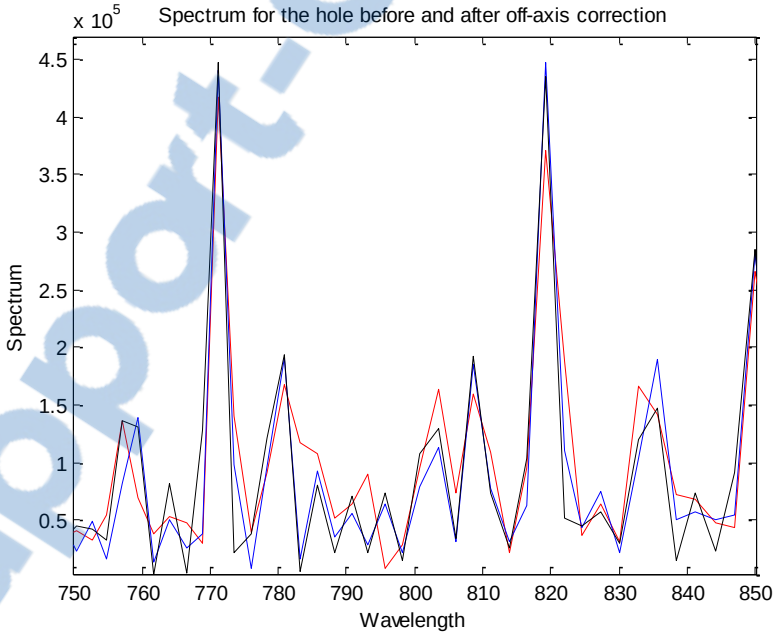

(b) 750-850nm

Figure 4.8: Spectra of the hole before and after off-axis correction.

Chapter 5

Calibrating an IFTS scanning moving scenes

5.1 Problem description

It is a standard procedure for imaging FTS to calibrate the spectral gain of its focal plane array, which varies from pixel to pixel, or to perform a radiometric calibration (gain and offset) of the spectrometer [10]. This work addresses the problem of gain calibration for data cubes with moving scenes/targets. We presented in [29, 31] the problem of moving scenes and targets in the field of view of a scanning imaging FTS along with new algorithms for the registration and re-alignment of frames of the data cubes. This process is required to recover accurate spectra of the moving target and background. We propose now further improvement of those algorithms by combining them with the radiometric calibration.

While the offset is readily removed based on the linearity property of Fourier transform, a proper integration of the spectral calibration to the frame registration is needed for the gain. We observed as well that in some cases the boundaries between the targets and background may lack contrast in raw data cubes as a result of the gain and offset of the instrument, reducing the performance of motion estimation techniques required for frame registration.

Starting from the spectrometer equation 2.2, and assuming that we have samples from a target and background measured alternately by the same pixel, where the samples of the background starts at $x = x_0$ and ends at $x = x_1$, and the samples of the target starts at $x = x_1$ and ends at $x = x_{end}$, equation 2.2 takes the form of:

$$I_t(x) = \begin{cases} 2\int_{\sigma 1}^{\sigma 2} A_\alpha(\sigma)d\sigma + 2\int_{\sigma 1}^{\sigma 2} A_\alpha(\sigma)cos(2\pi\sigma x)d\sigma & \text{for } x_0 \leq x < x_1 \\ 2\int_{\sigma 1}^{\sigma 2} A_\beta(\sigma)d\sigma + 2\int_{\sigma 1}^{\sigma 2} A_\beta(\sigma)cos(2\pi\sigma x)d\sigma & \text{for } x_1 \leq x < x_{end} \end{cases}$$

where $I_t(x)$ is the intensity at a given OPD x, $\sigma 1$ and $\sigma 2$ are the start and end wavenumber of the spectral band where the response of the sensor is not null (sensor operating band),

$A_\alpha(\sigma)$ is the spectrum of the background in the sensor operating band, and $A_\beta(\sigma)$ is the spectrum of the target in the same band. The first term in these two equations is the DC level of $I_t(x)$. We have two different values, one for the background and one for the target. We need to keep these DC levels for the step of frame registration because they represent the contrast between the background and the target. For calibrating a raw spectrum, we use the calibration equation depending on instrument gain and offset as shown in equation 2.12

$C_\sigma = R_\sigma(L_\sigma + L_{\sigma 0})$

Moreover, recalling the equations of 2.13 and 2.14, the gain and offset are generated from physical blackbodies C_h and C_c with interferogram samples linked to pixel location. So, we cannot perform motion registration before data calibration. To calibrate a raw spectrum, we will use the instrument gain and offset shown in the previous equation. The spectral calibration process is performed within the sensor operating band while forcing the out-of-band to zero. This last step would remove any unmodulated component from the interferograms (i.e, the DC levels of the interferograms). This makes frame registration and motion compensation impossible to do as a result of losing the contrast between the targets and the background.

We can summarize the problem as:

1. We need to calibrate interferograms related to moving targets where the samples of the inteferograms are not always related to the same sub area.

2. Data before calibration may lack the contrast that is needed by the motion estimation techniques.

3. We cannot subtract the DC levels of the unmodulated lights because they are important for the step of motion estimation.

4. Calibration data is linked to pixel location.

5. Frame registration mixes pixel locations before we can apply the calibration.

5.2 Calibrating a Stationary Simulated Cube

In this section we calibrate a simulated raw fixed data cube to have a deeper understanding for the challenge of calibration. We keep the DC levels and use them in the calibration process. After verifying the results, this will help us to introduce a calibration algorithm in the case of non-stationary cubes.

We start by simulating a raw data cube that contains two fix targets of water vapour and carbon dioxide as shown in section 2.2.1. To generate the raw data, we use the calibration

parameters (gain and offset) with the input spectrum to the simulator as follows

$$\text{raw spectrum}(i,j) = \text{simulated spectrum}(i,j) \times \text{Gain}(i,j) + \text{Offset}(i,j) \tag{5.1}$$

This equation which "uncalibrates" the spectrum is processed for each spatial location (i,j) in the simulated cube. For simplicity we have applied the same gain and offset for all the sub-pixels included in the pixel's location.

We scanned hot and cold blackbodies using an ABB IFTS. Using the theoretical cold and hot blackbodies spectra, we can evaluate the gain and offset at each spatial location. The number of points in the spectra of ABB cube is 8000 spectral points, whereas the number of spectral points corresponding to the sensor operating band is only 150 points. We upsampled the 150 spectral points for the sensor operating band to match the number of spectral points for the input simulated spectrum to the simulator, i.e. 3000 points. We also upsampled the frames of the cold and hot BB of 64x64 pixels spatially, to match with the simulator's frame size of 128x128 pixels. Figures 5.1, and 5.2 show the gain and offset function for the ABB IFTS and their up sampled versions to the size of the simulated spectrum. Note that the gain is going to infinity because the theoretical BB curves used to generate the gain go to zero when increasing the frequency.

We use the same calibration parameters used at the un-calibration process to calibrate the output spectrum from the simulator. The output spectrum is 1000 points. The working window is 375 spectral points. We downsampled the calibration parameters from the ABB IFTS to fit in this working window and calibrate the output spectrum. Figure 5.3 shows the gain and offset values that are used to calibrate the output spectrum. These values are those of a pixel in the carbon dioxide target. The calibration process follows the normal calibration procedure for IFTS data except for the DC levels for the unmodulated lights. When calibrating stationary IFTS data cubes, we subtract this DC level in the interferogram before calibration. In non-stationary IFTS data cubes, the unmodulated light levels (DC levels) are important to distinguish the background from the targets in the interferograms. To keep this contrast, we need to preserve the DC levels of the interferograms.

To describe the challenge we face with the unmodulated light component of the interferograms that is used in the calibration of non-stationary IFTS cubes, we start from the raw data step. Assume $A(\sigma)$ is an input calibrated spectrum in the sensor operating band, where σ is the wave-number, $B(\sigma)$ is the raw spectrum, $G(\sigma)$, $O(\sigma)$ are the gain and offset used in the conversion between the calibrated and raw spectra. The relation between the calibrated and raw spectra as shown in section 2.1.5 is

$$B(\sigma) = A(\sigma) \times G(\sigma) + O(\sigma) \tag{5.2}$$

We write

$$I^{'}(x) = I_0^{'}(x) + I_1^{'}(x) \tag{5.3}$$

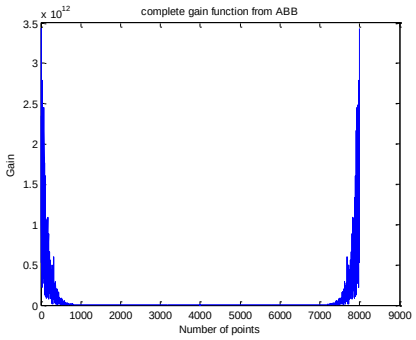

(a) Full band gain

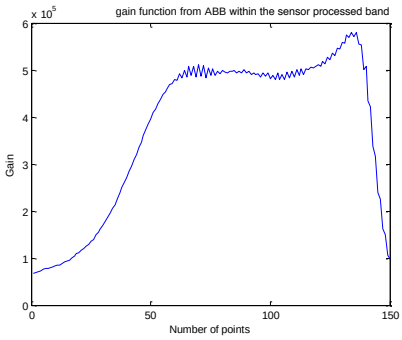

(b) Gain in the sensor operating band

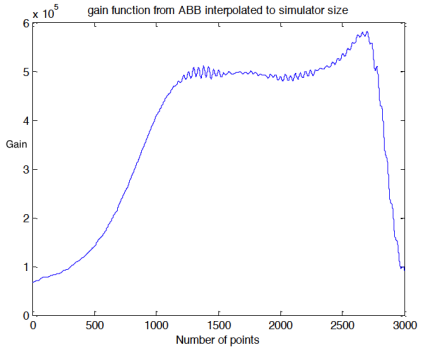

(c) Gain in the sensor operating band after upsampling.

Figure 5.1: ABB IFTS gain function used for un-calibrating the simulator.

where $I^{'}(x)$ is the interferogram with non zero DC level for the raw spectrum, $I_0^{'}(x)$ is the DC level, and $I_1^{'}(x)$ is the modulated part of the interferogram. We also write

$$I(x) = I_0(x) + I_1(x) \tag{5.4}$$

where $I(x)$ is the interferogram with DC level for the calibrated spectrum, $I_0(x)$ is the DC level, and $I_1(x)$ is the modulated part of the interferogram.

In the frequency domain, we can define $A(\sigma)$, $B(\sigma)$ and $C(\sigma)$ as respectively the Fourier transforms (FT) of $I_1(x)$, $I_1^{'}(x)$, and $I^{'}(x)$. From the previous equations, we get

$$\begin{aligned} FT(I^{'}(x)) &= FT(I_0^{'}(x) + I_1^{'}(x)) \\ C(\sigma) &= FT(I_0^{'}(x)) + FT(I_1^{'}(x)) \\ C(\sigma) &= B_0(0) + B(\sigma)\ . \end{aligned} \tag{5.5}$$

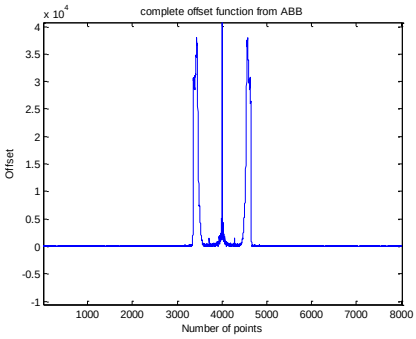

(a) Full band offset

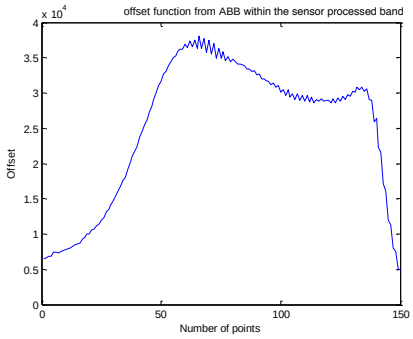

(b) Offset in the sensor operating band

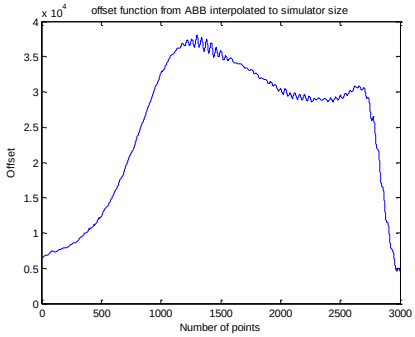

(c) Offset in the sensor operating band after upsampling.

Figure 5.2: ABB IFTS offset function used for un-calibrating the simulator.

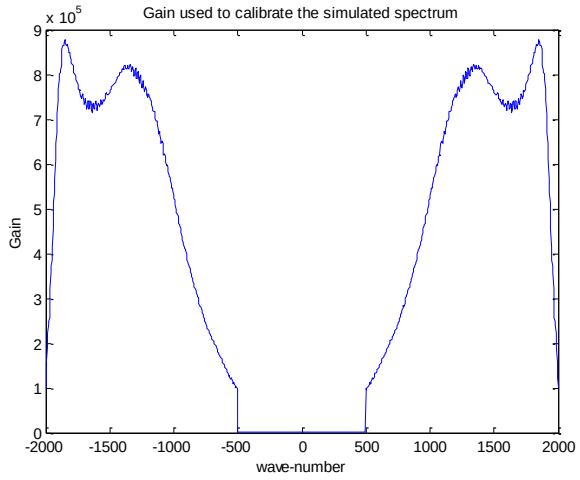

(a) Gain

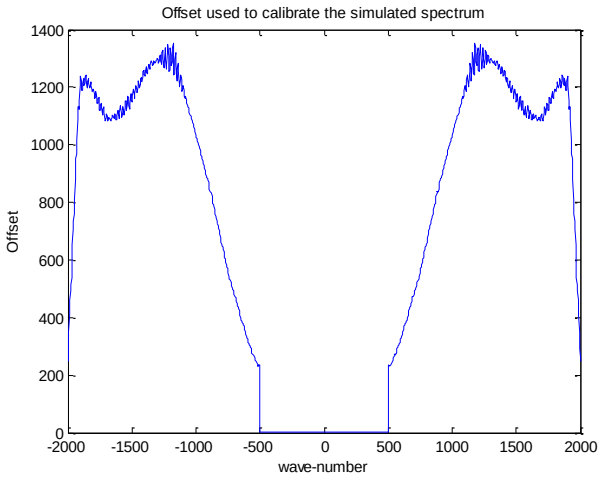

(b) Offset

Figure 5.3: Gain and offset functions used to calibrate the spectrum.

If we calibrate $C(\sigma)$, we get

$$\begin{aligned}\frac{C(\sigma)-O(\sigma)}{G(\sigma)} &= \frac{B_0(0)+B(\sigma)-O(\sigma)}{G(\sigma)} \\ &= \frac{B_0(0)}{G(\sigma)} + \frac{B(\sigma)-O(\sigma)}{G(\sigma)} \\ &= \frac{B_0(0)}{G(0)} + A(\sigma)\end{aligned} \tag{5.6}$$

Since the gain function is defined only for the sensor operating band, we cannot know its value at the zero frequency.

For the stationary cubes, we can revert to the main interferogram equation

$$\begin{aligned}I(x) &= 2\int_{\sigma 1}^{\sigma 2} A(\sigma)[1+cos(2\pi\sigma x)]d\sigma \\ &= 2\int_{\sigma 1}^{\sigma 2} A(\sigma)d\sigma + 2\int_{\sigma 1}^{\sigma 2} A(\sigma)cos(2\pi\sigma x)d\sigma \\ &= I_0(x) + I_1(x)\end{aligned} \tag{5.7}$$

So, if we integrate the calibrated spectrum (Eq. 5.6) for the sensor operating band, we get the DC level (i.e, $I_o(x)$) of the unmodulated light. This only true when the scanned scene is stationary. In the case of non-stationary scene, the interferogram of a pixel may have samples from both a target and the background, and integrating the calibrated spectrum will only give a weighted sum of the different DC levels.

Following the equations, the steps to calibrate a stationary cube while preserving the DC levels are as follow:

1. Calibrate using the offset and the gain values according to the calibration equation.
2. Force the out-of-band spectrum to zero value.
3. Integrate the calibrated spectrum under the sensor operating band and place this value at the zero frequency.
4. Compute the inverse FT of the whole spectrum to get the the calibrated interferogram with the correct DC levels.

Results for Calibrating a Stationary Simulated Cube

To verify our "un-calibration and calibration process", we compare the finally calibrated spectrum with a spectrum generated from a reference simulated cube without any calibration process. From the carbon dioxide target shown in Figure 5.4, we can recognize that the calibrated interferogram and spectrum are near to the references. The calibration parameters

used to generate the raw spectrum and calibrate the output spectrum from the simulator are interpolated to fit with the number of points for each spectrum. This can explain why the calibrated spectrum does not perfectly match the reference one. After calibrating each inter-

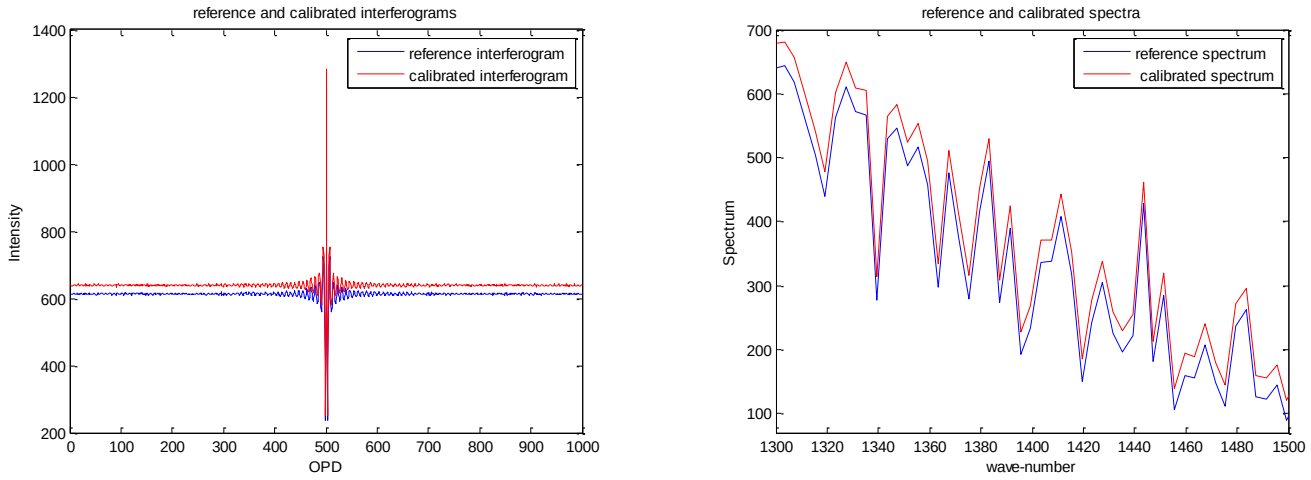

(a) Interferograms

(b) Spectra

Figure 5.4: Calibrated interferogram and spectrum compared to the references.

ferogram, we can construct the calibrated cube. Figure 5.5 shows a frame in the simulated cube before and after calibration and compares it to a reference frame. This shows that the proposed calibration process preserves the DC levels of the interferograms (the DC levels are what allows us to distinguish the targets in the figure).

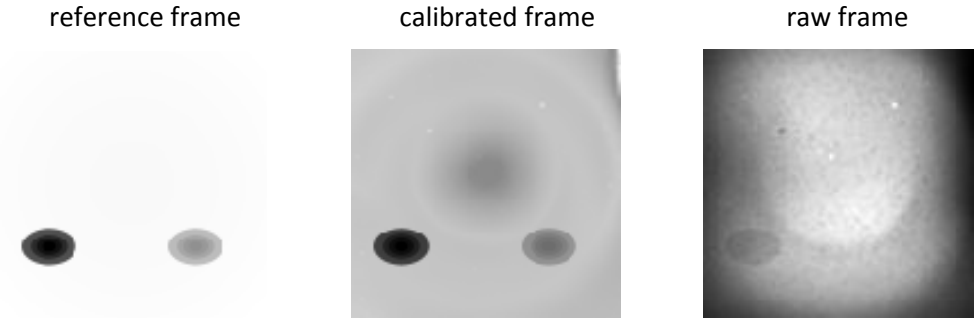

Figure 5.5: Stationary cube before and after calibration normalized to unity.

5.3 Calibrating an IFTS Scanning Moving Scenes

In this section we develop an algorithm to calibrate an IFTS data cube that contains one or more moving target in the field of view. We apply the algorithm on simulated data cubes generated from the simulator as well as on experimental data cubes from ABB Bomem.

5.3.1 Proposed Solution and Limits

In the case of an IFTS scanning moving targets, for various sections of the interferogram, we have different DC levels of unmodulated light. Each DC level contributes to the interferogram values when either the target or the background appears in the scanned spatial location. These DC levels are important to spatially distinguish between the targets and backgrounds when using motion estimation techniques. The boundaries between the targets and the background may be lost as a result of the effect of the gain and the offset parameter in the raw cubes. We need to find a procedure to calibrate the non-stationary raw cube to have a calibrated cube suitable for registration.

For the simulated data cubes, the targets are in absorption mode. The DC level for the background interferograms is therefore always higher than that of the targets. We can distinguish between the interferograms values from to the background or the targets with this DC level. The background is the BB that is used for calibration.

The steps to calibrate an IFTS scanning moving targets while preserving the DC levels are as follow:

1. Calculate the average level for the background interferogram by integrating the total power within the operating sensor band for all calibrated spectra of the background.

$$I_{BG}(0) = \frac{\sum_{k=1}^{k_{total}} 2 \int_{\sigma 1}^{\sigma 2} A_{BG}(\sigma)_k d\sigma}{k_{total}}$$

   where $I_{BG}(0)$ is the average level for the background interferogram, A_{BG} is a calibrated specrum in the background, and k_{total} is the total number of interferograms related to the background.

2. For every pixel in the raw data cube, convolve its interferogram with a low pass filter $h_{LP}(x)$ to capture changes in the unmodulated component of the interferogram and compute a normalized ratio function related to these changes.

$$I^{'}_{RF}(x) = h_{LP}(x) \otimes I^{'}(x)$$

$$I^{'}_{RF}(x) = I^{'}_{RF}(x)/max(I^{'}_{RF}(x)) \tag{5.8}$$

   where $I^{'}(x)$ is a raw interferogram, $I^{'}_{RF}(x)$ is the ratio function normalized to unity, and $\otimes$ is the convolution operator.

3. Compute the spectrum of each pixel and perform radiometric calibration, and force the out of sensor band to zero.

$$C(\sigma) = FT(I^{'}(x))$$

so, the calibrated spectrum is:

$$[A(\sigma)]_{\sigma 1}^{\sigma 2} = [\frac{C(\sigma)}{G(\sigma)} - O(\sigma)]_{\sigma 1}^{\sigma 2} \text{ where } A(\sigma) = 0 \text{ otherwise}$$

where $C(\sigma)$ is the raw spectrum, $A(\sigma)$ is the calibrated spectrum, and $G(\sigma)$, $O(\sigma)$ are the gain and offset used for calibration.

4. Compute an interferogram from the radiometrically calibrated spectrum.

$$I_1(x) = IFT(A(\sigma))$$

where $I_1(x)$ is the calibrated interferogram.

5. Add the average light level obtained in step 1 to the calibrated interferogram, and multiply the interferogram by the ratio function obtained in step 2:

$$I(x) = (I_1(x) + I_{BG}(0)) \times I_{RF}^{'}(x)$$

Ratio Function

In the process described above, we do not know the DC levels of the targets or the background. We compute the ratio between them (see Figure 5.6) by lowpass filtering the interferogram.

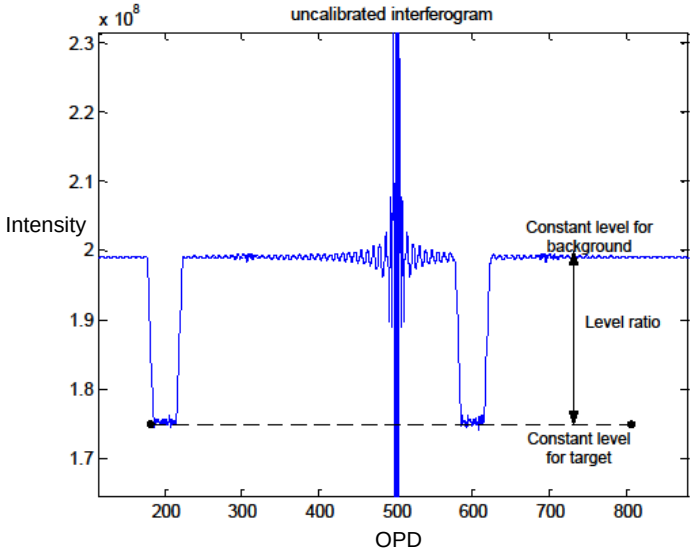

Figure 5.6: Interferogram of a pixel that views in alternance the background and the target during a scan.

We then use this ratio after calibration to restore the differences between the DC levels of the background and the targets. We have however to verify if the ratio of the DC levels in the calibrated data can be recovered from the raw data.

To show the issue, we start from the equations used for the stationary cube

$$\begin{aligned} B(\sigma) &= A(\sigma).G(\sigma) + O(\sigma) \\ I^{'}(x) &= I_0^{'}(x) + I_1^{'}(x) \\ I(x) &= I_0(x) + I_1(x) \end{aligned} \tag{5.9}$$

where $I_0(x)$ represents the DC levels for the unmodulated lights in the calibrated interferogram, and $I_0^{'}(x)$ represents the DC levels for the unmodulated lights in the raw interferogram.

$I_0(x)$ can be divided in several parts for non-stationary cubes. For our scenario where each pixel sees only either the background or the foreground, it is divided into two parts as follows: $I_{0\alpha}(x)$ is the DC level of the background, and $I_{0\beta}(x)$ is the DC level of the target. The values for the DC levels can be computed as discussed before as

$$\begin{aligned} I_{0\alpha}(x) &= 2\int_{\sigma 1}^{\sigma 2} A_\alpha(\sigma)d\sigma \\ I_{0\beta}(x) &= 2\int_{\sigma 1}^{\sigma 2} A_\beta(\sigma)d\sigma \end{aligned} \tag{5.10}$$

where, $A_\alpha(\sigma)$ is the spectrum of the background, and $A_\beta(\sigma)$ is the spectrum of the target.

For the raw interferogram, the DC levels can be computed as

$$\begin{aligned} I_0^{'}(x) &= 2\int_{\sigma 1}^{\sigma 2} B(\sigma)d\sigma \\ &= 2\int_{\sigma 1}^{\sigma 2} \left(A(\sigma)G(\sigma) + O(\sigma)\right)d\sigma \\ &= 2\int_{\sigma 1}^{\sigma 2} A(\sigma)G(\sigma)d\sigma + 2\int_{\sigma 1}^{\sigma 2} O(\sigma)d\sigma \end{aligned} \tag{5.11}$$

Similar to the previous equation, the DC level can be divided into two levels for the raw interferogram (we ignore the offset parameter because it can be removed based on the linearity property of Fourier transform):

$$\begin{aligned} I_{0\alpha}^{'}(x) &= 2\int_{\sigma 1}^{\sigma 2} A_\alpha(\sigma)G(\sigma)d\sigma \\ I_{0\beta}^{'}(x) &= 2\int_{\sigma 1}^{\sigma 2} A_\beta(\sigma)G(\sigma)d\sigma \ . \end{aligned} \tag{5.12}$$

While the gain is multiplied with the spectrum in the spectral domain, it is convolved with the interferogram and can therefore affect the differences between the DC levels of the unmodulated lights.

To verify if this is the case, we calculate $I_{0\alpha}(x)/I_{0\beta}(x)$, the ratio between the DC levels of the unmodulated lights for the calibrated background and two different targets. The obtained ratio values of 1.0314 for the carbon dioxide target, and 1.0864 for the water vapour target. We use the lowest density for the simulated targets to examine the worst case condition (i.e. the case with the smallest ratio). We then computed $I'_{0\alpha}(x)/I'_{0\beta}(x)$, the ratio between the levels of the unmodulated lights of the raw background and target at all pixel positions. The ratio maps are shown in Figure 5.7. In this figure, for the carbon dioxide, the minimum and

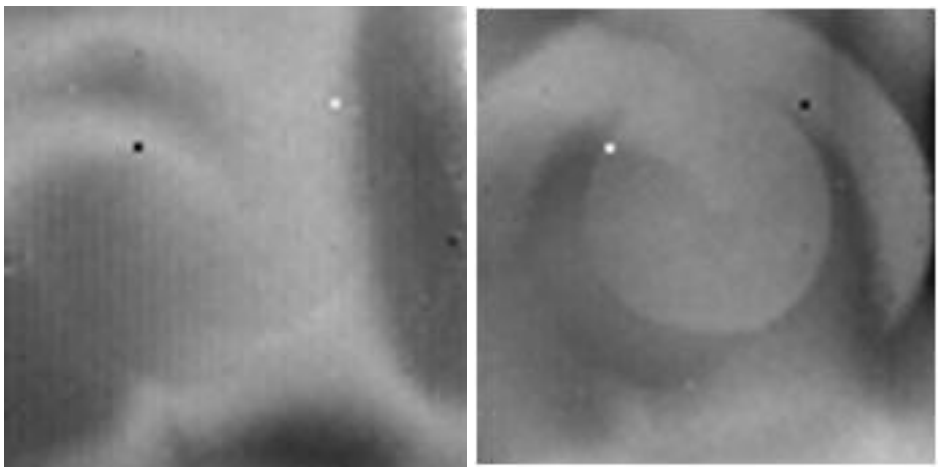

(a) Carbon dioxide (b) Water vapor

Figure 5.7: Ratio map between the dc levels in raw interferograms.

maximum values of the ratio are respectively 1.0092 and 1.0185, and for the water vapour, the minimum and maximum values are respectively 1.1184 and 1.1755. Although the ratio values are different from the values of the calibrated data, they are different and fairly constant for all pixels. This indicates that we can reliably differentiate the DC levels of the different targets from the raw data and validates our use of the ratio function. Note that this will usually be the case if the gain function $G(\sigma)$ is relatively flat spectrally, and if there is no inversion in the ratios before and after calibration. Finally, as we will explain below, the ratio function is only used to generate a data cube from which we will estimate motion vectors. Calibration of the motion compensated frames does use the ratio function.

5.3.2 Results for Calibrating Simulated Data Cubes with Moving Scenes

We simulated an IFTS data cube containing two targets moving in different directions. It has 1000 frames of 128×128 pixels. We also simulated a reference calibrated cube with the same motion vectors but without instrument gain and offset for comparison purpose. We calibrated the raw interferograms and compared them with those generated from the reference cube. We examine here interferograms in spatial locations with samples from both the background

and a moving water vapor target. Figure 5.8a shows an interferogram before calibration with different unmodulated light levels. The generated ratio function related to the unmodulated component is shown in Figure 5.8b.

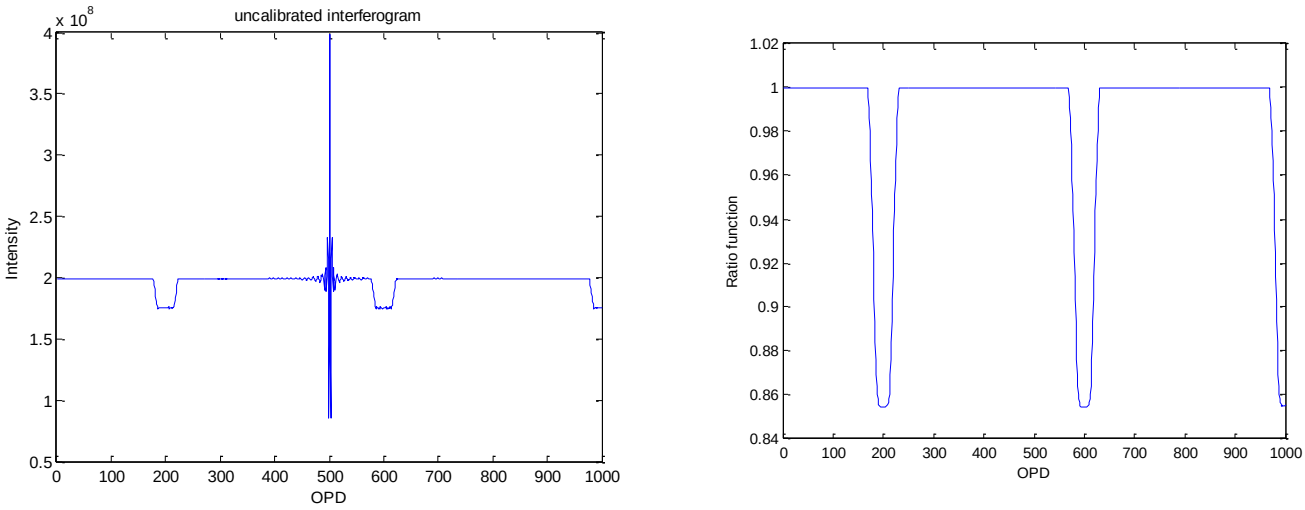

(a) Raw interferogram

(b) Ratio function

Figure 5.8: The raw interferogram and the ratio function.

Figure 5.9 shows the spectrum before and after calibration while forcing the out sensor band to zero after calibration. After radiometric calibration, the interferogram (Figure 5.10a) is multiplied by the ratio function. The result is shown in Figure 5.10b.

After calibrating all the interferograms in the raw IFTS data cube, we can construct the calibrated cube. Figure 5.11 shows some frames before and after calibration compared to the reference frames. The effect of the spatially non-homogeneous gain function on the frame contrast before calibration is apparent. After calibration we estimate the motion vectors between the frames and compare them with the motion vectors generated from the frames of the simulated reference calibrated cube as shown in the next section.

Motion and off-axis correction for the calibrated simulated cube

We use the GDIM motion estimation technique on the calibrated frames to generate the motion vectors. These motion vectors are applied on the calibrated cube without the unmodulated light. In this way we can avoid the errors generated from the low pass filter while generating the ratio function. The schematic shown in Figure 5.12 shows the complete procedure. The motion vectors obtained after applying the GDIM motion estimation technique on the calibrated data cube are shown in Figures 5.13 and 5.14. The real motion vectors are obtained from the actual motion, while the reference motion vectors are obtained from a reference calibrated cube with

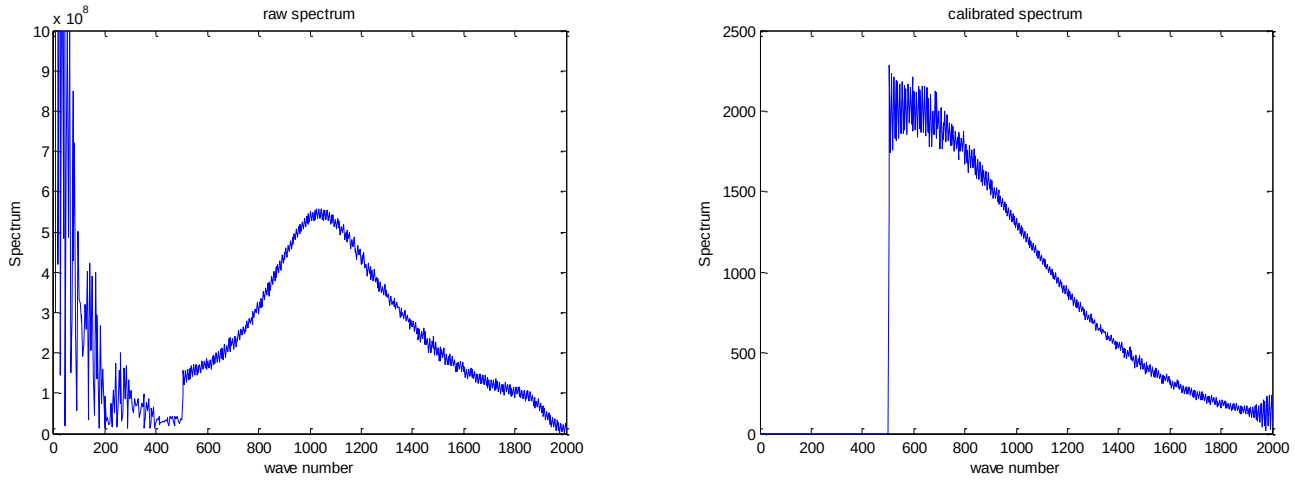

(a) Raw spectrum

(b) Calibrated spectrum

Figure 5.9: The raw and calibrated spectra.

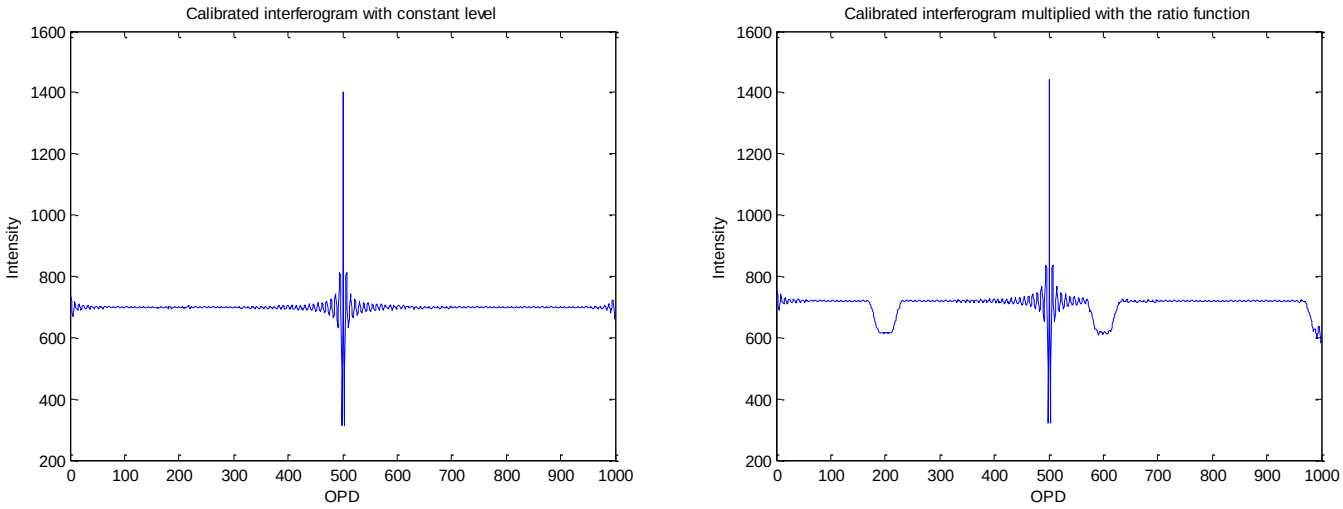

(a) Calibrated interferogram

(b) interferogram after applying the ratio function

Figure 5.10: The calibrated interferogram before and after applying the ratio function.

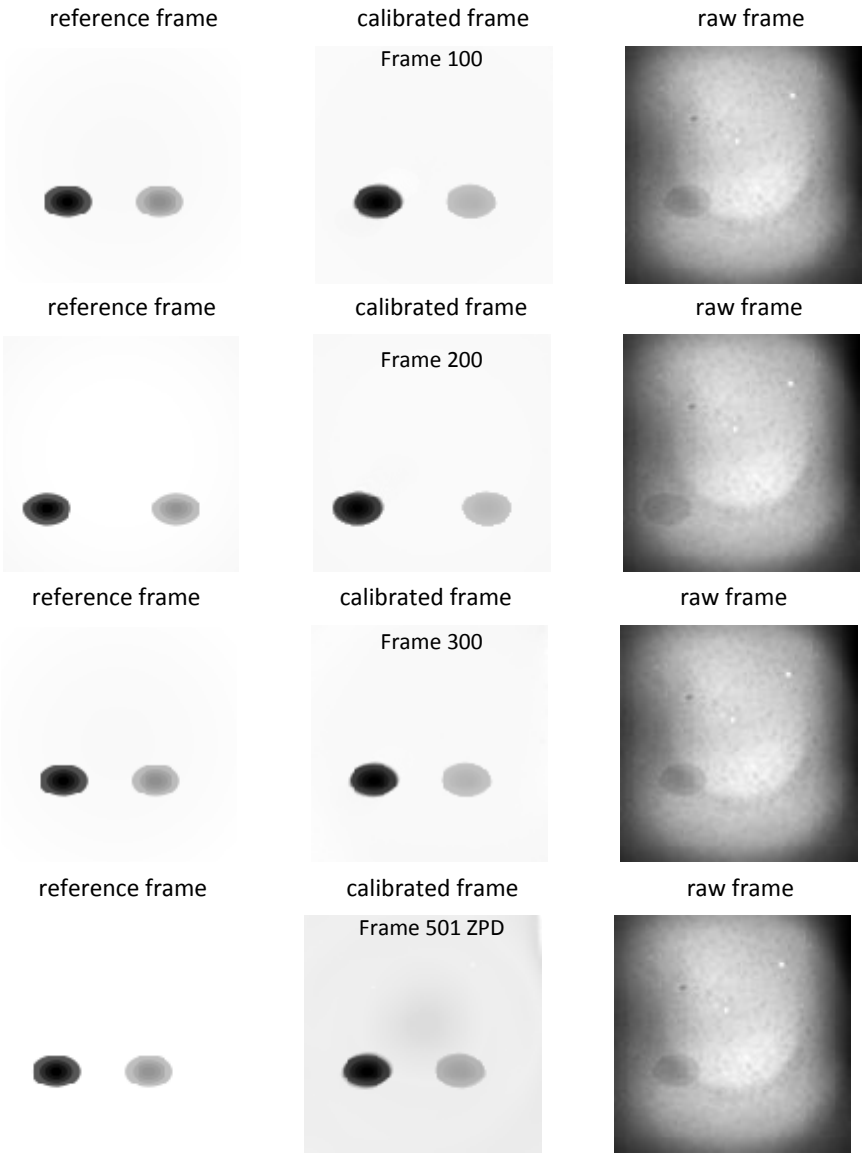

Figure 5.11: Non-stationary cube before and after calibration.

the same motion vectors but without instrument gain and offset. From the figure, we conclude that the motion vectors obtained from the calibrated cube coincide with the reference and the real motion vectors.

To illustrate the improvements in the motion vectors after calibrating the cube, the resulting motion vectors are subtracted from the known ones, and plotted for both the vertical and horizontal direction as shown in Figures 5.15 and 5.16. The calibration method does not affect the precision of the motion vectors as shown from the error curve. The errors in the

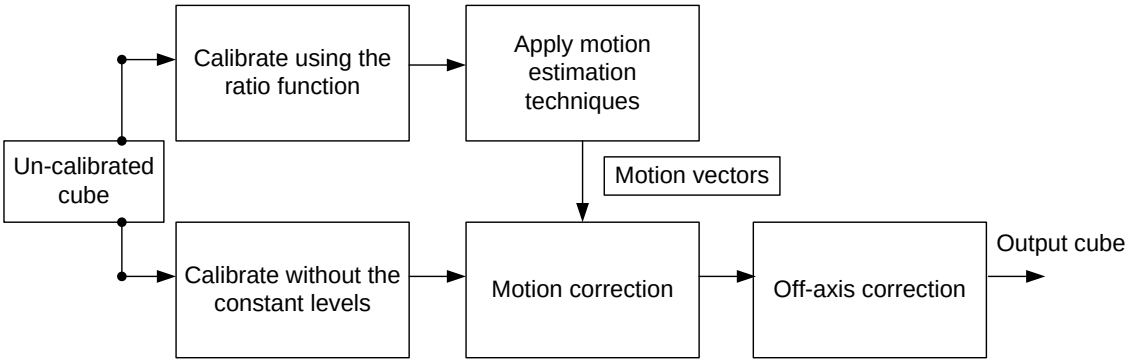

Figure 5.12: The complete procedure for calibration, motion, and off-axis correction.

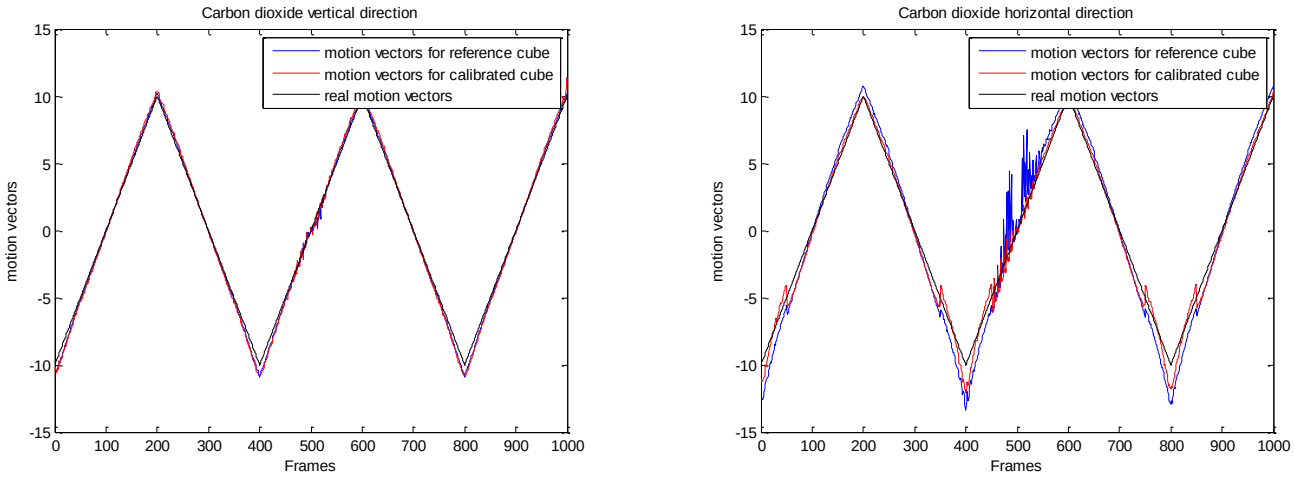

(a) Vertical

(b) Horizontal

Figure 5.13: Motion vectors for the carbon dioxide target using GDIM.

motion vectors of the carbon dioxide target is higher than the motion vectors of the Water vapour target. This can be related to the high absorption of the water vapour target that gives a high contrast with the background.

Figure 5.17a, is the interferogram of a pixel in the CO_2 target before and after motion correction compared to a ground truth. The ground truth is a stationary calibrated cube. We subtracted the unmodulated light from the interferograms for presentation purpose. We notice that the corrected interferogram coincides with the ground truth. Figures 5.17 b and c show the spectra of the CO_2 before and after motion correction. The zoom windows show the spectra at the wavenumbers where the CO_2 absorbs. The contribution of the motion correction algorithm is clear.

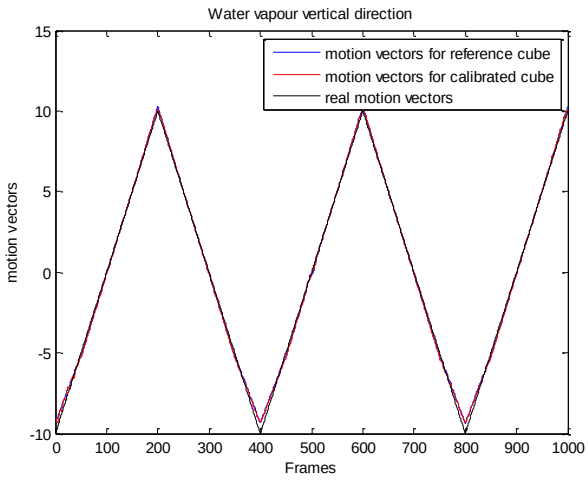

(a) Vertical

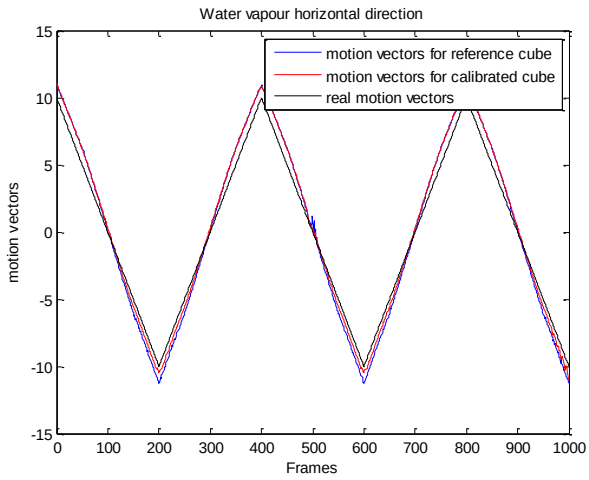

(b) Horizontal

Figure 5.14: Motion vectors for the water vapor target using GDIM.

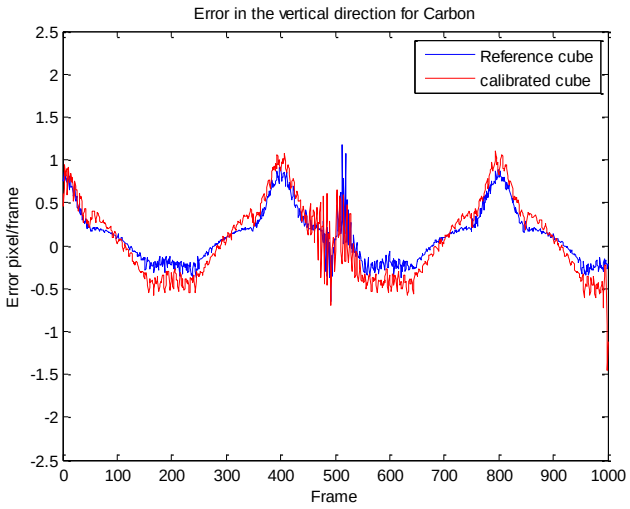

(a) Vertical

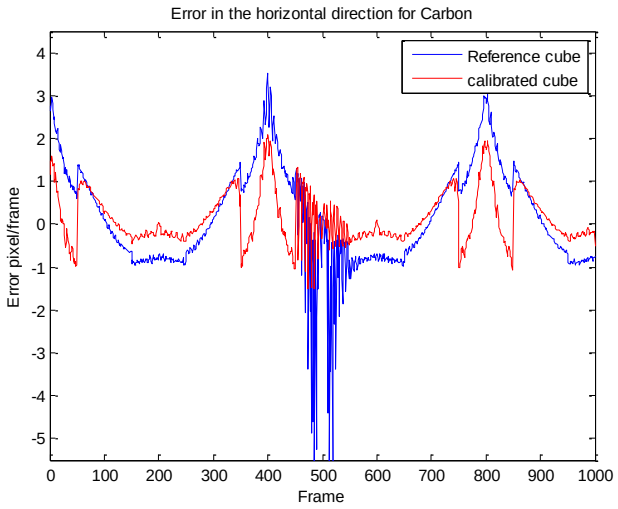

(b) Horizontal

Figure 5.15: Error in motion vectors for the carbon dioxide target using GDIM.

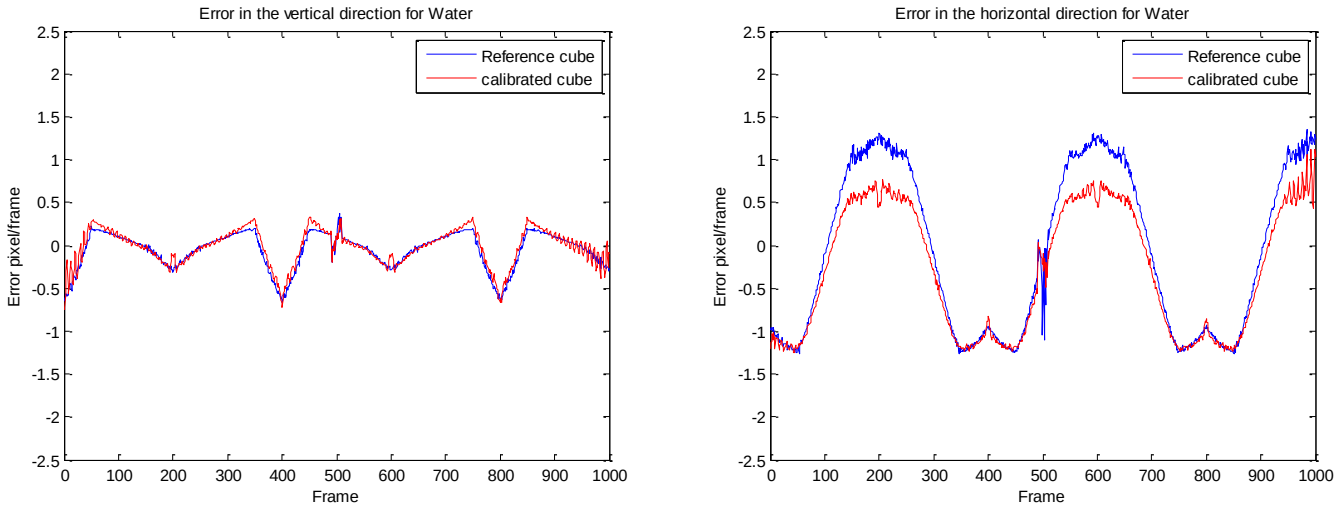

(a) Vertical

(b) Horizontal

Figure 5.16: Error in motion vectors for the water vapour target using GDIM.

Figure 5.18 shows the contribution of the off-axis correction algorithm in the spectrum domain that improves the resolution of the output spectrum, where it coincides with the spectrum of the ground truth. The zoom windows show the spectra at the wavenumbers where the CO_2 absorbs.

Similar results are obtained for a pixel in the H_2O target. The effect of the motion estimation algorithm is shown in Figure 5.19. The interferogram and spectrum of the H_2O after motion estimation correction coincides with the ground truth. Zoom windows of Figure 5.20 show the absorption wavenumbers for the calibrated H_2O before and after motion correction. The motion estimation correction algorithm improves the resolution of the spectral absorption lines of the H_2O. Off-axis correction algorithm has a high effect on the resolution of the spectral lines of the H_2O. The spectral lines after the off-axis correction coincides with the ground truth spectral lines. Figure 5.21 shows a zoom window of the spectral lines before and after off-axis correction.

5.3.3 Results for Calibrating Experimental Data Cubes with Moving Scenes

We acquired the experimental data cubes from the IFTS at ABB Bomem as shown in section 2.2.2. The IFTS scanned a toluene gas contained in a glass bulb and is moved by a motor in the horizontal direction forward and backward. The motor speed is set to be constant as much as possible. The system is guided by a monochromatic $HeNe$ laser at wavelength of $633nm$ for synchronization with the camera and scanned at a fringe rate of 15,798 fringes/sec. We use a camera with 16 bits/pixel, and each scan has between 8500 and 9000 frames. The

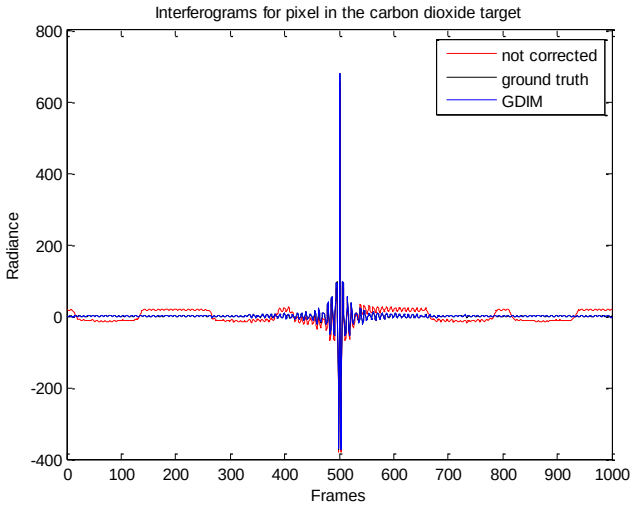

(a) Interferogram

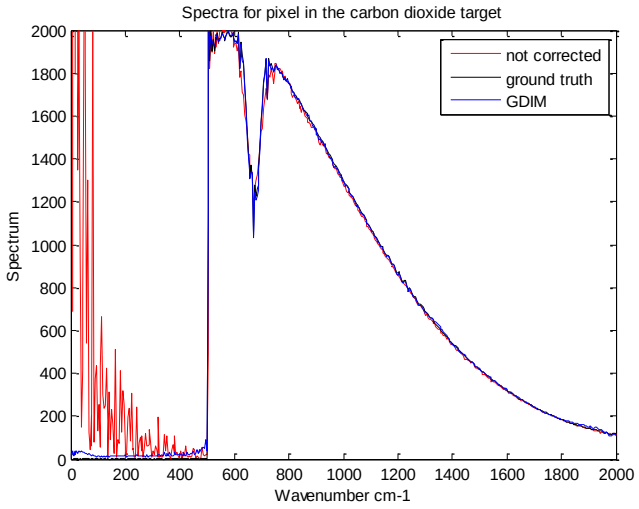

(b) Spectrum

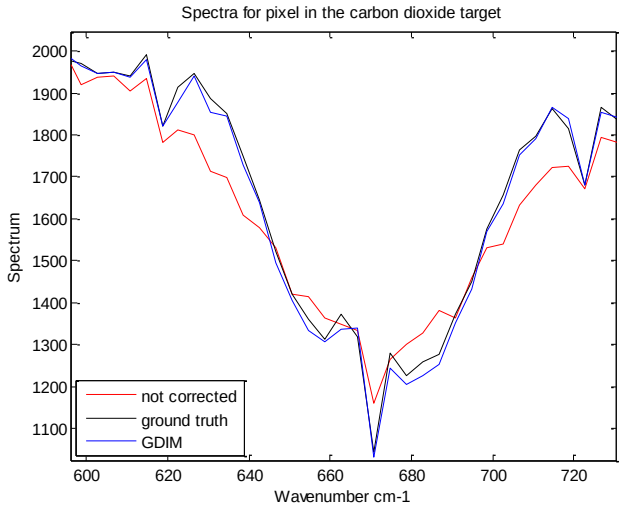

(c) Sensor operating band spectrum

Figure 5.17: Interferogram and spectrum for calibrated carbon dioxide before and after motion correction.

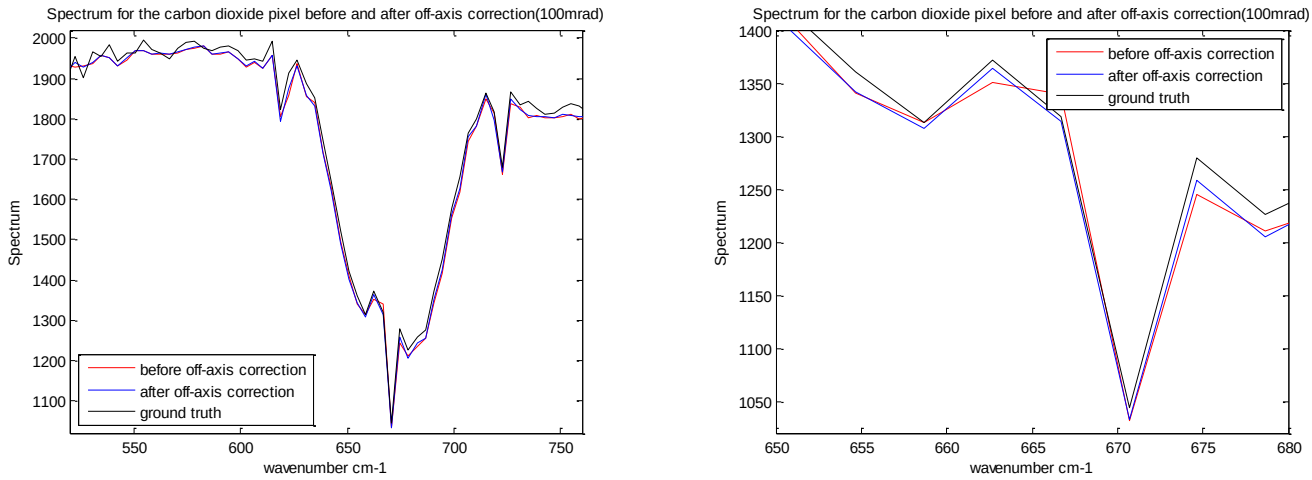

Figure 5.18: Calibrated carbon dioxide before and after off-axis correction.

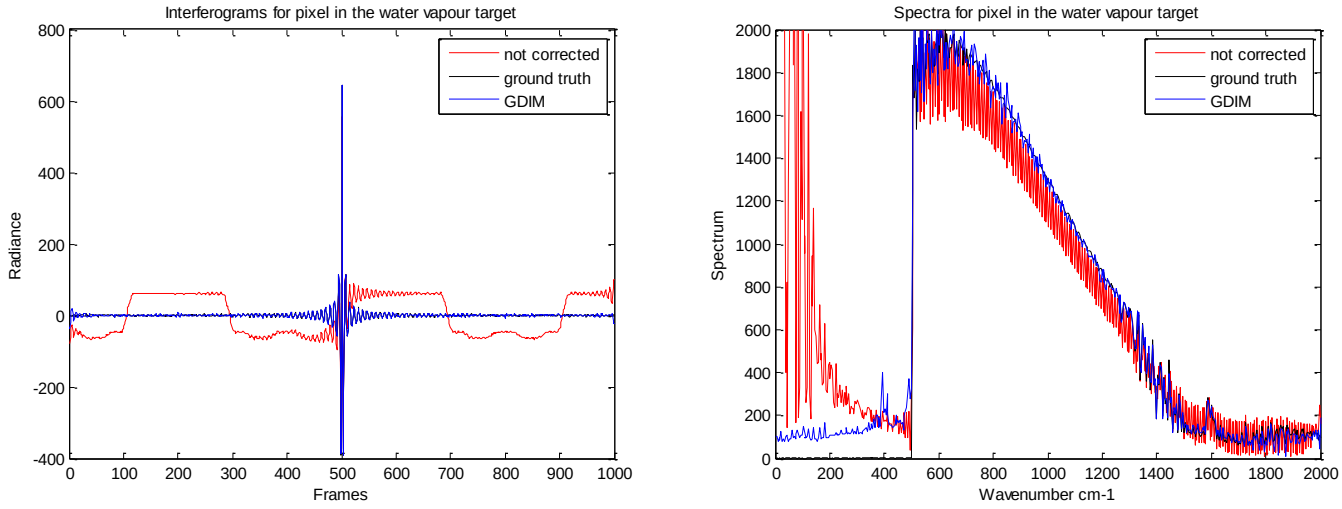

(a) Interferogram

(b) Spectrum

Figure 5.19: Interferogram and spectrum for calibrated water vapour before and after motion correction.

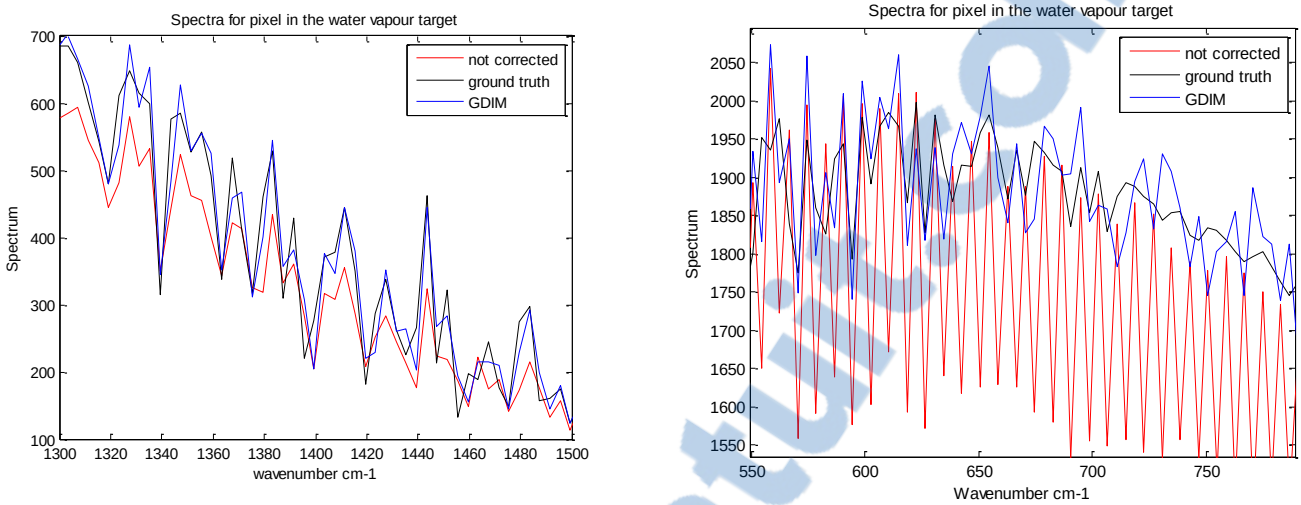

Figure 5.20: Calibrated water vapor spectrum before and after motion correction for the sensor operating band.

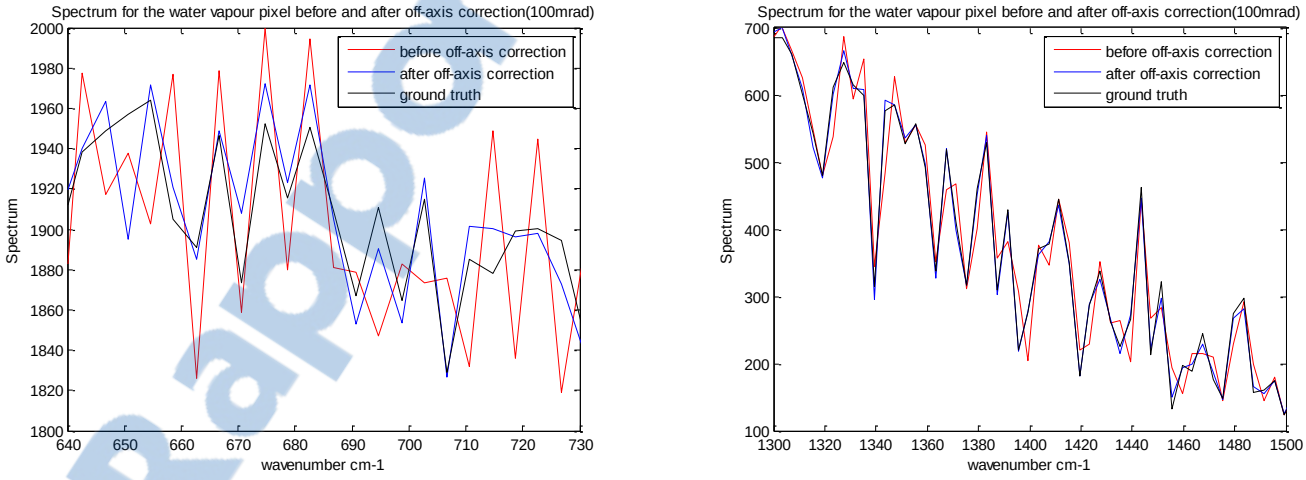

Figure 5.21: Calibrated water vapor spectrum before and after off-axis correction.

data cube is obtained by searching for the ZPD frame and cut an equal number of frames for both sides. Figure 5.22 shows some samples from the data cube. In this data cube, we

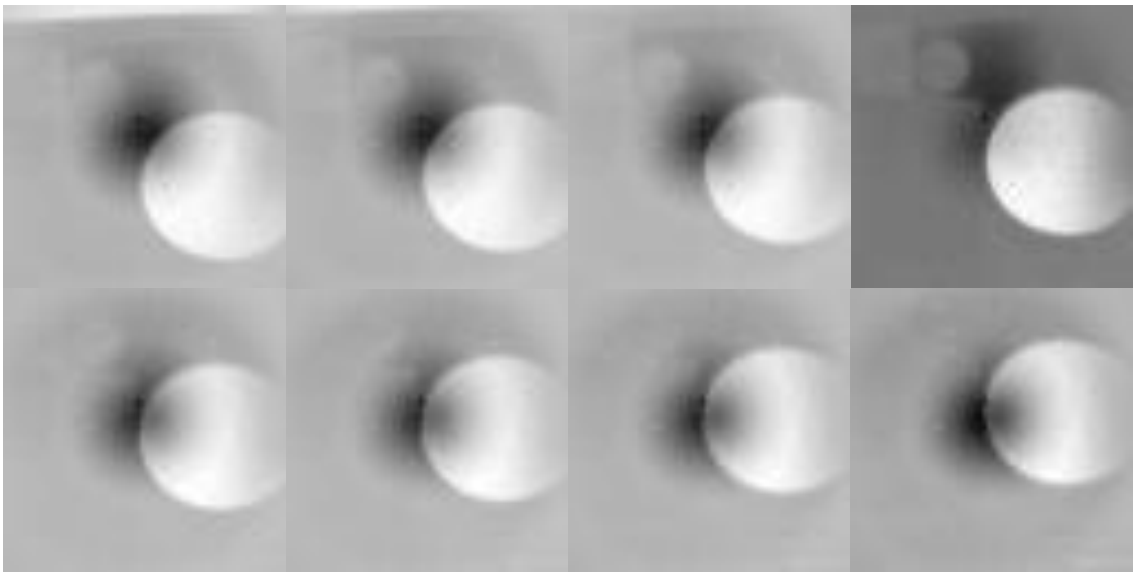

Figure 5.22: Toluene target moving, the frames show frame 1000 to 8000 in a step of 1000.

have interferograms assigned to the background only, interferograms assigned to the target only, and interferograms with samples assigned to both the background and the target. The background is a the metal glass holder for the glass bulb, while the target is the toluene gas bulb as discussed. Calibration now reuires differentiating between the pixels that only see the background or the target.

Steps to calibrate:

1. Separate the interferograms to differentiate those with samples assigned to the background only and those assigned to the target only by verifying their average level (obtained by integrating the calibrated spectra under the operating sensor band). In this setup, the DC value of the interferogram of the target is higher than that of the background. Also, the interferograms assigned to either the background or the target only have no change in their unmodulated light level, so we can distinguish them from the others.

$$I(0) = 2\int_{\sigma 1}^{\sigma 2} A(\sigma) d\sigma$$

where $I(0)$ is the average level for the interferogram with samples from either the background or target only, $A(\sigma)$ is its calibrated specrum. We choose a threshold for the background , and if $I(0)$ is greater than this threshold, we assign the interferogram to the target.

2. Calculate the average level for the background and the target interferograms by integrating the calibrated spectra for the wave numbers in the operating sensor band for the pixels that see the target or the background:

$$I_T(0) = \frac{\sum_{k=1}^{k_{total}} 2 \int_{\sigma 1}^{\sigma 2} A_T(\sigma)_k d\sigma}{k_{total}}$$

where $I_T(0)$ is the average level for the target interferogram, A_T is the target calibrated specrum, and k_{total} is the total number of interferograms related to the target;

$$I_{BG}(0) = \frac{\sum_{k=1}^{k_{total}} 2 \int_{\sigma 1}^{\sigma 2} A_{BG}(\sigma)_k d\sigma}{k_{total}}$$

where $I_{BG}(0)$ is the average level for the background interferogram, A_{BG} is the background calibrated specrum, and k_{total} is the total number of interferograms related to the background.

3. For every pixel in the raw data cube, convolve its interferogram with a low pass filter $h_{LP}(x)$ to capture changes in the unmodulated component of the interferogram and compute a normalized ratio function related to these changes.

$$I_{RF}^{'}(x) = h_{LP}(x) \otimes I^{'}(x)$$

$$I_{RF}^{'}(x) = I_{RF}^{'}(x)/max(I_{RF}^{'}(x))$$

where $I^{'}(x)$ is a raw interferogram, $I_{RF}^{'}(x)$ is the ratio function normalized to unity, and $\otimes$ is the convolution operator.

4. Compute the spectrum of each pixel and perform radiometric calibration, and force the out of sensor band to zero.

$$C(\sigma) = FT(I^{'}(x))$$

so, the calibrated spectrum is:

$$[A(\sigma)]_{\sigma 1}^{\sigma 2} = [\frac{C(\sigma)}{G(\sigma)} - O(\sigma)]_{\sigma 1}^{\sigma 2} \text{ where } A(\sigma) = 0 \text{ otherwise}$$

where $C(\sigma)$ is the raw spectrum, $A(\sigma)$ is the calibrated spectrum, and $G(\sigma)$, $O(\sigma)$ are the gain and offset used for calibration.

5. Compute an interferogram from the calibrated spectrum and multiply it by the ratio function.

$$I_1(x) = IFT(A(\sigma))$$

$$I_{interferogram}(x) = I_1(x) \times I_{RF}^{'}(x)$$

where $I_1(x)$ is the calibrated interferogram, and $I_{interferogram}$ is the calibrated interferogram after multiplying with the ratio function.

6. Add the average light level for the background to the samples of the background, and the average light level for the target to the samples of the target.

$$I(x) = \begin{cases} I_{interferogram}(x) + I_{BG}(0) & \text{for } x \in \text{back ground} \\ I_{interferogram}(x) + I_{T}(0) & \text{for } x \in \text{target} \end{cases}$$

We start by identifying the pixels whose interferograms only see either the target or the background from the pixels whose interferograms see both the target and background. We use the variation in the ratio function of each pixel to do this (high variation indicates that the pixel sees both the target and the background). Then we separate the interferograms assigned to either the background or the target according to their average energy. In this experiment, the average energy for the target is higher than the background. Other classification methods can be used for more complicated scenes. Figure 5.23 shows the spatial location for the interferograms assigned to either the background or the target.

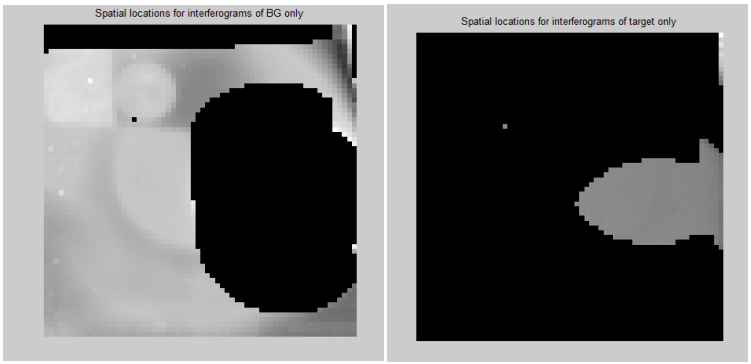

(a) Background only interferograms (b) Target only interferograms

Figure 5.23: Spatial locations for the background and target interferograms.

From the figure, we conclude that the separation method is efficient while there are still some misclassified spatial locations. The source of some of these errors are reflections on the target, and the bad pixels of the camera. The top pixels are misclassified as they see, for a few frames, the mechanical arm use to hold the toluene sample.

We examine three interferograms: one with samples related to the target only, one with samples related to the background only, and one which has samples from both the background and the target. Figure 5.24 shows the background interferogram before and after calibration. The unmodulated light level is calculated by integrating the total power within the sensor band as discussed. Figure 5.25 shows the target interferogram before and after calibration.

Figure 5.26a shows an interferogram before calibration starts with samples assigned to the target then samples assigned to the background. The generated ratio function related to

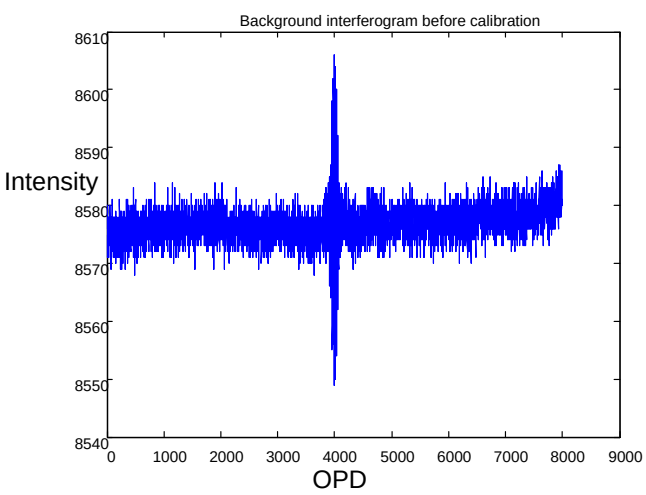

(a) Before calibration

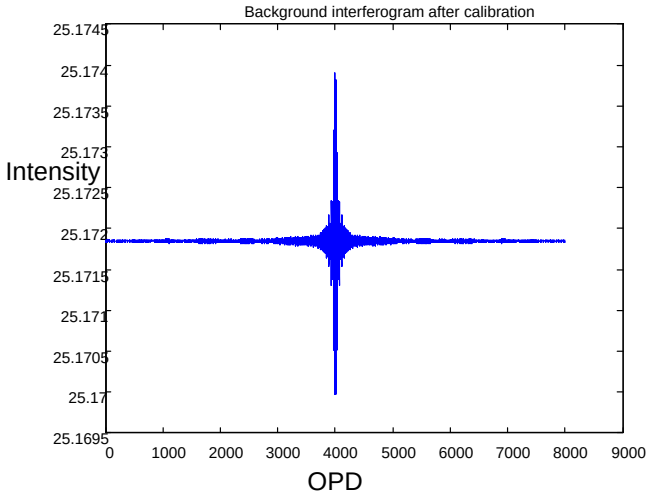

(b) After calibration

Figure 5.24: Interferograms for a background pixel before and after calibration.

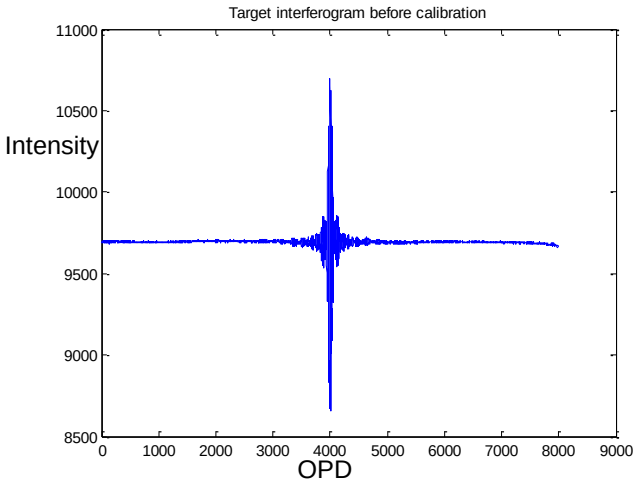

(a) Before calibration

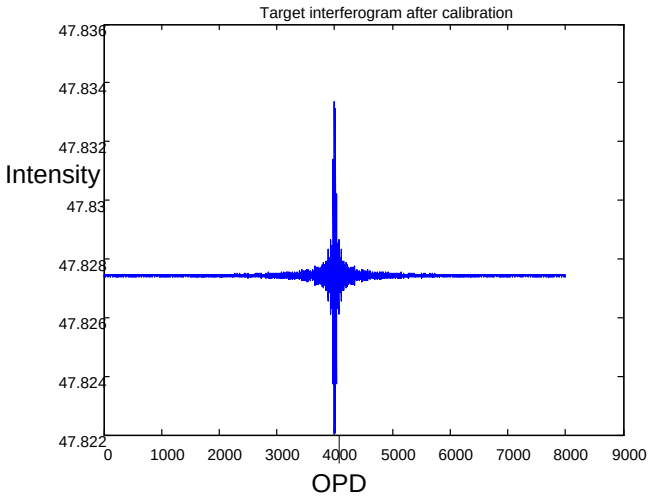

(b) After calibration

Figure 5.25: Interferograms for a target pixel before and after calibration.

the unmodulated component is shown in Figure 5.26b. After radiometric calibration, the

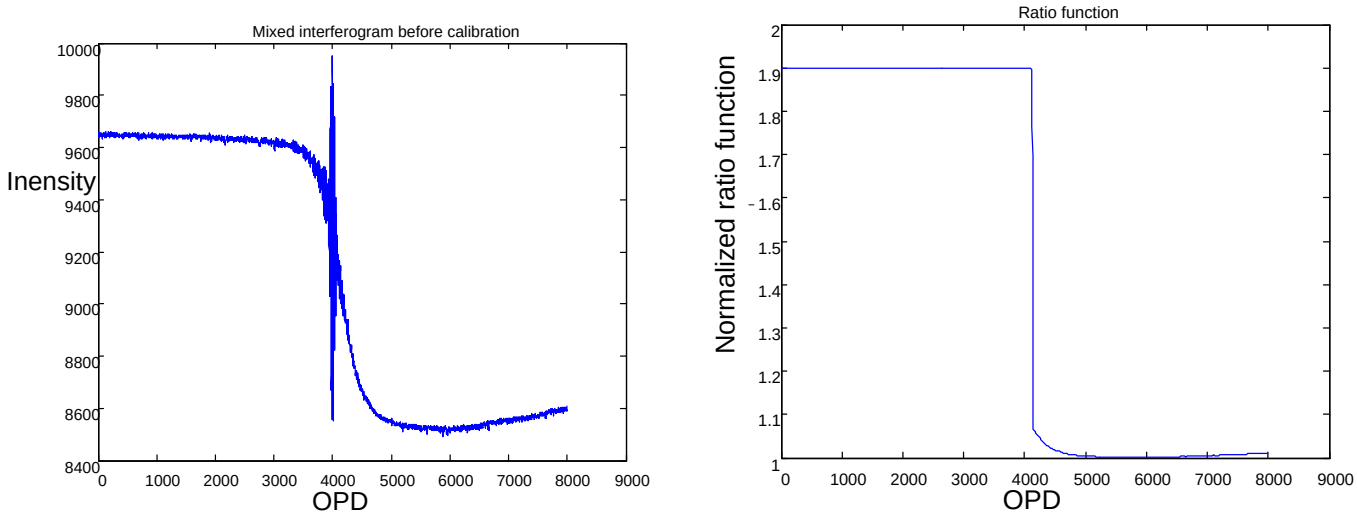

(a) Before calibration

(b) Ratio function

Figure 5.26: Interferograms contains samples from background and target before calibration, and the ratio function.

interferogram is multiplied by the ratio function. Then we add the average light level of the target to the samples of the target, and add the average light level of the background to the samples of the background. Figure 5.27 shows the calibrated interferogram and a zoom window around the ZPD.

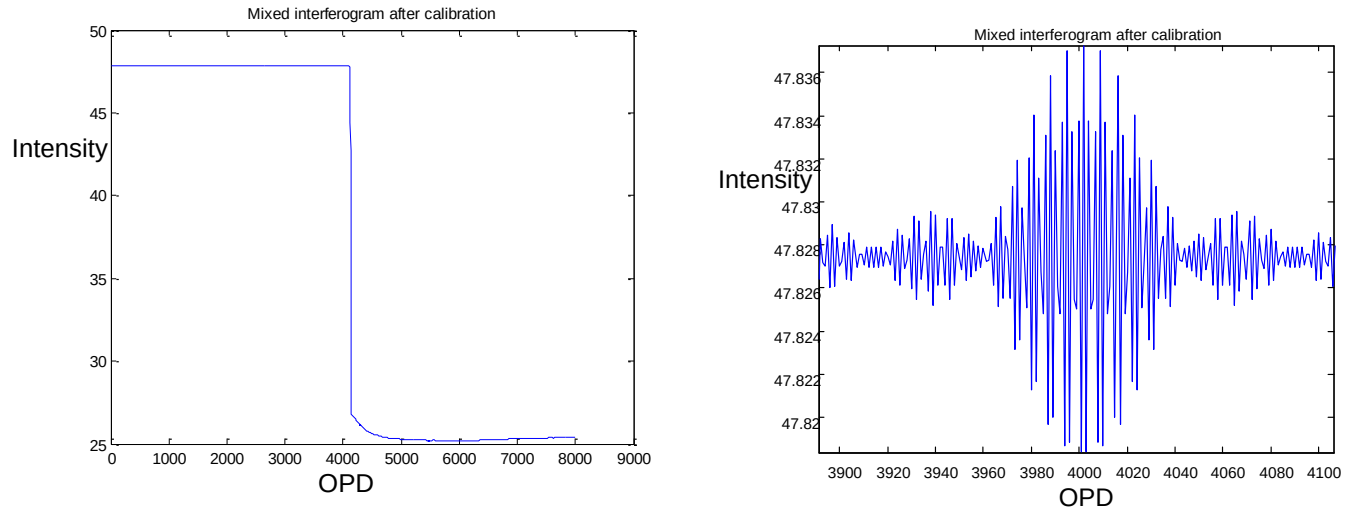

(a) After calibration and applying the ratio function

(b) Zoom window around ZPD

Figure 5.27: Interferogram for a pixel contains samples from background and target after calibration and a zoom window around the ZPD.

After calibrating all the interferograms in the raw IFTS data cube, we can construct the calibrated cube. Figure 5.28 shows some frames before and after calibration. After calibration, we estimate the motion vectors between the frames for registering as will be shown in the next section.

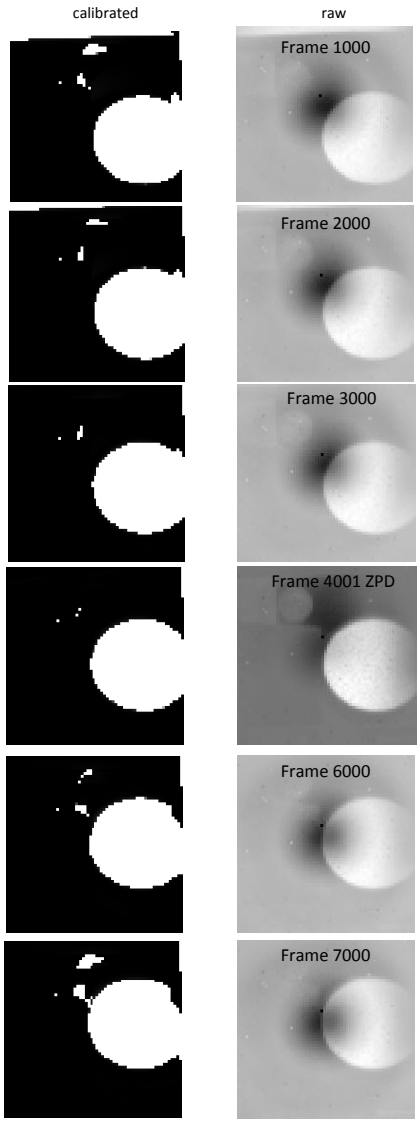

Figure 5.28: ABB non-stationary cube before (the right column) and after calibration (in the left column).

Motion Correction for Calibrated Experimental Cube

We use the phase-based method for generating the motion vectors between the frames. Figure 5.29 shows the motion vectors obtained with the phase-based pixel registration technique applied on both the raw and calibrated ABB data cube. We conclude that the target is moving in the vertical direction only. This matches with the experimental setup at ABB Bomem. Also, we conclude that the target moves around 16 pixels during the scan and by visual inspection for the target we confirmed the motion estimation results. By examining the pixel motion vectors around the ZPD frame, we recognize that the motion estimation algorithm gives better results for the case of the calibrated cube. The target moves smoothly with a constant velocity in the experiment setup. The motion vectors obtained for the calibrated cube shows a step progression in the motion, while for the raw cube the motion estimation algorithm failed to detect this progression. This is clearer when examining the sub-pixel motion vectors. We register the data cube on a pixel based registration, then apply the phase-based

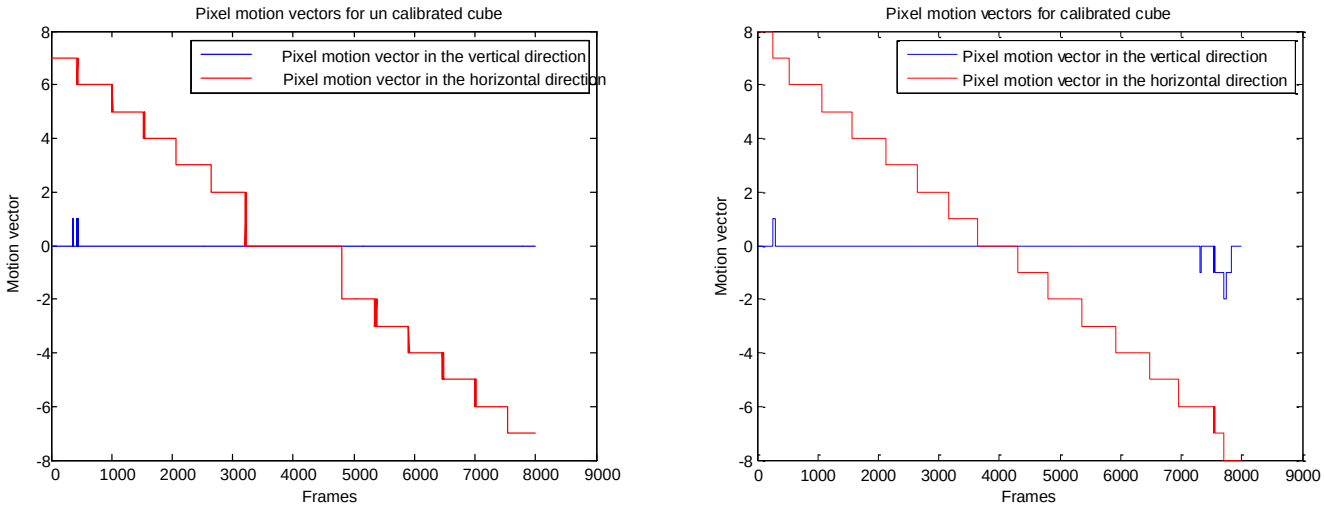

(a) Raw

(b) Calibrated

Figure 5.29: Pixel motion vectors for raw and calibrated toluene.

sub-pixel motion estimation on the pixel registered frames. Figure 5.30 shows the motion vectors for both the raw and calibrated cube. Although there are no reference motion vectors to compare with, we expect motion vectors related to a constant speed. A zoom window on the motion vectors obtained for the raw and calibrated ABB data cubes is shown in Figure 5.31. The figure shows the contribution of calibration step before motion estimation. Errors in the motion vectors appear around frames 3200 and 4800 for the raw cube in the vertical direction, while the motion vectors are smooth around these frames for the calibrated cube. We examine two pixels at the boundary of the toluene. Note that due to the slow motion of the target compared to the scan velocity, contribution for the motion estimation algorithm may

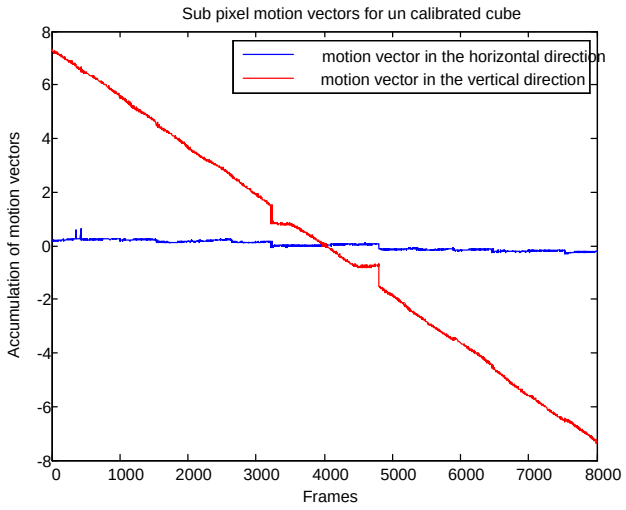

(a) Raw

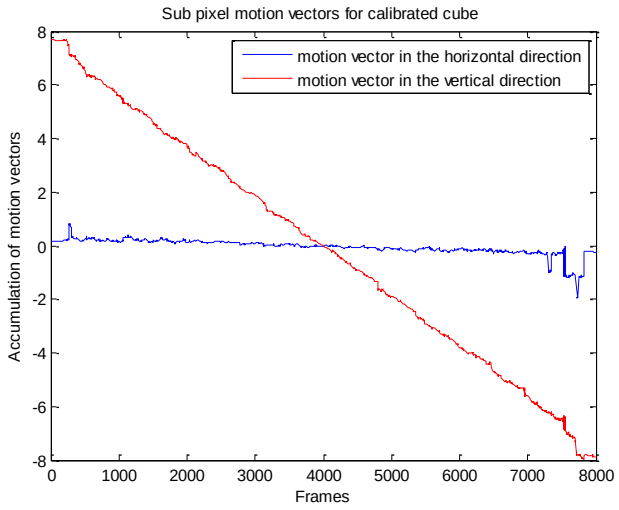

(b) Calibrated

Figure 5.30: Sub-pixel motion vectors for raw and calibrated toluene.

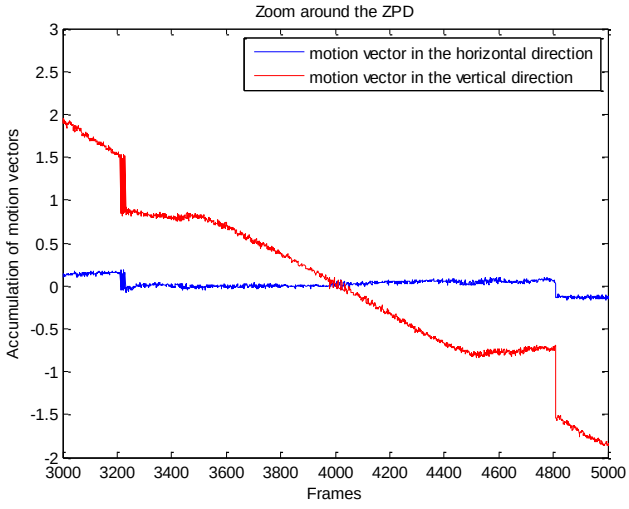

(a) Raw

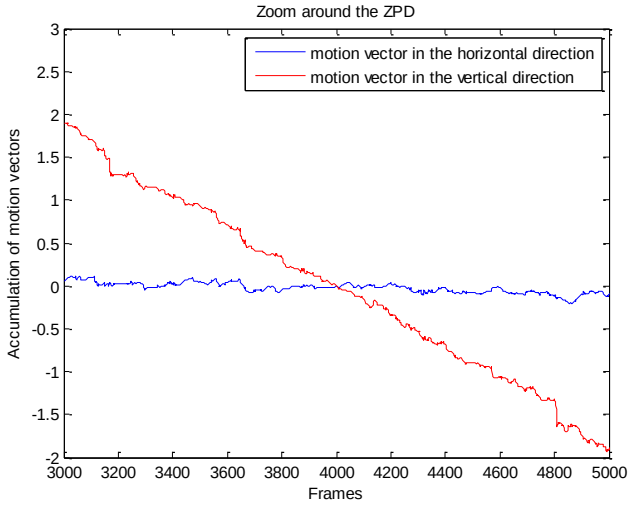

(b) Calibrated

Figure 5.31: Sub-pixel motion vectors for raw and calibrated toluene around the ZPD.

not be clear enough. The interferogram have enough samples around the ZPD to give a useful spectrum representing the target. Figure 5.32 shows the examined pixels at the ZPD frame. We compare three pixels from three different cubes to show the contribution of calibrating

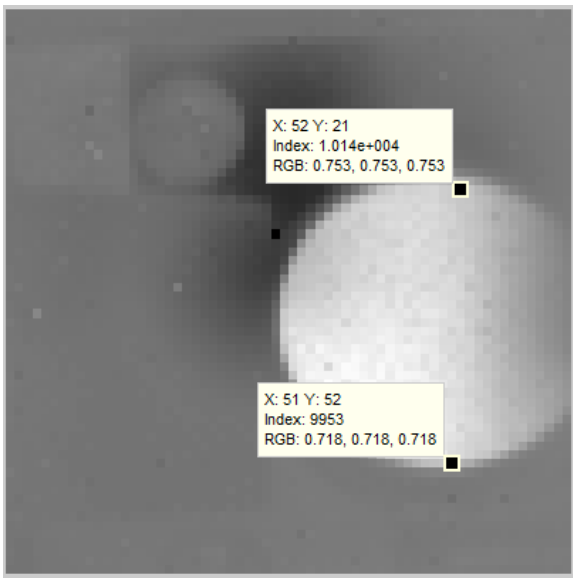

Figure 5.32: The ZPD frame and the examined pixels.

the data. The green curve shown in Figure 5.34a is the interferogram for a raw and moving pixel. The red curve is the interferogram for the raw pixel but after registering the frames of the cube using the motion estimation algorithm. Finally the blue curve is the interferogram for the same pixel after calibrating and registering the frames. The samples of the green interferogram starts with the background and then the samples of the target appear after the ZPD. After registering the cube, the samples of the interferogram are contributed to the target as shown by the red curve. The samples of the blue interferogram after calibration are also assigned to the target.

The contribution of calibrating the cube on the resolution of the output spectrum is shown in Figure 5.34b. The calibrated registered blue curve changed its slope to match with the reference spectrum of the toluene generated from a stationary calibrated cube shown in Figure 2.6. The calibration decreases the oscillations of the raw spectra presented by the red and green curves. Examining another pixel located in the lower border for the toluene target gives similar results. The samples of the green interferogram starts with the target and then the background appears because the toluene is moving to the upper direction. The contribution of calibrating and registering the cube is shown in Figure 5.34.

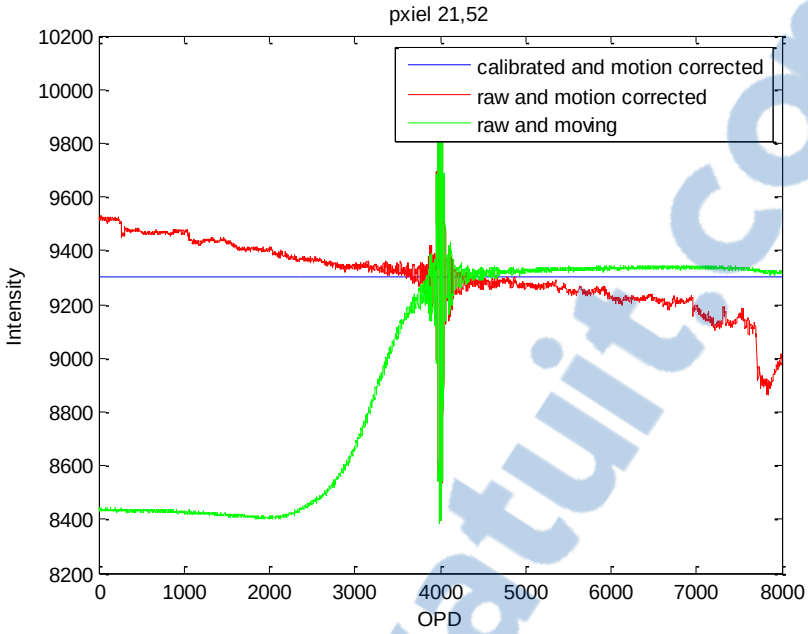

(a) Interferograms

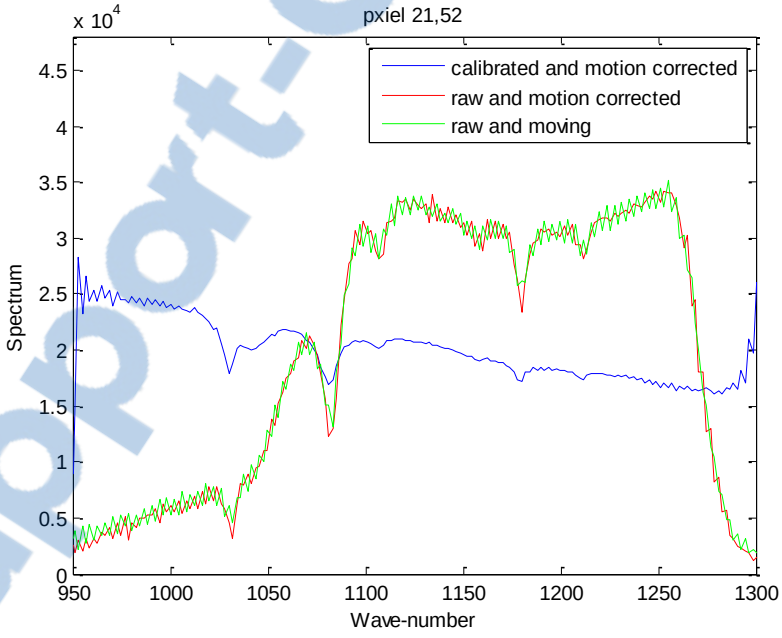

(b) Spectra

Figure 5.33: Pixel 21,52 before and after calibration and motion correction.

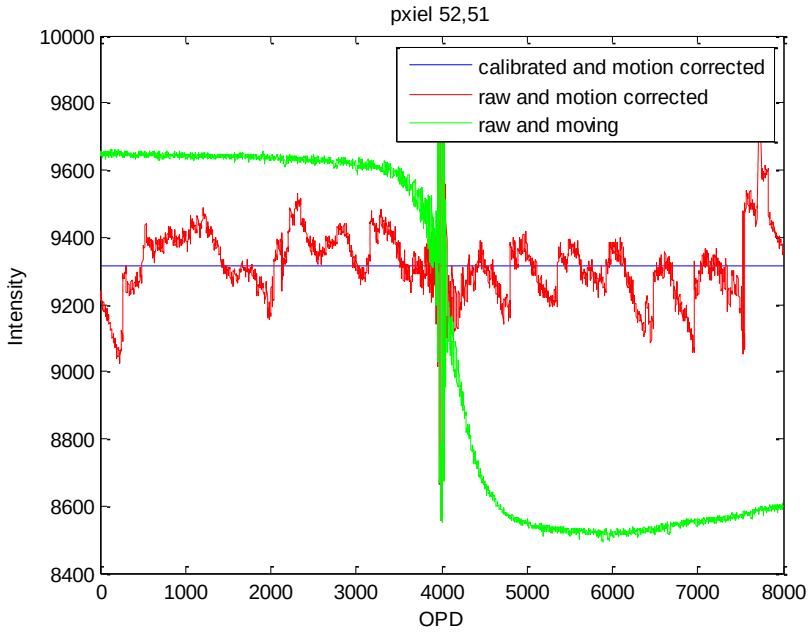

(a) Interferograms

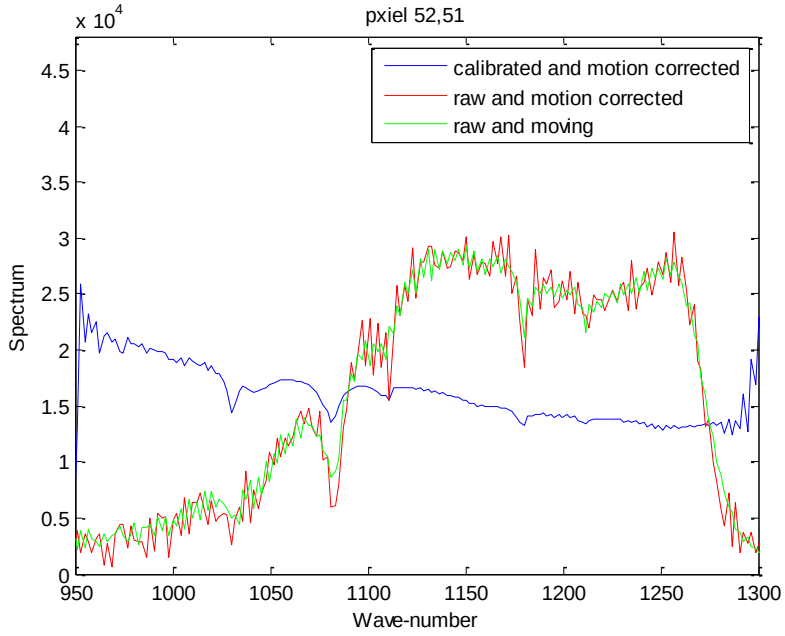

(b) Spectra

Figure 5.34: Pixel 52,51 before and after calibration and motion correction.

5.4 Conclusion

We presented a method for calibrating IFTS data cubes containing moving targets while preserving the unmodulated light level. The unmodulated light level is required for IFTS frame registration, which relies on the contrast between the targets and background space.We filtered the raw interferograms with a low pass filter to generate a ratio function that is applied on the calibrated interferograms. We obtain a calibrated IFTS data cube with a contrast suitable for the step of frame registration and motion compensation. Motion vectors obtained show competitive results for frame registration.

These motion vectors are then used to register the radiometric calibrated data frames, or compensate for target motion, followed by the off-axis correction. We used simulated and experimental data to validate our approach, and obtained spectral data with spectral accuracy and spectral resolution comparable to spectra computed from interferograms acquired when the scene and the IFTS are stationary.

Chapter 6

Conclusion and Future Work

6.1 Contributions

In this thesis, we showed that the spectra computed from interferograms acquired with an IFTS in presence of motion (either in the scene or simply relative to the instrument) have lower accuracy and resolution then the spectra computed in the absence of motion. We proposed to perform motion compensation a posteriori on the data cube to generate spectra with accuracy and resolution similar to spectra computed in the absence of motion. Processing the data a posteriori is more flexible than using a pointing mechanism at acquisition since it can compensate for relative motion between the instrument and the scene and also for motion within the scene.

In chapter 3, we cast the problem of motion compensation on interferograms as a problem of motion compensation without the brightness constancy hypothesis. We identified motion compensation techniques that were suitable for our scenario. We developed an algorithm that we successfully used to compensate for the relative motion between the instrument and the scene being imaged. The first algorithm uses a phase-based motion estimation algorithm with an approach based on mutual information. We integrated both algorithms taking into account the nature of our data. Particularly, our algorithm can efficiently deal with long sequences of frames without suffering from error accumulation. To compensate for motion with the scene, we modified the GDIM algorithm to take into account the particularity of the interferogram data around the zero path difference. We used simulated and experimental data to test our algorithms and evaluate their performance against a ground truth. Simulated data is generated from a simulator we designed to generate IFTS data cubes both in the LWIR and NIR band. The experimental data was acquired with a setup we built around the SPIOMM instrument. Results show that our algorithms can compensate for relative motion between the instrument and the scene, or for motion within the scene, and allow to retrieve spectral data with high spectral accuracy and spectral resolution.

In chapter 4, we explained that interferogram samples have off-axis distortion values that varies with the pixel spatial location from which they are acquired. This is a particularity of infrared Fourier transform spectrometers. This becomes an important issue when samples from different pixel locations are used to form an interferogram by motion compensation or frame registration. We developed an algorithm to resample the interferogram obtained by motion compensation. This algorithm assumes that the motion is slow enough so that the off-axis distortion parameters vary slowly with the interferogram samples. We tested our off-axis correction algorithm with our motion estimation algorithms on simulated and experimental data, and showed, against ground truth data, that it improved the the accuracy and resolution of the computed spectra.

In chapter 5, we addressed the effect that radiometric calibration, using spatial gain and offset functions, has on our motion estimation algorithms. Specifically, radiometric calibration does not preserve the DC levels (unmodulated light) of the interferograms. The DC levels of the interferogram are used by the motion compensation algorithms to register the frames and track a moving target. We develop an algorithm where the DC levels of the interferograms are estimated before calibration (we called those the ratio function). We showed that our approach to estimate these DC levels from the raw (uncalibrated data) was valid when the spectral gain function was relatively constant. We then apply the ratio function to the interferograms after radiometric calibration to generate data from which motion vectors can be estimated. These motion vectors are then used to register the radiometric calibrated data frames, or compensate for target motion, followed by the off-axis correction. As in the previous chapter, we used simulated and experimental data to valide our approach and show that we can compute, from interferogram data acquired with a moving IFTS or with motion in the scene, spectral data with spectral accuracy and spectral resolution comparable to spectra computed from interferograms acquired when the scene and the IFTS are stationary.

6.2 Future Research Avenues

Although the objectives of this research have been achieved, probing deeper, there are still other research opportunities to be investigated. Below, we propose directions for future research that could be derived from the work we presented in this thesis:

Frames Around the ZPD

Most of the errors in the motion vectors are present at the frames around the ZPD. This is a result of the high illumination variations encountered by these frames. Although we have used motion estimation techniques that work under this condition and modified the GDIM algorithm, there are still errors in the motion vectors. Future work can be directed for better motion estimation under the high illumination conditions around the ZPD. Also filtering the motion vectors around the ZPD may improve the results. The motion of the target or the

instrument is always restricted by some limits. The mechanical aspects of the instrument and the physical properties of the target control the motion. Motion vectors can be filtered to be cleared from unreasonable motion. Designing a suitable low pass filter is a challenging research problem. Its type, bandwidth, and the motion vectors where it can be applied will have a great effect on the results.

Mixing Off-axis Correction Algorithm Limitation

In chapter 4, we have designed an off-axis correction algorithm that processes a motion compensated interferogram sample by sample. We have assumed that the target is slow enough to consider the off-axis distortion of the adjacent samples on the motion corrected OPD are nearly the same. Although this assumption is reasonable for many IFTS scanners, future work may consider the case of fast targets moving in the scene of IFTS.

Calibration of Moving Targets with Multiple Constant Levels

In this thesis, we examined data cubes with distinguishable DC levels. We proposed the use of a ratio function to restore the DC variations in calibrated interferograms. This approach works when the ratio of the different DC levels is not inversed by the calibration. When this is not the case, the problem of taking into account the calibration in order to successfully register the frames remains an open problem.

In the case of two different DC levels (two targets or one target and the background), we estimate these levels by integrating their respective calibrated spectra. This works properly when the energy difference between the target and background is different. When there are many targets with different DC levels, classification or segmentation techniques need to be developped in order to estimate these DC levels.

A Priori Information

Although it seems that the output interferograms and spectra for practical data cannot be compared with any other reference to know if the output is acceptable or not, this is not quite the case. We have some a priori information about the spectra that we compute. For exemple, the out-of-sensor band spectrum that we compute should be zero. This information should be factored in the processing chain (calibration, motion estimation, off-axis correction).

Bibliography

[1] Ninth workshop on infrared remote sensing applications. *WIRSA, Quebec, Canada*, 2008.

[2] Internet site. "`http://www.bhkinc.com/`", 2012.

[3] Internet site. "`http://www.hitran.com/`", 2012.

[4] KR. Bambery, E. Schultke, BR. Wood, ST. Rigley MacDonald, K. Ataelmannan, RW. Griebel, BH. Juurlink, and D. McNaughton. "A Fourier transform infrared micro spectroscopic imaging investigating into an animal model exhibiting glioblastoma multiforme". *Biochimica et Biophysica Acta (BBA)-Biomembrances*, 1758:900–907, 2006.

[5] R. Bhargava. "Towards a practical Fourier transform infrared chemical imaging protocol for cancer histopathology". *Analytical and Bioanalytical Chemistry*, pages 1618–2642, 2007.

[6] H. Chen. "On registration of regions of interest (ROI) in video sequences". *Proceeding of the IEEE Conference on advanced video and signal based surveillance, AVSS*, 2003.

[7] Y. J. Chen, Y. D. Cheng, H. Y. Liu, P. Y. Lin, and C. S. Wang. "Observation of biochemical imaging changes in human pancreatic cancer tissue using Fourier transform infrared microspectroscopy". *Chang Gung Med J.*, 29, 2006.

[8] C. Cheung and L. Po. "A novel small cross-diamond search algorithm for fast video coding and video conferencing applications". *IEEE Conference on Image Processing*, 2002.

[9] T. Cover and J. Thomas. *Elements of information theory.* John Wiley and Sons, 1991.

[10] S. Davis. *Fourier transform spectrometry.* San Diego Academic press, 2001.

[11] L. Drissen. "Science results from the imaging Fourier transform spectrometer SpIOMM". *Ground-based and Airborne Instrumentation for Astronomy II, SPIE*, 2008.

[12] L. Drissen. "SpIOMM, a wide-field imaging FTS for astronomy". *In Fourier Transform Spectroscopy (FTS) Topical Meeting, OSA Optics and Photonics Congress, Vancouver*, page FTuA2, 2009.

[13] C. Fookes, A. Maeder, S. Sridharan, and J. Cook. "Multi-spectral stereo image matching using mutual information". *Proceedings of the 2nd international symposium on 3D data processing, visualization, and transmission (3DPVT 04)*, 2004.

[14] J. Genest and P. Tremblay. "Instrument line shape of Fourier transform spectrometers: analytic solutions for nonuniformly illuminated off-axis detectors". *Applied Optics*, 38:5438–5446, 1999.

[15] F. Grandmont, A. Bernier, M. Charlebois, and L. Drissen. "SpIOMM: a ground-based wide-field imaging FTS". *In Fourier Transform Spectroscopy (FTS) Topical Meeting, OSA Optics and Photonics Congress, Santa Fe, New Mexico*, page FWC4, 2007.

[16] F. Grandmont, J. Lavigne, and L. Drissen. "SpIOMM: an imaging FTS for astronomy". *In Fourier Transform Spectroscopy (FTS) Topical Meeting, OSA Optics and Photonics Congress, Quebec*, page PD1, 2003.

[17] R. Harig, R. Braun, C. Dyer, C. Howle, and B. Truscott. "Short-range remote detection of liquid surface contamination by active imaging Fourier transform spectrometry". *Optics Express*, 16:5708–5714, 2008.

[18] F. Harris. "On the use of windows for harmonic analysis with the discrete Fourier transform". *Proceedings of the IEEE*, 66(1):51–83, 1978.

[19] H. Haussecker and D. Fleet. "Computing optical flow with physical models of brightness variation". *IEEE Transaction on Pattern Recognition and Machine Intelligence*, 23(6):661–673, 2001.

[20] E. Hirsch and E Agassi. "Detection of gaseous plumes in IR hyperspectral images using hierarchical clustering". *Applied Optics*, 46:6368–6374, 2007.

[21] B. Horn. *Robot vision.* The MIT press, 1986.

[22] B. Horn and B. Schunck. "Determining optical flow". *Artificial Intelligence*, 17:185–203, Aug. 1981.

[23] A. Jacobsen. *Analyzing airborne optical remote sensing data from a hyper-specral scanner and implications for environmental mapping and monitoring.* PhD thesis, university of Copenhagen, 2000.

[24] J. Kauppinen. *Fourier transform in spectroscopy.* Berlin, Germany, Willey-VCH, 2001.

[25] R. Li, B. Zeng, and M. Liou. "A new three-step search algorithm for block motion estimation". *IEEE Transaction on Circuits and Systems for Video Technology*, 4(4):438–442, 1994.

[26] Y. Liao, N. Chiu, C. Weng, and Y. Sun. "Registration and normalization techniques for assessing brain functional images". *Biomedical Engineering-Applications, Basis and Communications*, 15(3):87–94, 2003.

[27] K. Liou. *An introduction to atmospheric radiation.* New York, Academic press, 1980.

[28] B. Lucas. "An iterative image registration technique with an application to stereo vision". *Proceeding of imaging understanding workshop*, pages 121–130, 1981.

[29] A. Mahgoub, T. Nguyen, R. Desbiens, and A. Zaccarin. "Aligning the frames of a non stationary IFTS for spectrum retrieval". *IEEE Conference on Image Processing, Egypt*, 2009.

[30] A. Mahgoub, T. Nguyen, R. Desbiens, and A. Zaccarin. "Retrieving a spectrum from a non stationary imaging Fourier transform spectrometer". *In Fourier Transform Spectroscopy (FTS) Topical Meeting, OSA Optics and Photonics Congress, Vancouver*, page FThA5, 2009.

[31] A. Mahgoub, T. Nguyen, R. Desbiens, and A. Zaccarin. "Retrieving a high resolution spectrum from a moving target in an imaging FTS for astronomy". *In Fourier Transform Spectroscopy (FTS) Topical Meeting, OSA Optics and Photonics Congress, Toronto*, page FTuB3, 2011.

[32] J. P. Maillard and D. Simons. "Spectro-imaging mode of the CFHT-FTS with a NICMOS camera: first results". *ESO Conf. On Progress in Telescope and Instrumentation Technologies, ESO Conference and Workshop Proceedings, Garching*, pages 733–739, 1992.

[33] G. Nave. "Measurements at NIST in support of the search for exponents". *In Fourier Transform Spectroscopy (FTS) Topical Meeting, OSA Optics and Photonics Congress, Toronto*, page FTuA1, 2011.

[34] S. Negahdaripour. "Revised definition of optical flow: integration of radiometric and geometric cues for dynamic scene analysis". *IEEE Transaction on Pattern Analysis and Machine Intelligence*, 20:961–979, 1998.

[35] T. Nguyen, A. Mahgoub, R. Desbiens, and A. Zaccarin. "Super resolution for an imaging Fourier transform spectrometer". *In Fourier Transform Spectroscopy (FTS) Topical Meeting, OSA Optics and Photonics Congress, Vancouver*, page JTuB13, 2009.

[36] L. Po and W. Ma. "A novel four-step search algorithm for fast block motion estimation". *IEEE Transaction on Circuits and Systems for Video Technology*, 6(3):313–317, 1996.

[37] A. E Potter. *Multispectral imaging system.* U.S. Patent 3702,735, 1972.

[38] H. Revercomb, H. Buijs, H. Howell, D. LaPorte, W. Smith, and L. Sromovsky. "Radiometric calibration of IR Fourier transform spectrometers: solution to a problem with the high-resolution interferometer sounder". *Applied Optics*, 27(15), 1988.

[39] S. Roy, S. Potvin, J. Genest, and R. Desbiens. "Fast line-shape correction procedure for imaging Fourier-transform spectrometers". *Applied Optics*, 46:4674–4679, 2007.

[40] T. Smithson. "AIRIS : The Canadian Airborne Infrared Hyperspectral Imager: Current status and future developments". *In Fourier Transform Spectroscopy (FTS) Topical Meeting, OSA Optics and Photonics Congress, Santa Fe, New Mexico*, page FThb, 2007.

[41] Nasa/Goddard space flight centre. The remote sensing tutorial. "`http://rst.gsfc.nasa.gov/`", 2008.

[42] L. Spencer, D. Naylor, and B. Swinyard. "Performance evaluation of the Hershel/SPIRE imaging Fourier transform spectrometer". *SPIE, Space Telescopes and Instrumentation I: Optical, Infrared, and Millimeter*, 6265, 2006.

[43] T. S. Spisz, P. K. Murphy, C. C. Carter, A. K. Carr, A. Vallieres, and M. Chamberland. "Field test results of standoff chemical detection using the FIRST". *In Proceedings of SPIE, Chemical and Biological Sensing VIII*, 6554, 2007.

[44] H. Stone, M. Orchard, E. Chang, and S. Martucci. "A fast direct Fourier-based algorithm for sub pixel registration of images". *IEEE Transactions on Geoscience and Remote Sensing*, 39(10):313–317, 2001.

[45] B. D. Tait and R. Parade. "Fourier transform infrared imaging as a method for detection of HLA class I expression in melanoma without the use of antibody". *Tissue Antigens*, 69:252–258, 2007.

[46] M. Tekalp. *Digital video processing*. Prentice Hall Signal Processing Series, 1995.

[47] J. Tian. *Reconstruction of irregularly sampled interferograms in imaging Fourier transform spectrometry*. PhD thesis, Georgia Institute of Technology, 2004.

[48] G. Toon, P. Wennberg, V. Hipkin, and J. Drummond. "The mars atmosphere trace molecule occultation spectrometer". *In Fourier Transform Spectroscopy (FTS) Topical Meeting, OSA Optics and Photonics Congress, Toronto*, page FTuA2, 2011.

[49] I. Vajda. *Theory of statistical inference and information*. Kluwer Academic, Dordrecht, The Netherlands, Aug. 1989.

[50] W. Wolfe. *Introduction to radiometry*. Spie press, 1998.

[51] R. Wutfz, E. Wishnow, S. Blais-Ouellette, K. Cook, B. Holden, D. Carr, and C. Stubbs. "Gallery of data cubes obtained from the livermore imaging Fourier transform spectrometer". *SPIE Astronomical Telescope and Instrumentation, SPIE Conf. Ser, Hawaii*, 2002.

Appendix A

Simulator Setup

In this section, we discuss the parameters of the simulator we developed for our research, the data cubes it generates and the different scenarios we built to generate data.

A.1 Input Spectrum

In chapter two, we discussed the case of a gas in absorption or transmission mode (in the LWIR band). We gave the equations to compute the gas spectrum. In this section, we discuss the case when more than one gas is seen on by an instrument. This case is not used in the thesis, however it can be generated by the simulator.

A.1.1 Two successive Gases in LWIR Band

In this scenario, we want to compute the spectrum that will be measured by an IFTS when it sees multiple layer of gas. As an example, an IFTS scans a plume of CO_2 gas released from a chimney, the plume of gas is released in front of an H_2O layer and the IFTS is directed toward the earth. Figure A.1 describes this scenario. The output radiance of the first gas plume is

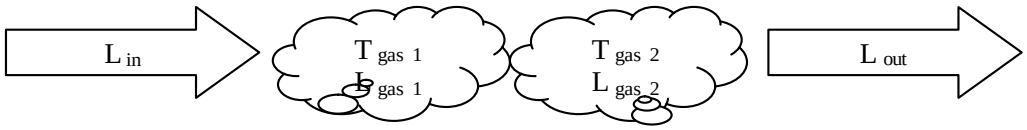

Figure A.1: Scenario for successive gases in absorption or transmission mode.

the input radiance for the second gas and so on as described in the following equation:

$$L_{out} = ((L_{in}T_{gas1} + L_{gas1}(1 - T_{gas1}))T_{gas2} + L_{gas2}(1 - T_{gas2})) \tag{A.1}$$

Referring to the previous exemple, H_2O is combined with the background, and then the CO_2 can be placed in front of this combination. The background spectrum is now a combination

between the blackbody of the earth at temperature of 300K and the spectrum of the water vapor at temperature of 250K instead of the spectrum of the blackbody alone. The carbon dioxide that is located in front of the previous background is scanned with the spectrometer to add more absorption lines to the background spectrum. The carbon dioxide is also at temperature 250K same as the water vapor. Figure A.2 shows the output spectrum.

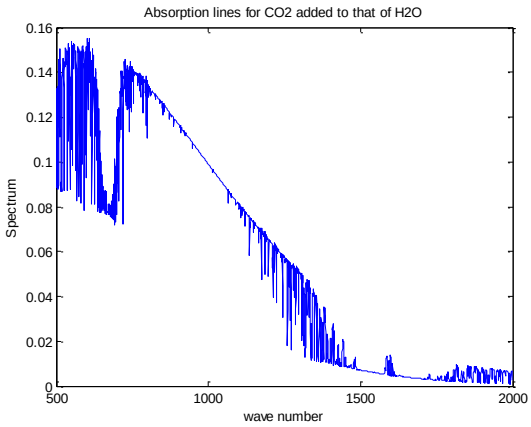

Figure A.2: Simulated CO_2 and H_2O in absorption mode.

A.2 Hitran Database

Hitran (High resolution TRANsmission) database is a component of a larger set of spectroscopic data and software called HAWKS (Hitran Atmospheric Workstation). It can be used to calculate and predict the transmission of radiation in the atmosphere and provide the necessary fundamental parameters to represent molecular properties in atmospheric spectroscopic analysis from the microwave through the ultra-violet spectral regions. The initial database contained only the seven most infrared-active gases: H_20, CO_2, O_3, N_2O, CO, CH, and O_2. Subsequent editions of HITRAN have added many trace atmospheric species [3]. In our simulator, we used HITRAN to generate high resolution spectra for gases. We scan these gases using the spectrometer simulator to obtain the interferograms. Figure A.3 shows the line strength at 296K of CO2, H20, O3, and CH4 obtained with Hitran.

A.3 Multiple Layers Calculations

The concentration, the pressure, the temperature and the path length for the gas are input parameters that will affect the output spectra. In order to be able to change these parameters as well as to compute the absorption or transmission spectrum of multiple layers of atmospheric

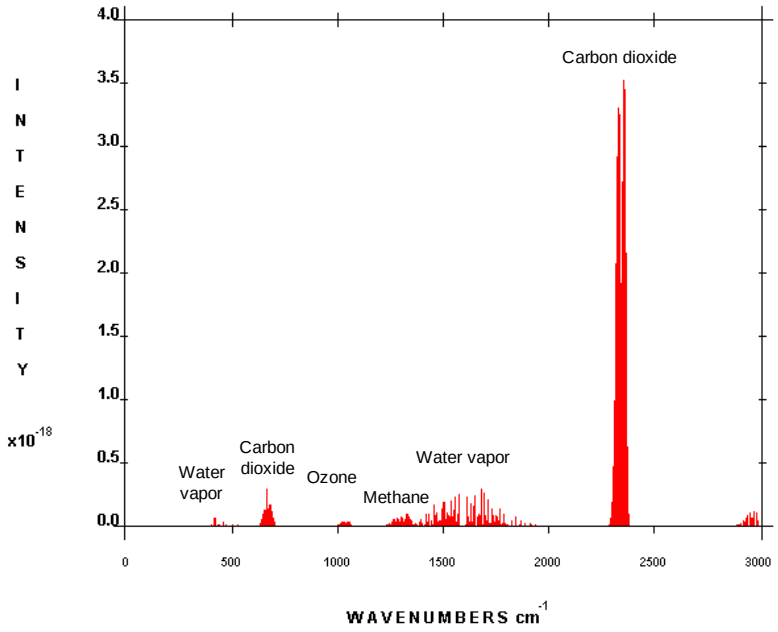

Figure A.3: Line strength at 296K of some gases simulated with Hitran.

gases we use Matlab code (written by R. Desbiens) to perform a line-by-line transmittance calculation based on Voigt profile.

A.4 Downsampling high resolution spectrum

Spectra generated from Hitran are low-passed filtered and downsampled to decrease the running time of the simulator. Lowpass filtering is done with a sinc function whose width has to be half the size of the maximum resolution produced by the simulator. For exemple, suppose we are simulating an IFTS with resolution of $4cm^{-1}$, with a sampling rate twice the maximum wave number which is $8000cm^{-1}$. The needed number of frames to reach this resolution is 4000 frames, as will be discussed later. The resolution of the Hitran spectrum is $0.01cm^{-1}$ and includes 150,000 points describing the spectrum in the range of 5500-7000cm^{-1}. We convolve this spectrum with a sinc function of a width $2cm^{-1}$ that is twice narrower than the output resolution of the simulator. We can the downsample the spectrum by a factor of 200 to 750 points. This significantly contributes to reduce the running time of our simulator.

A.5 Simulator architecture

This section gives a brief overview of the simulator components.

A.5.1 Input parameters

Several parameters can be chosen for the simulator including the number of output frames, size of frame, sensor operating band, off-axis angle, step displacement for the moving mirror, location of the ZPD, camera's output bits, and other parameters can be added for future work like noise and shear.

A.5.2 IFTS processing

When running the simulator each sub-pixel is processed independently. The equation for the spectrometer is applied on the input simulated Hitran spectrum at this sub-pixel location with its corresponding off-axis angle. Each group of sub pixels are integrated to form a pixel. The value of that pixel is the value of the interferogram sample at this OPD. This operation is repeated for each pixel of the frame. For the next frame, the target moves and the computations are performed again to give the next interferogram frame.

The simulator is divided into many functions. The main function is responsible for the determination of the different input parameters and also for calling the other functions. In the main function, the sensor operating range (in wave numbers) is set as well as the number of the output frames. The output resolution of the spectrum is related to the number of frames and the maximum wave number according to the equation

$$\text{number of frames} = \frac{2\sigma_{max}}{resolution} \tag{A.2}$$

where σ_{max} is the maximum wave number.

The moving speed of the target and its initial position as well as the areas of different densities are set also in the main function.

A.5.3 Input spectrum

The main function calls the input spectrum function responsible for simulating the input spectra from Hitran database. The different concentration for the gas are also set, where the maximum concentration is located at the center of the gaz column. The concentration decreases gradually until it is zero. Also, in this function, we generate theoretical black bodies curves using Plank's equation.

The output radiance is then computed based on the scenario we want to simulate (i.e, one, two or multiple gaz layers) at the minimum resolution needed for the parameters of the instrument (i.e. the spectrum is down sampled in this function). For simulation in the NIR band, the earth's reflection coefficient at each sub-pixel location is multiplied with the radiation of the sun after passing through the different gaz layers.

A.5.4 Generating the frames

The sampling rate is set to twice the maximum wave number in the main function. The grid length and width are upsampled to allow sub-pixel motion for the target. The off-axis effect is calculated on a grid according to their spatial location and included in the spectrometer equation.

The simulator starts calculation from the most left frame tot the most right one while passing through the frame of the ZPD at the middle. At each frame the OPD is calculated according to the frame number. The left most frame has an OPD of $-\frac{F}{2S\sigma_{max}}$ and for each subsequent frame, the OPD is increased by $\frac{1}{\sigma_{max}}$, where F is the number of frames and S is the sampling rate. This gives an OPD of zero for one frame (the ZPD frame). The most right frame has an OPD $\frac{F}{2S\sigma_{max}}$.

For each frame, the sub-pixel interferogram values are computed using the interferometer equation. Numerical integration is used to compute the sample value. To shorten the computation time, the off-axis distortion can be calculated only once for each pixel location and its value used for all the sub-pixels at that spatial location. These sub-pixel values are then added to represent the integration of a pixel sensor over an area. The value of each pixel is then quantized to a number of bits to match the resolution of a given IR camera. Once this process is done for all frames, we have a data cube for our simulated IFTS.

A.6 Simulation scenarios

We use the simulator to generate data cubes in both the LWIR and NIR range. We can add a global motion between the IFTS and the scanned target, or add more than a moving target in the scene of the IFTS. In this section we discuss two data cubes generated from the simulator and used in the thesis.

A.6.1 Moving IFTS in the LWIR band

We chose to design an elliptical target. The concentration of gas is maximum at the center and decreases gradually until it is zero. We can change the size, the shape, and the area occupied by each concentration. The initial position and motion direction can be changed. As an example, we can assume that we have two targets, respectively of CO_2 and H_2O at a temperature lower than the temperature of the background. The targets are at 250K while the background is a blackbody at 300K, so the targets are in absorption mode.

The input spectrum for the simulator is then the blackbody as seen through the gaz targets, so the targets appear to be darker than the background. The water vapour target will appear darker than the carbon dioxide target since it absorbs more. We can then propose a motion for both targets. Figure A.4 shows sample frames for a scenario.

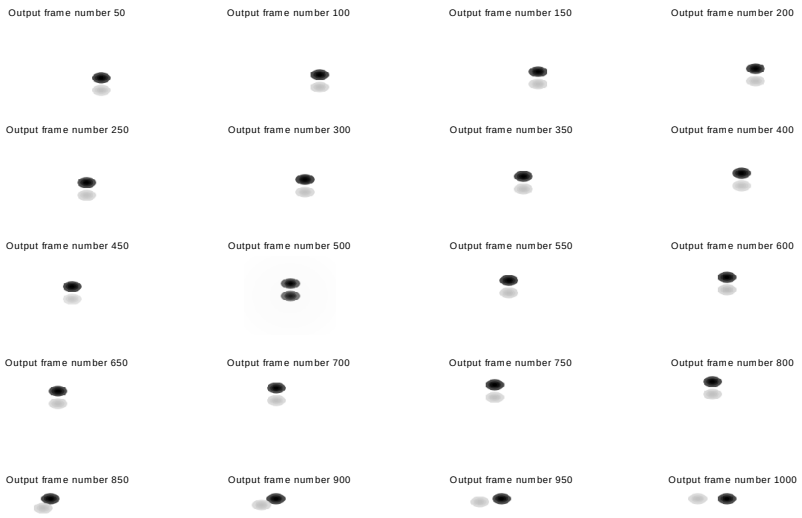

Figure A.4: Output frames from the simulator in the LWIR.

A.6.2 Moving IFTS in the NIR

In this scenario, the IFTS is assumed to be placed on a plane scanning a column of gas at a height nearly 2 km above the earth's surface. The column of CO_2 gas (for exemple) has an elliptical shape with a maximum concentration of 380 ppm at the center and decreasing gradually to the edges. The sensor operating band of the IFTS is between 5500-7000 cm^{-1}. The reflectance of earth's surface is simulated using a NASA database in that same band, and is normalized to 0.4 as a maximum reflection coefficient. Since the data in the NASA database contains only 224 samples for the 4000-25000 cm^{-1} range, we interpole the values to the spectral resolution we simulate. The transmittance of CO_2 is obtained from Hitran spectroscopic database. Figure A.5 shows the setup for this scenario.

For each pixel in the scene, the radiation received by the IFTS is that transmitted through the column of the gas, multiplied with the reflection coefficient for the corresponding ground's surface, and then multiplied again with the transmission parameters of the CO_2. Figure A.6 shows a pixel reflection pattern obtained from the NASA database, the transmission pattern for the CO_2 with the highest concentration in the column, and the radiation received by the IFTS. The last image is the shape of the column of the gas.

Sample frames of cube generated with this simulator are given in Figure A.7. In this case,

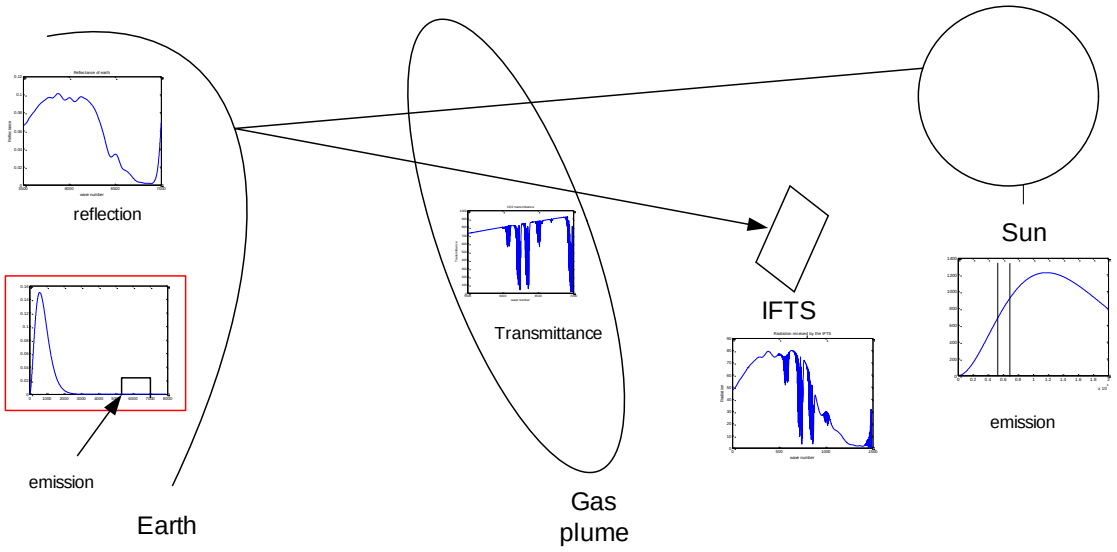

Figure A.5: Scenario for an IFTS in the NIR band.

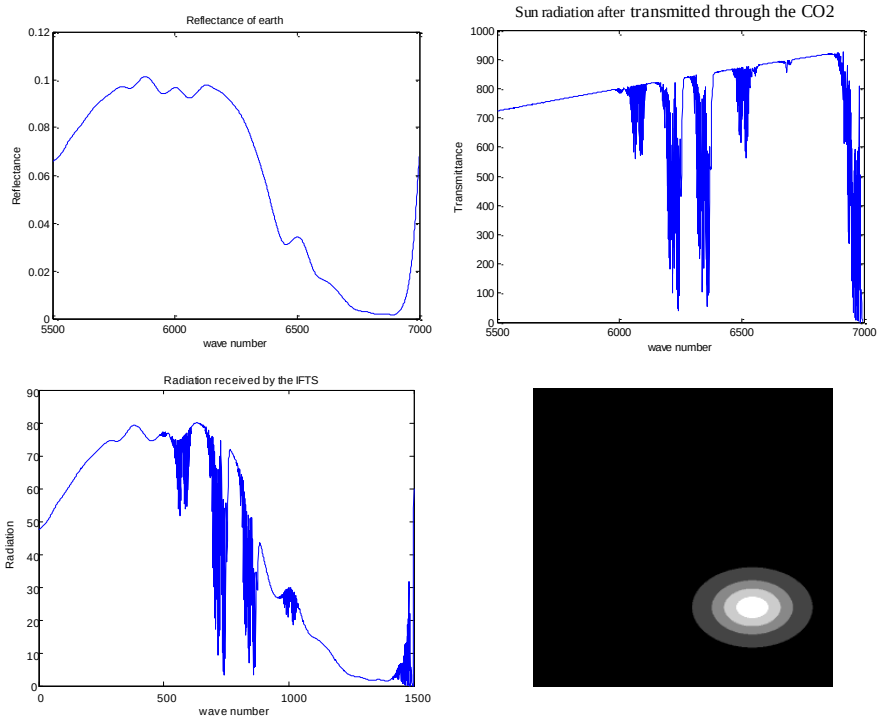

Figure A.6: Reflection of earth's surface (upper left), radiance of sun after transmitted through CO_2 column (upper right), signal received by IFTS (down left), and the column of the CO_2 (down right).

we simulated a fixed CO_2 column of gas with a diagonally moving IFTS. The simulated hyper-spectral cube has 4000 frames of 64 x64 pixels, with a $3.5cm^{-1}$ spectral resolution. The sampling rate or the minimum OPD step is set to twice the maximum wave-number ($7000cm^{-1}$). Each pixel of the simulator is obtained by integration over the sensor area, simulated here by dividing each pixel in 10×10 sub-pixels. The integration is actually done on a matrix of 9×9 sub-pixels, where the remaining sub-pixels are left empty to simulate the area needed by the sensor's electronics (which gives a fill ratio of 81%. Due to the spatially varying reflection coefficient, the target is blurred in the output frames.

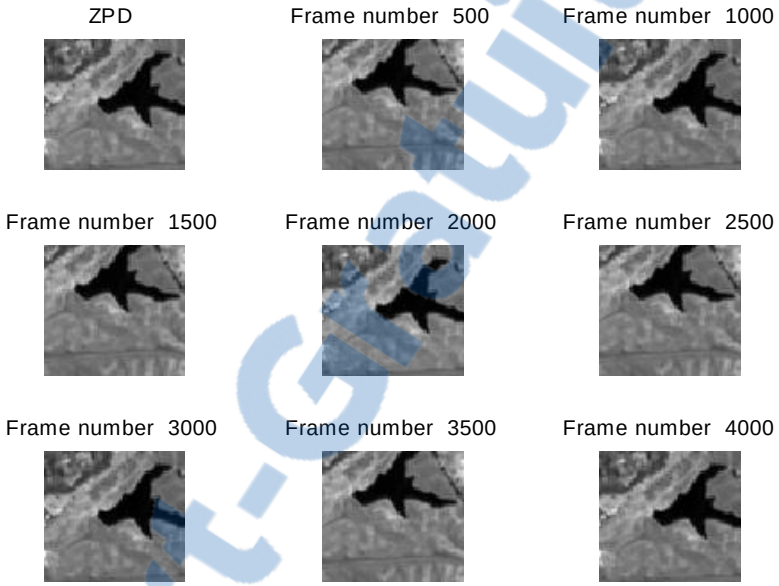

Figure A.7: Output frames from the simulator in the NIR.

Appendix B

GDIM algorithm modification

In this appendix, we describe small modifications made to the GDIM algorithm to improve the motion estimation on interferogram frames.

For the brightness variation between the frames of the IFTS cube, we observe that it depends mainly on the multiplier factor. The multiplier factor resulted from the matrix is always robust even around the ZPD where the brightness varies non-uniformly to high extends and the geometric parameters are noisy. We modify the GDIM algorithm to benefit from the robustness of the multiplier factor to increase the accuracy of the geometric parameters.

B.1 Division using the radiometric multiplication factor

We observed that the radiometric multiplier factor, $\delta m(r)$ was the dominant parameter to explain the brightness change between the pixel of two interferogram frames. This parameter was also robustly estimated for frames around the ZPD where the brightness variation is significant, but where the estimated motion vectors are poorly estimated. We proposed to iteratively used the GDIM algorithm but on frames where the radiometric multiplication factor estimated at each iteration is used to modify the data.

More specifically, assume that we have 2 frames, frame k and frame $k+1$ frame, and r is the vector denoting the spatial coordinates of a pixel. We first use the GDIM algorithm between frames k and $k+1$ to obtain the geometric and the radiometric parameters. We then divide frame $k+1$ by the estimated parametric multiplier factor, $\delta m(r)$. Assuming that the motion vectors between two successive frames are relatively small, we first align the frame of the multiplication factors using the motion vectors before the division. We then reuse the GDIM algorithm on frame k and the new version of frame $k+1$ to estimate the motion vectors and the radiometric parameters. This is repeated iteratively until the parameter values are stable, which in our tests, happens after a small number of iterations.

Figure B.1 shows that the motion vector estimated with this iterative approach converges after

3 or 4 iterations. By removing the contribution of the radiometric multiplication factor, we can better estimates of the motion vectors.

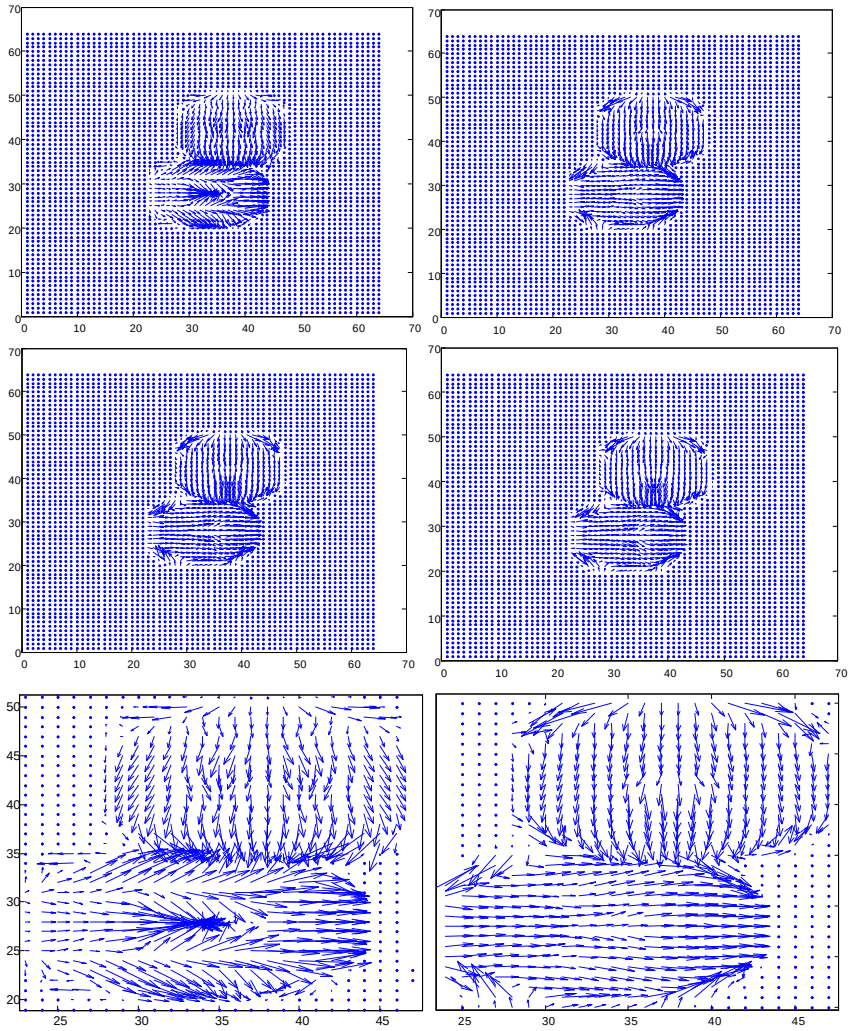

Figure B.1: Motion vectors evaluation through 4 iterations. Iteration 1 (upper left corner), iteration 2 (upper right corner), iteration 3 (lower left corner), and iteration 4 (lower right corner). Last row is a zoom on the motion vectors after iteration 1 (left) and 4 (right).

Figure B.2 shows the values of the parametric multiplication factor for 4 iterations. We can clearly that the differential motion factor converges to a value of one.

B.2 Partial derivative calculation

We need to estimate the derivatives of brightness between reference frame k and test frame $k+1$. Let the measured brightness be $e_{i-1,j,k}$ at spatial coordinate i and j in the k^{th} frame. We propose to replace the the pixel brightness with an average brightness of its neighborhood to

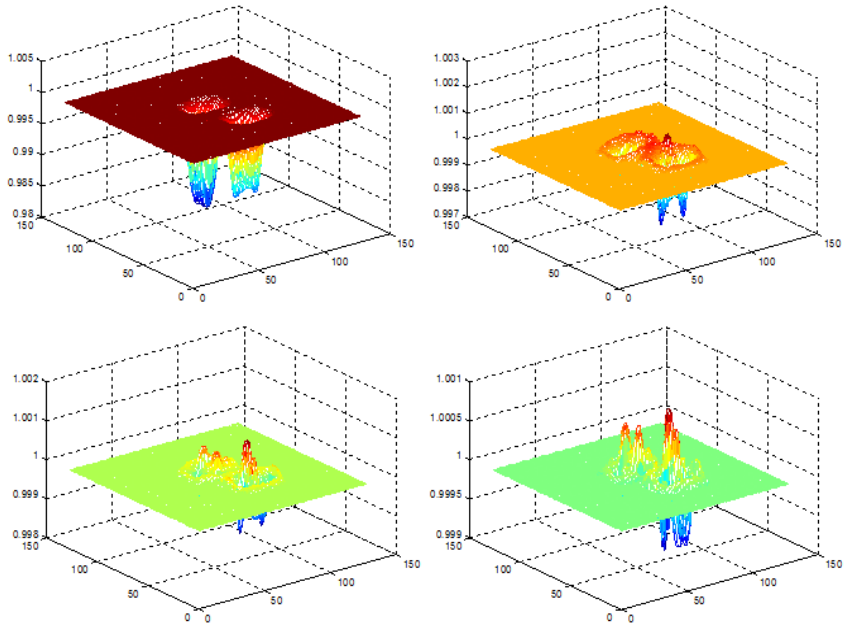

Figure B.2: The evolution of the multiplier factor through the iteration of the GDIM. Each iteration the multiplier factor is divided from the test frame. Iteration 1 (upper left corner), iteration 2 (upper right corner), iteration 3 (lower left corner), and iteration 4 (lower right corner).

further decrease the noise and improve the estimation of the motion vectors. The derivatives in the x-direction, y-direction are calculated as follow

$$e_x = e_{i+1,j,k} - e_{i-1,j,k}$$
$$e_y = e_{i,j+1,k} - e_{i,j-1,k}$$

while the pixel brightness is replaced by

$$e = \frac{1}{10}(e_{i,j,k+1}+e_{i,j,k}+e_{i-1,j,k+1}+e_{i-1,j,k}+e_{i+1,j,k+1}+e_{i+1,j,k}+e_{i,j-1,k+1}+e_{i,j-1,k}+e_{i,j+1,k+1}+e_{i,j+1,k})$$

We compute the time derivative twice to balance the filter. While estimating the motion vectors in the x-direction, we use the pixels in this direction only to compute the time derivative. While computing the motion vectors in the y-direction, only the pixels in the y-direction are used for the time derivative. Each of the estimates is the average of the three differences between the pixels in the k frame and the $k+1$ frame as follow

$$e_{tx} = (e_{i+1,j,k} - e_{i+1,j,k+1} + e_{i,j,k} - e_{i,j,k+1} + e_{i-1,j,k} - e_{i-1,j,k+1})$$
$$e_{ty} = (e_{1,j+1,k} - e_{i,j+1,k+1} + e_{i,j,k} - e_{i,j,k+1} + e_{i,j-1,k} - e_{i,j-1,k+1})$$

where e_{tx} and e_{ty} are the time derivatives in the x and y directions. We need to solve the GDIM matrix twice, one for the motion vectors in the vertical direction, and one for the

motion vectors for the y-direction. Although this doubles the processing time, the results are not biased to a certain direction. The radiometric multiplier and offset factor are obtained by averaging the results from both GDIM runs. Figure B.3 shows the pixels that are used for computing the derivatives.

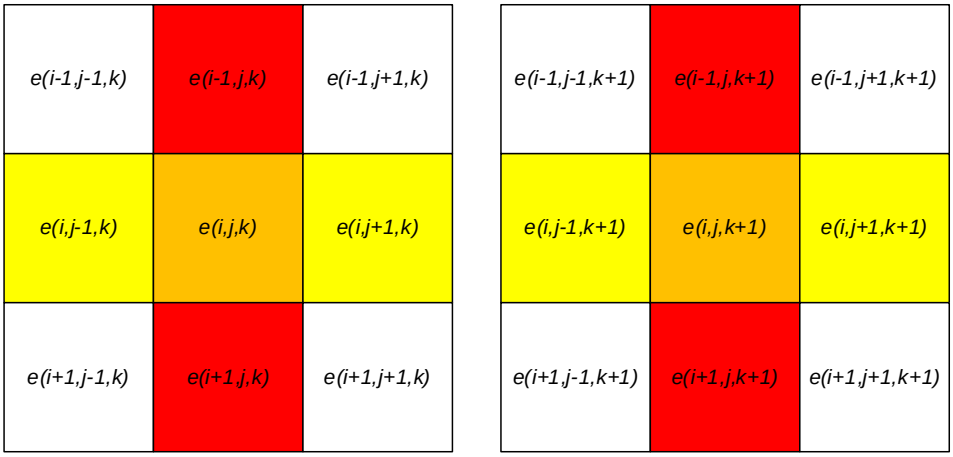

Figure B.3: The k and k+1 frames, where the red color indicates the vertical direction (x), and the yellow color indicates the horizontal direction (y). The 10 colored pixels are used to compute the average brightness value.